

AD-A214 908

DTIC FILE COPY

1



DTIC
ELECTE
DEC 04 1989
S B D

THEORETICAL AND EXPERIMENTAL
INVESTIGATION OF COUPLED
AR-ION LASERS

DISSERTATION

Mark P. Jelonek

Captain, USAF

AFIT/DS/ENP/89-3

DEPARTMENT OF THE AIR FORCE
AIR UNIVERSITY
AIR FORCE INSTITUTE OF TECHNOLOGY

Wright-Patterson Air Force Base, Ohio

DISTRIBUTION STATEMENT A

Approved for public release
Distribution Unlimited

89 12 01 040

AFIT/DS/ENP/89-3

①

THEORETICAL AND EXPERIMENTAL
INVESTIGATION OF COUPLED
AR-ION LASERS

DISSERTATION

Mark P. Jelonek

Captain, USAF

AFIT/DS/ENP/89-3

Approved for public release; distribution unlimited

S DTIC
ELECTE
DEC 04 1989 **D**
B

AFIT/DS/ENP/89-3

THEORETICAL AND EXPERIMENTAL INVESTIGATION
OF COUPLED AR-ION LASERS

DISSERTATION

Presented to the Faculty of the School of Engineering
of the Air Force Institute of Technology

Air University

In Partial Fulfillment of the
Requirements for the Degree of
Doctor of Philosophy

Mark P. Jelonek, B.S., M.S.

Captain, USAF


October, 1989

Approved for public release; distribution unlimited


THEORETICAL AND EXPERIMENTAL INVESTIGATION
OF COUPLED AR-ION LASERS

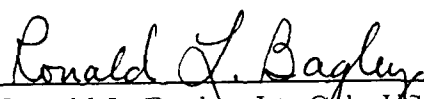
Mark P. Jelonek, B.S., M.S.
Captain, USAF

Approved:

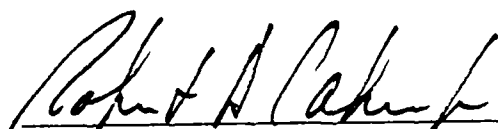
 23 Oct 89
Won B. Roh, Chairman

 23 Oct 89
Theodore E. Luke

 23 Oct 89
Steven K. Rogers, Maj., USAF

 23 Oct 89
Ronald L. Bagley, Lt. Col., USAF

Accepted:

 23 Oct 89
Robert A. Calico, Jr.
Interim Dean, School of Engineering

Acknowledgements

Even though many hours of intensive study, hard work, and careful preparation are important, more than four years of graduate research has convinced me that the single most critical factor in the successful completion of a doctoral dissertation is luck. I was fortunate to receive more than my fair share. At times, I thought I would never produce anything of value and suffer my first real academic defeat, but the dice tumbled to the right numbers at the right time.

I owe a deep debt of thanks to many people, but I could not even pay the interest on the time, guidance, and education my advisor, Dr. Won B. Roh, has invested in me. Anyone can teach facts, but more than all else, Dr. Roh taught me to be a responsible member of the physics community. I'd like to thank Lt. Col. James Lupo for cheerfully fielding my seemingly incessant questions on computer operations. I also wish to thank Mr. William Evans and the rest of the laboratory support staff who continually battled the supply system bureaucracy to procure equipment for me. Much of this work could not have been completed without the generous support of other Air Force organizations including the Air Force Office of Scientific Research and Maj. Tony Corvo and Dr. Tom Gavrielides of the Air Force Weapons Laboratory. A special thanks must go to Capt. Steve Rinaldi for sharing his extensive knowledge of laser processes during our frequent discussions. Finally, I'd like to thank my fellow doctoral students whose encouragement and suggestions allowed me to plow through many substantial roadblocks. To all, thank you.

- Mark P. Jelonek



n For	
AI	
<input checked="checked" type="checkbox"/>	
<input type="checkbox"/>	
ed	
tion	
By	
Distribution/	
Availability Codes	
Dist	Avail and/or Special
A-1	

Table of Contents

Acknowledgements	ii
List of Figures	v
List of Tables	ix
Abstract	x
Chapter I. Introduction	1
A. Overview	1
B. Laser Coupling	2
C. Advantages to Phase Locking	5
D. History of Laser Coupling	10
E. Dissertation Outline	12
Chapter II. Coupled Laser Theory	13
A. History of Laser Coupling Theory	13
B. Single-Mode Theory	15
C. Two-Mode Theory	33
D. Conclusion	45
Chapter III. Coupled Ar-ion Lasers Experiment	46
A. Experimental Configurations	46
B. Measurements	54
Chapter IV. Results and Analysis	57
A. Data	57
i. General Descriptions	57
ii. Interference Fringes	59
B. Analysis	61
Chapter V. Conclusions and Recommendations	80
A. Summary	80
B. Recommendations	83
C. <i>Finis</i>	84
Appendix A: Computer Simulations	85
A. Single-Mode Equations	85
i. Mathematics	85
ii. Stability	88
iii. Computer Program for Single-Mode Coupled Laser Equations	90

B. Two-Mode Equations	97
i. Mathematics	97
ii. Stability	99
iii. Computer Program for Two-Mode Coupled Laser Equations	100
Appendix B: Experimental Verification of the Mutually-Reinforced Hole-Burning Minimum	115
A. Spectral Hole Burning Theory	115
B. Experimental Verification	120
Appendix C: Passive Mode Analysis of Three Mirror Fabry-Perot Resonators	124
A. Field Equations for Three-Mirror Interferometers	124
B. Application to Filters	127
C. Application to Coupled Laser Resonators	129
D. Conclusion	135
Bibliography	138
Vita	141

List of Figures

Figure		Page
1.1	(a) Coupled masses and springs; Coupled Helmholtz resonators; (c) Coupled tank circuits; (d) Coupled Lasers.	4
1.2	Configuration for a Young's two-slit interference experiment.	6
1.3	Configuration for far-field interference of two plane waves.	8
2.1	Geometry for coupled laser theory.	16
2.2	Reflected and transmitted waves at the coupling mirror interface.	23
2.3	Geometry to derive net perturbation per round trip coupling terms.	24
2.4	Schematic diagram of the coupled laser system for (a) a single mode oscillating in each cavity and (b) two modes oscillating in each cavity.	25
2.5	Intensity, frequency detuning, and phase as a function of cavity detuning for single-mode coupling for the case of translating both output mirrors. The solutions are stable for all displacements.	28
2.6	Intensity, frequency detuning, and phase as a function of cavity detuning for single-mode coupling for the case of translating a single output mirror. The solutions are stable from -3.48 MHz to +3.14 MHz.	29
2.7	Intensity, frequency detuning, and phase as a function of cavity detuning for single-mode coupling for the case of translating the coupling mirror. The solutions are stable from -1.65 MHz to +1.65 MHz.	30
2.8	Locking range as a function of coupling mirror transmission for both single- and two-mode coupling during translation of a single output mirror.	34

2.9	Intensity, frequency detuning, and phase as a function of cavity detuning for two-mode coupling for the case of translating both output mirrors simultaneously. (a)-(c) $\psi = -\pi/2$, (d) $\psi = +\pi/2$. The solutions are stable for all displacements.	39
2.10	Mode structure of intensity versus cavity detuning for a single, uncoupled laser. See text for complete explanation.	41
2.11	Intensity, frequency detuning, and phase as a function of cavity detuning for two-mode coupling for the case of translating a single output mirror. The solutions are stable for -6.41 MHz to +6.43 MHz.	43
2.12	Intensity, frequency detuning, and phase as a function of cavity detuning for two-mode coupling for the case of translating the coupling mirror. The solutions are stable for -2.94 MHz to +3.26 MHz.	44
3.1	Schematic diagram for multiline coupling without an optical trombone for path length compensation.	48
3.2	Schematic diagram for multiline coupling with an optical trombone for path length compensation and the diagnostic equipment used for the measurements.	49
3.3	Schematic diagram for single wavelength coupling with an optical trombone for path length compensation.	50
3.4	Multiline fringe envelope generated from the near-field interference of the four Ar-ion laser wavelengths described in the text as the optical trombone is scanned.	53
4.1	Multimode frequency spectrum showing (a) the equal intensity grass with no coupling mirror, and (b) the mode spiking with a 70% reflective coupling mirror.	60
4.2	Sample near-field interference fringes from multiline coupling without the optical trombone. R_c = Coupling Mirror Reflectivity, V = Visibility.	62
4.3	Sample near-field interference fringes from multiline coupling with the optical trombone. R_c = Coupling Mirror Reflectivity, V = Visibility.	63

4.4	Sample near-field interference fringes from single-line coupling at 488.0 nm. R_c = Coupling Mirror Reflectivity, V = Visibility.	64
4.5	Fringe visibilities plotted as a function of coupling mirror transmission for two coupled multiline lasers with the optical trombone in the coupling path.	65
4.6	Fringe visibilities plotted as a function of coupling mirror transmission for two coupled single-line lasers oscillating at 488.0 nm with the optical trombone in the coupling path.	66
4.7	Fringe visibilities plotted as a function of coupling mirror transmission for two coupled multiline lasers without the optical trombone in the coupling path.	67
4.8	Radio frequency mode beat spectrum of the multiline coupled lasers with a 70% reflective coupling mirror.	69
4.9	Fields, phases, mirror reflectivities and transmissivities, and round trip gains for a three-mirror cavity.	73
B.1	Spectral hole burning of a Doppler-broadened gain curve: (a) A laser mode oscillating at a frequency away from the gain center burns two holes in the gain curve. (b) A mode oscillating at the gain center burns one hole. (c) The laser output intensity exhibits a Lamb dip as the laser is tuned across the gain curve.	117
B.2	Intensity tuning curve of a two-mode laser. The intensity shown represents the incoherent sum of the individual mode intensities. The spectral locations of the modes at various points along the tuning curve are shown as (a)-(d).	118
B.3	Schematic diagram of the experimental setup. PZT is a piezoelectric transducer.	121
B.4	Recorder trace of the photodetector output exhibiting the mutually-reinforced hole-burning minimum as the PZT-mounted cavity mirror is translated by a ramp signal. See text for explanation.	122
C.1	Fields, phases, mirror reflectivities and transmissivities, and round trip gains for a three mirror cavity.	126

C.2	Normalized reflected and transmitted intensities for a three-mirror cavity plotted as a function of frequency with the two end mirrors of 90% reflectivity and the center mirror of 50% reflectivity.	130
C.3	Round trip gain plotted as a function of frequency showing the spacing of the resonant modes and magnitudes with the gain medium in the left- or right-hand cavity only.	132
C.4	Phase angle $\theta/2\pi$ plotted as a function of frequency showing the three oscillating frequencies corresponding to (a) $L_1 + L_2$, (b) $2L_1$, (c) $2L_2$, and (d) when all three frequencies are equal.	136

List of Tables

Table		Page
2.1	Symbols and Definitions	21.22
2.2	Ar-ion Laser Parameters	26
3.1	Ar-ion Wavelengths and Intensities	52
4.1	Output Power for each Coupling Mirror	61
4.2	Fringe Visibilities and Standard Deviations for Coupling without the Optical Trombone (R_c : Coupling Mirror Reflectivity, N: Number of Samples, V: Visibility, σ : Standard Deviation)	75
4.3	Fringe Visibilities and Standard Deviations for Coupling with the Optical Trombone (R_c : Coupling Mirror Reflectivity, N: Number of Samples, V: Visibility, σ : Standard Deviation)	76
4.4	Fringe Visibilities and Standard Deviations for Single-Line Coupling (488.0 nm) with the Optical Trombone (R_c : Coupling Mirror Reflectivity, N: Number of Samples, V: Visibility, σ : Standard Deviation)	77
4.5	Actual Coupling Mirror Reflectivities Measured with a Spectrophotometer Compared to the Manufacturers Specifications for the Experimental Wavelengths	78
4.6	Wave Intensities for Passive Cavity Mode Analysis of Two Coupled Fabry-Perot Resonators (R_2 : Coupling Mirror Reflectivity; See Figure 4.9 for Symbols; $C=1.00$)	79
A.1	Single-Mode Perturbation Matrix Coefficients	89
A.2	Definitions of Computer Symbols	91
B.1	He-Ne Laser Parameters	119

Abstract

A single-mode laser theory was applied to two coupled Ar-ion lasers in Fabry-Perot resonators and the equations were solved numerically to predict intensity tuning curves and locking ranges for various types of mirror translations. The same theory was extended to model two modes in each cavity, which predicted a decrease in locking range as well as a mutually-reinforced hole-burning minimum. With a single, uncoupled, two-mode He-Ne laser, the existence of the minimum was verified experimentally. Two multiline/multimode Ar-ion lasers were coupled through a common end mirror and the effect of coupling strength on phase locking was investigated by varying the reflectivity of that mirror. In order to characterize the phase-locked performance of multiline/multimode and single-line/ multimode coupling, interference fringe visibilities, output power, and frequency and RF mode beat spectra were measured. It was found that the optimal phase locking occurred at approximately 25% coupling as determined by the maximum fringe visibilities produced by laser phase locking. That 25% coupling was the optimum coupling strength was also substantiated by the fact that the maximum power output was also achieved at this point, and the appearance of the super cavity mode spacing verified that the behavior was due to phase locking. A passive cavity mode analysis of the three-mirror Fabry-Perot resonator showed that the system oscillated on the composite resonator frequency as well as the frequencies of both subresonators.

A Theoretical and Experimental Investigation of Coupled Ar-ion Lasers

Chapter I. Introduction

This dissertation research theoretically and experimentally investigated the phase-locked performance of two coupled Ar-ion lasers in Fabry-Perot resonators along with several other associated aspects of coupling. The following is a brief overview of why the U.S. Air Force and the military in general is interested in coupled laser systems. In the remainder of the introduction, the concepts of laser coupling will be presented followed by a discussion of the advantages of phase-locked operation. The next section will review some of the previous experiments studying phase locking using conventional coupling, and the final part will be a synopsis of the dissertation contents.

A. Overview

The United States Air Force is currently investigating the feasibility of using high-energy lasers as one component of the ballistic missile defense network proposed as part of the Strategic Defense Initiative (SDI). High-energy lasers could also be used in a lower power and somewhat more peaceful role as a means of communicating with undersea vehicles or as the drivers for laser fusion power plants. For the ballistic missile defense applications, a simple diffractive optics calculation using intercontinental distances indicates that a tremendous amount of energy is needed to achieve the required power density on target to assure a kill.

Whether for civilian or military application, laser output energy must increase by several orders of magnitude before any system can be deployed. Although it is theoretically possible to increase laser output by proportionately scaling the size of the laser and the amount of gain medium, current technology restrictions put severe limitations on the size and power of lasers that can be constructed.

One possible method for scaling laser power to higher output levels and thus circumventing some of the technology shortfalls is to coherently combine or phase lock an array of small, low power, independent lasers using conventional coupling. Conventional coupling means injecting a portion of the output of each laser into the other resonators via partially transmitting mirrors, holes in the optics, or diffraction around the mirrors. In spite of some added complexities, coherent combination of lasers offers advantages over incoherent combination because the resultant smaller far-field spot size produced by phase locking increases the power density on target by the square of the number of lasers. Also, because the system is comprised of independent lasers, the array can still function, although below peak capacity, with one or more of the lasers inoperative.

B. Laser Coupling

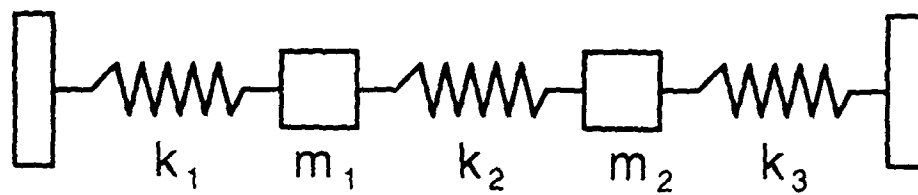
The study of coupled oscillators is by no means a new field of endeavor, but the study of coupled lasers is still in its infancy mostly because lasers have only been around as a useful tool since the early 1960's. Despite a thorough understanding of many types of coupled oscillators, coupled lasers have escaped complete characterization not only because they operate on the order of 10^{15} Hz, but

also because the oscillating fields originate within the medium itself. This self-generating oscillation presents a unique set of problems from which the low-frequency coupled oscillators do not suffer. Coupled oscillators can be roughly divided into four different frequency subgroups ranging from subhertz all the way to 10^{15} Hz. The first category is the mechanical oscillators; springs-and-masses and pendulums which oscillate up to several hertz. Next are the coupled acoustic resonators which function from several hertz up to tens of kilohertz before air mass movement in the coupled Helmholtz resonators begins to pose an upper limit. In tank and radio circuits, the light, nimble electrons can respond to electric fields all the way up into the gigahertz régime. Presently, the upper limit of coupled oscillators is lasers whose electric fields oscillate at a frantic 10^{15} Hz (See Figure 1.1).

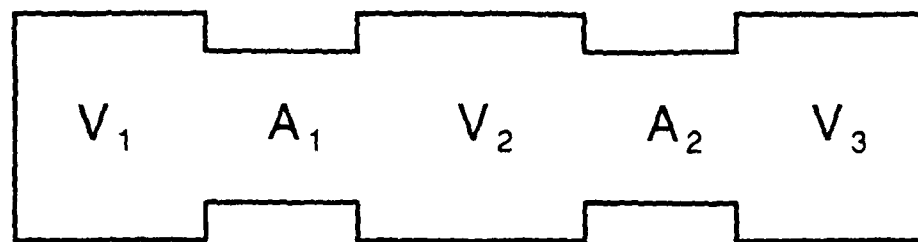
What is truly remarkable is that the four vastly different types of coupled oscillators are governed by equations similar in form. Each is based on the fundamental expression which comprises the time variation of the equation of motion

$$m\ddot{x} + b\dot{x} + kx \tag{1.1}$$

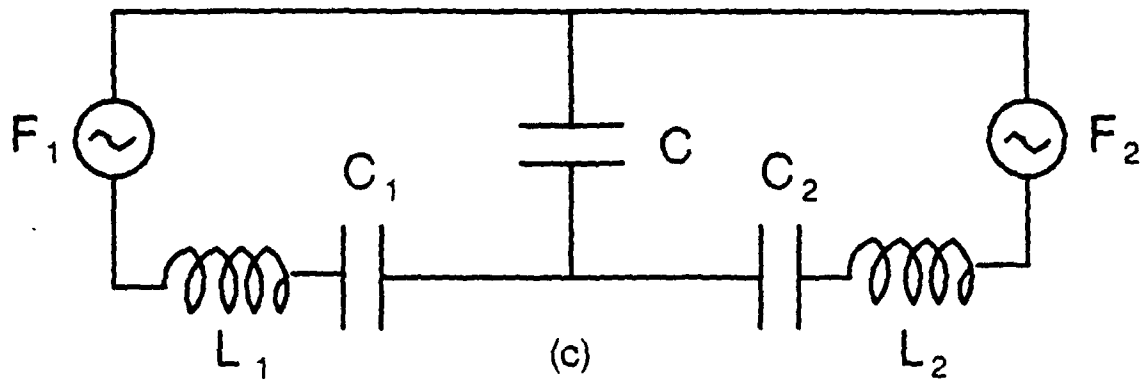
plus a coupling and driving term. Superficially, the analogy appears to be encouraging, but examination of the characteristic frequency of each oscillatory system uncovers a marked difference between the coupled lasers and the others. The mass attached to the spring, the acoustical inertance of the air mass in the Helmholtz resonator, and the opposing magnetic field encountered by an electron in an inductor all constitute the mass term in the equation of motion, but the



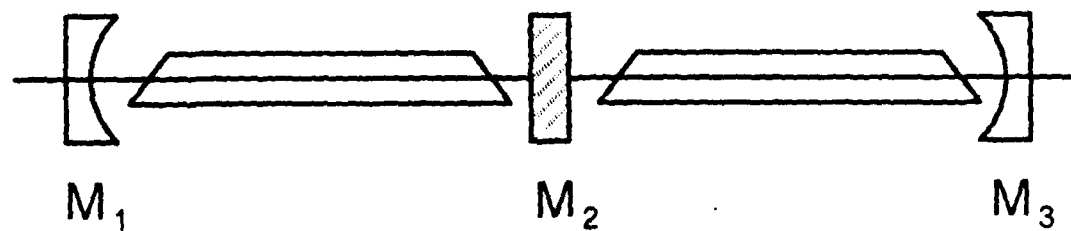
(a)



(b)



(c)



(d)

Figure 1.1: (a) Coupled masses and springs; (b) Coupled Helmholtz resonators; (c) Coupled tank circuits; (d) Coupled Lasers.

photon "mass" is hidden and undiscernable in the laser frequency term:

$$\begin{array}{lll}
 \text{Mechanical}^1 & \omega_0 = \left(\frac{k}{m} \right)^{\frac{1}{2}} & \begin{array}{l} k = \text{spring constant} \\ m = \text{mass} \end{array} \\
 \text{Acoustical}^2 & \omega_0 = \left(\frac{A v^2}{V l} \right)^{\frac{1}{2}} & \begin{array}{l} A = \text{area} \\ V = \text{volume} \\ l = \text{neck length} \\ v = \text{velocity} \end{array} \\
 \text{Electrical}^3 & \omega_0 = \left(\frac{1}{L C} \right)^{\frac{1}{2}} & \begin{array}{l} L = \text{inductance} \\ C = \text{capacitance} \end{array} \\
 \text{Optical}^4 & \omega_0 = n \frac{\pi c}{L} & \begin{array}{l} n = \text{integer} \\ L = \text{resonator length} \\ c = \text{velocity of light} \end{array}
 \end{array} \tag{1.2}$$

Similarly, the damping caused by friction, viscosity, or resistance is more easily traced than the nebulous losses associated with diffraction and absorption in the laser cavity. The most striking disparity between the first three systems and the coupled lasers lies in the driving term. Simple sinusoidal and constant phase driving forces lead nicely to analytical solutions, but the complexities and approximations inherent in the derivation of the driving quantum mechanical polarization separates an optical maverick from a stable of better behaved oscillators.

C. Advantages of Phase Locking

There are significant advantages to a phase-locked laser system over the same number of uncoupled lasers focussed to the same target point. The intensity

distribution on target from independent lasers is the diffraction limited sum of the intensities of the individual lasers, $N \times I$, but the peak intensity from the same number of phase-locked lasers is proportional to the square of the number of lasers, $N^2 \times I$. The N^2 effect arises from coherence and can be understood in terms of the theory of a Young's two-slit interference experiment as presented by Goodman ⁵ and of interference theory.

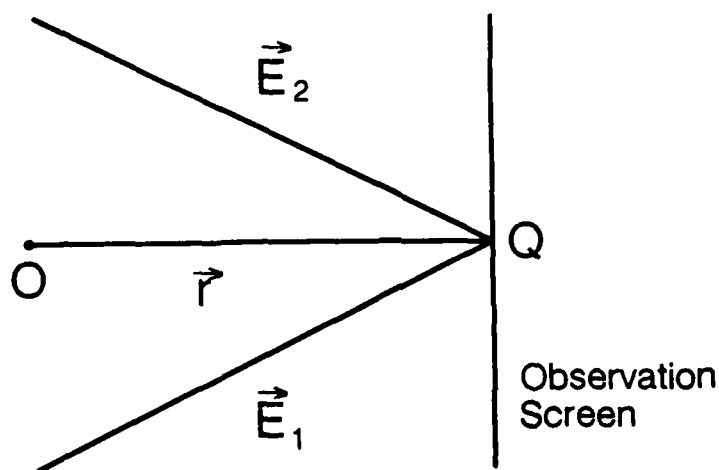


Figure 1.2: Configuration for a Young's two-slit interference experiment.

Consider the interference experiment depicted in Figure 1.2. The intensity at some point Q on the screen is given by

$$I(Q) = \langle |\vec{E}_1 + \vec{E}_2|^2 \rangle \quad (1.3)$$

where $\langle \rangle$ denotes a time average and

$$\vec{E}_i = E_{0i} \hat{e}_i \exp[i(\vec{k}_i \cdot \vec{r} - \omega_i t + \phi_i(t))] \quad (1.4)$$

E_{0i} is the field amplitude of the waves

\hat{e}_i is the unit polarization vector

\vec{k}_i is the propagation vector

\vec{r} is the position vector of a point on the screen

ω_i is the frequency

$\phi_i(t)$ is the initial phase of the wavefront.

If the polarizations are identical, then substituting (1.4) into (1.3) yields

$$I(Q) = |E_{01}|^2 + |E_{02}|^2 + 2E_{01}E_{02}^* \cos[(\vec{k}_1 - \vec{k}_2) \cdot \vec{r} - (\omega_1 - \omega_2)t + (\phi_1(t) - \phi_2(t))] \quad (1.5)$$

If $|E_{01}|^2 = |E_{02}|^2 = I$, then

$$I(Q) = 2I(1 + \cos\theta) \quad (1.6)$$

where $\theta = (\vec{k}_1 - \vec{k}_2) \cdot \vec{r} - (\omega_1 - \omega_2)t + (\phi_1 - \phi_2)$. The locking phenomena may be understood through closer examination of θ . If $\omega_1 = \omega_2$, the two waves are said to be frequency locked, but the phases may continue to change as random functions of time and spoil the N^2 peak intensity. If on the other hand, a fixed relationship occurs between ϕ_1 and ϕ_2 , the laser phases are locked, but any difference between ω_1 and ω_2 will cause a beat signal which creates a time-dependent interference pattern whose amplitude varies with the amplitude of the beat envelope. When $\omega_1 = \omega_2$, and there is a fixed phase relationship, the two waves are phase locked and produce a steady intensity distribution in the near field as described by equation (1.5). At all points for which $\cos\theta = 1$, the intensity is $4 \times I$ or $2^2 \times I$.

The coherent summation concentrates the energy into a smaller area giving rise to the N^2 effect. To better understand the mathematics of the far-field nar-

rowing which causes this N^2 effect, consider the following example of the coherent summation of two plane waves. When two plane waves are combined in the far field (See Figure 1.3), the field distribution at the observation screen is

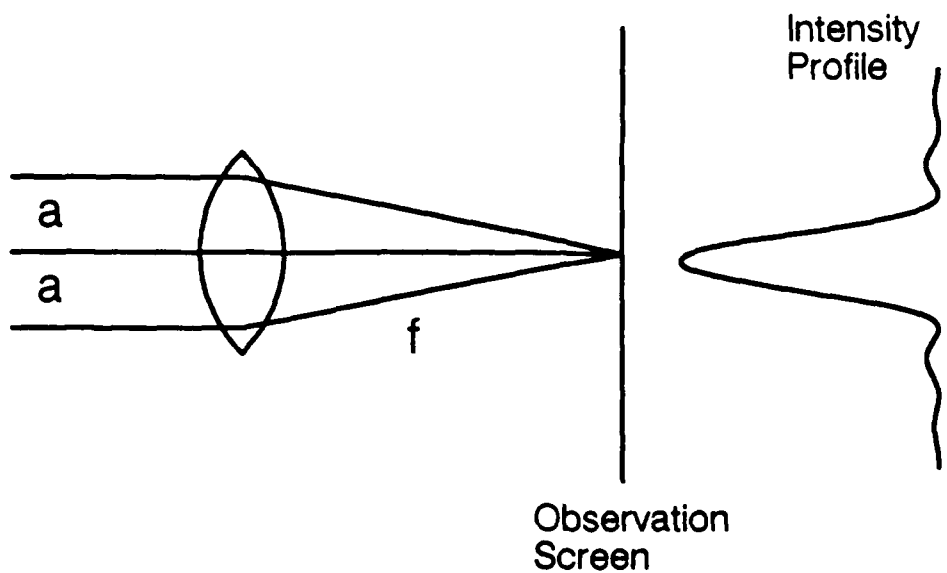


Figure 1.3: Configuration for far-field interference of two plane waves.

$$\begin{aligned}
 E(u) &= -\frac{i}{\lambda} E_0 \frac{e^{ikf}}{f} \int t(x) e^{i2\pi qx} dx \\
 &= -\frac{i}{\lambda} E_0 \frac{e^{ikf}}{f} \left[\int_{-\frac{a}{2}}^{\frac{a}{2}} e^{i2\pi qx} dx + \int_{\frac{3a}{2}}^{\frac{5a}{2}} e^{i2\pi qx} dx \right] \quad (1.7) \\
 &= -\frac{i}{\lambda} E_0 \frac{e^{ikf}}{f} \left(\frac{1}{\pi q} \right) e^{i\pi qa} \sin 2\pi qa
 \end{aligned}$$

where $t(x)$ is the transmission function of the lens, f is the focal length, a is the diameter of the beams, and q is the spatial frequency associated with some point

on the screen. Taking the magnitude gives the intensity:

$$I(q) = \left(\frac{E_0}{\lambda f} \right)^2 4a^2 \frac{\sin^2 2\pi qa}{(2\pi qa)^2} \quad (1.8)$$

where $I(q) = 0$ when $q = 1/(2a)$. For a single beam of diameter a ,

$$I(q) = \left(\frac{E_0}{\lambda f} \right)^2 a^2 \frac{\sin^2 \pi qa}{(\pi qa)^2} \quad (1.9)$$

where $I(q) = 0$ when $q = 1/a$. This says that the diameter of the diffraction limited spot in one dimension of the intensity pattern for the coherent mixing is one-half that of a single beam. Compressing twice the intensity into half of the area means a fourfold increase in the peak power density. Even though the lasers emit Gaussian beams, the mathematics of plane waves is far simpler and more transparent. The far-field interference of both types of wavefronts gives the same results, but equation (1.9) describes the fringes within the Gaussian pattern.

When some degree of coherence exists among wavefronts, proper mixing of the waves produces near-field interference fringes in accordance with (1.5). The amount of coherence is characterized by measuring the visibility of the fringe pattern. The visibility is defined by

$$V = \frac{I_{\max} - I_{\min}}{I_{\max} + I_{\min}} \quad (1.10)$$

where I_{\max} and I_{\min} are the maximum and minimum intensities of two consecutive light and dark fringes, respectively. If $V = 1$ (high contrast fringes), the waves are completely coherent, but if there are no fringes, $V = 0$ and the waves

are incoherent.

Another practical military advantage of a coupled laser system is the property, as termed by the coupled devices community, of graceful degradation. For a single, high-energy laser, if a critical component fails, the laser cannot function and the mission can not be performed. If instead, a phase-locked coupled laser system is employed and one or several of the lasers are inoperative, the system can still be used as a weapon albeit at reduced effectiveness. For example, imagine the United States to have a coupled laser system of 10-10 kilowatt lasers for a total of 1 megawatt peak output power. Perhaps two component lasers of the system are down for maintenance. Instead of operating at the maximum performance level of 1 megawatt of peak phase-locked power, the system could still function at 640 kilowatts and continue to perform the defensive mission. Even if no phase locking occurred, the 10 laser system would generate 100 kilowatts of power showing that the coupled laser system exhibits several levels of fault tolerance. The numbers and the scenario previously described are fictitious, but the concepts involved in such an event are quite plausible.

D. History of Laser Coupling

In 1966, Stover and Steier of Bell Telephone Laboratories made what was perhaps the first attempt at coupling independent lasers by injection locking two frequency-stabilized He-Ne lasers ⁶. Man and Brillet duplicated the work in 1984 using two Ar-ion lasers by injecting the stabilized, single-frequency output of a master laser into a multiline/multimode slave laser and produced almost three

times the single frequency output of one laser ⁷. Even though injection locking is an excellent method for increasing the single-mode output power from lasers, the requirements for precision control of the system components are considerable and not always easy to satisfy. Another method of scaling laser power is the master oscillator/power amplifier (MOPA) ⁸. In a MOPA system, a relatively clean seed beam passes through one or more amplifiers in which the seed beam is amplified thereby increasing the beam intensity to higher power levels.

Both MOPA and injection locking have a critical dependence on a master oscillator. Should the master oscillator fail, there would be no output from the former, and only the unphased output of the slave lasers of the latter. Conventional coupling, however, not only eliminates the dependence on a master oscillator, but it also makes it possible to extract phase-locked energy on multiple wavelengths simultaneously. Palma, *et. al.* coupled 2, 4, and 6 unstable CO₂ lasers by injecting portions of the beams through holes in the the feedback mirrors and by using beamsplitters to reflect the beams into the other resonators ⁹. This work resulted in a coherent sum of 65% of the theoretical phase-locked intensity for the 6 laser experiment and 88% and 95% of the ideal intensities for 4 and 2 lasers, respectively. Bernard, Chodzko, and Mirels coupled two cw HF chemical lasers in unstable resonators by seeding each laser with 20% of the output power¹⁰. Even though the multiline fringe pattern had an overall visibility of 0.6, the visibility of the filtered $P_2(6)$ IIF laser line was nearly equal to one indicating that the transitions in each laser were almost completely coherent. Currently, Cunningham *et. al.* are undertaking a similar experiment with chemical oxygen-

iodine lasers (COIL) ¹¹.

E. Dissertation Outline

Although there have been a number of coupled-laser experiments, apparently none have made a parametric study of the effect of the transmitted coupling power on the coupled system, especially in multiline lasers with Doppler-broadened media in standing-wave cavities. This dissertation research focussed on the behavior of two coupled Ar-ion lasers both theoretically and experimentally. Ar-ion will definitely not be used in any high-energy laser system, but understanding the physics of coupling in Doppler-broadened media should be applicable to other systems whose media exhibit Doppler-broadened behavior such as HF or oxygen-iodine. Additionally, Ar-ion lasers can be operated for extended periods of time without the hazards associated with the highly toxic HF and COIL lasers.

Chapter II will derive from first principles the equations describing single mode laser operation, and then work through the important points of both the single- and two-mode coupled laser equations. The computer solutions to those equations for various tuning configurations are then examined. In Chapter III, the coupling experiment itself will be discussed showing the three configurations studied and the measurement procedures. Chapter IV will present and analyze the experimental results. Finally, Chapter V presents the conclusions and some recommendations for continued research in this area.

Chapter II. Coupled Laser Theory

Because many real lasers oscillate on many wavelengths and many modes for each wavelength, it is extremely difficult if not impossible to accurately model the complex behavior of a single laser let alone two or more coupled lasers. Despite the enormity of the real problem, simpler theories developed under suitable approximations produce significant and useful insights into the coupled laser processes. This chapter will begin with a cursory historical examination of coupled laser theory, which will be followed by a derivation of the equations for two, coupled, single-mode Fabry-Perot lasers. The solutions to the single-mode equations will be discussed along with their accompanying tuning curves. The chapter continues with the extension of the single-mode equations to describe two modes oscillating in each cavity and an examination of some of the interesting phenomena that were discovered during the solution of the two-mode equations.

A. History of Laser Coupling Theory

Since Spencer and Lamb first introduced their coupled-laser theory in 1972 ¹², the field has blossomed with many related theories; each seeking to expand the range of applicability of Spencer and Lamb's treatment, or study a different aspect of a coupled laser system. Palma, *et. al.* applied Spencer and Lamb's theory directly to two coupled CO₂ lasers ⁹, and Chow derived an analytical expression for the locking range in terms of changes in the cavity length ¹³. The original theory has also been modified by Mirels ¹⁴ to more accurately represent the physical coupling mechanism. These theories have dealt only with a single

mode oscillating in each cavity and, except for Mirels, with homogeneous laser media. Spencer and Lamb's theory is also limited to cases of weak coupling.

With the growing interest in coupled laser systems, the theories likewise expanded to more closely model the prevailing experimental research. Shakir and Chow, based on the fundamentals of Spencer and Lamb's theory, extended the coupled laser theory to model any number of lasers in a phased array with any amount of coupling ¹⁵. Their paper also introduced the concept of supermodes; laser modes which satisfy the boundary conditions of the composite resonator. Both Walsh ¹⁶ and Shakir and Erkkila ¹⁷ applied the Shakir and Chow supermode theory to CO₂ lasers; Walsh to Fabry-Perot resonators and Shakir and Erkkila to unstable resonators. Since coupled ring resonators offer the possibility of higher output power, Benda and Palma adapted the supermode theory to model such a system ¹⁸. Not all theories find their roots in Spencer and Lamb's model. Rinaldi and Erkkila introduced a new approach by treating the coupling as an injected signal and used a rate-equation approximation as the model for the laser medium¹⁹.

This dissertation also presents its own contribution to the increasing number of coupled laser theories by planting a seed in an area of interest that has apparently been overlooked. As stated above, the theories generally deal with single-mode, homogeneously broadened, coupled lasers. A logical extension is to model two modes oscillating in each cavity. The second theoretical section of this chapter performs that analysis by developing two-mode coupled laser equations for Doppler-broadened gain media. It should be noted that the single- and two-

mode theories developed here describe the behavior of a coupled-cavity laser system with one or two modes oscillating in each cavity.

B. Single-Mode Theory

The objective of this research was to study the coupling of two standing-wave Ar-ion lasers. Although the theories fall far short of describing the complex interactions between the up to ten possible different wavelengths and dozens of modes in the real system, analysis of the coupled-laser theory aids in understanding some of the processes involved in coupling. If simple systems cannot be understood, then there is little hope of interpreting any results from more complicated experiments. This section will derive the single-mode coupled laser equations from the principles of electrodynamics. These equations will then be applied to coupled Ar-ion lasers and the resulting solutions will be examined and discussed.

The following derivation closely parallels that first introduced by Lamb in 1964 in his now famous paper on the "Theory of an Optical Maser"²⁰. It is reassuring to know that the derivation of the coupled-laser equations begins with the familiar Maxwell's equations. First, a driven wave equation describes the field in each cavity of Figure 2.1:

$$\frac{\partial^2 E_n(z,t)}{\partial t^2} + 2\Gamma_n \frac{\partial E_n(z,t)}{\partial t} - \frac{1}{\epsilon_0 \mu_0} \frac{\partial^2 E_n(z,t)}{\partial z^2} = -\frac{1}{\epsilon_0} \frac{\partial^2 P_n(z,t)}{\partial t^2} \quad (2.1)$$

where $n = A, B$ (the cavity designations); E_n is the complex field in each cavity; Γ_n are the cavity losses; and P_n is the complex polarization of the Doppler-

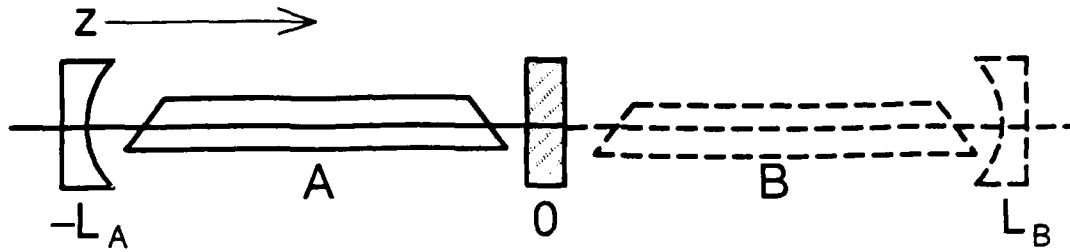


Figure 2.1: Geometry for coupled laser theory.

broadened medium. Since the spatial variations of the field inside the cavity are not important to the steady-state solutions of the output wave, the z -dependence is removed by performing a Fourier transform on the wave equation. Equation (2.1) is multiplied by $\frac{2}{L_A} \sin k_A(z + L_A)$ and integrated over Z from $-L_A$ to 0.

By defining the Fourier transform of the mode amplitude E_A by

$$\mathbf{E}_A(t) = \frac{2}{L_A} \int_{-L_A}^0 \sin k_A(z + L_A) E_A(z, t) dz \quad (2.2)$$

the resultant wave equation becomes

$$\ddot{\mathbf{E}}_A(t) + 2\Gamma_A \dot{\mathbf{E}}_A(t) - \frac{1}{\epsilon_0 \mu_0} \frac{2}{L_A} \int_{-L_A}^0 \sin k_A(z + L_A) \frac{\partial^2 E_A(z, t)}{\partial z^2} dz = -\frac{1}{\epsilon_0} \ddot{\rho}_A(t) \quad (2.3)$$

where ρ_A is the Fourier transform of the polarization. If the two outside mirrors have reflectivities of 100%, then the boundary conditions for the laser resonator are

$$E_A(0, t) = E_A(-L_A, t) = 0 \quad (2.4)$$

Integrating by parts twice eliminates the z -dependence from equation (2.3), and

the wave equation simplifies to

$$\ddot{\mathbf{E}}_A(t) + 2\Gamma_A \dot{\mathbf{E}}_A(t) + \frac{k_A^2}{\epsilon_0\mu_0} \mathbf{E}_A(t) = -\frac{1}{\epsilon_0} \ddot{\rho}_A(t) \quad (2.5)$$

Two further simplifications may be made by noting that $\Omega_A = k_A c$ is the bare cavity frequency and $(\epsilon_0\mu_0)^{-1} = c^2$:

$$\ddot{\mathbf{E}}_A(t) + 2\Gamma_A \dot{\mathbf{E}}_A(t) + \Omega_A^2 \mathbf{E}_A(t) = -\frac{1}{\epsilon_0} \ddot{\rho}_A(t) \quad (2.6)$$

In the pioneering work on coupled laser resonators developed by Spencer and Lamb ¹², a "dielectric bump", an infinitely narrow region of change in the dielectric permittivity between the two cavities, was the boundary condition through which the lasers were allowed to interact. The dielectric bump mirror model is mathematically described by

$$\epsilon(z) = \epsilon_0 [1 + \frac{\eta}{k} \delta(z)] \quad (2.7)$$

where $\eta = 2 (R_c / T_c)^{1/2}$ and R_c , T_c are the reflectivity and transmissivity of the coupling mirror, respectively. The dielectric bump changes the boundary condition at $E(0,t)$ and would have been included during the integration by parts if this derivation was strictly following that of Spencer and Lamb. Not only is the dielectric bump completely unphysical because no reflection occurs at an interface between two media of the same index of refraction, but the Spencer and Lamb model also allows no provision for output coupling and therefore makes the model somewhat artificial. In 1986, Mirels improved the model and made it more

representative of the actual coupling involved by replacing the dielectric bump term with a net perturbation per round trip term, accounting for light leakage through the output mirrors in the cavity loss terms, while retaining the fundamental medium interaction terms of Spencer and Lamb ¹⁴. Since this derivation uses Mirels' coupling terms, the development continues from equation (2.6).

Even though the problem has been reduced to a second-order differential equation, it is difficult to solve in this form, therefore some approximations must be made. Let the electric field and polarization be represented by complex, sinusoidally varying functions:

$$\begin{aligned} \mathbf{E}_A(t) &= E_A(t) e^{-i[\omega t + \phi_A(t)]} \\ \rho_A(t) &= P_A(t) e^{-i[\omega t + \phi_A(t)]} \end{aligned} \quad (2.8)$$

By invoking the slowly varying amplitude and phase approximation, all the second order terms in $E_A(t)$ and $\phi_A(t)$ can be neglected, and only the zeroth order term in polarization is retained. Since the terms containing $\Gamma_A \dot{E}_A(t)$ and $\Gamma_A \dot{\phi}_A(t)$ are roughly 10^7 times smaller than the others, they may also be eliminated. After making these simplifications, the resultant first-order coupled differential equation in $\dot{E}_A(t)$ and $\dot{\phi}_A(t)$ becomes

$$-2i\omega\dot{E}_A(t) + E_A(t) [\Omega_A^2 - (\omega + \dot{\phi}_A(t))^2] - 2i\omega\Gamma_A E_A(t) = \frac{\omega^2}{\epsilon_0} P_A(t) \quad (2.9)$$

Because optical frequencies are on the order of 10^{15} , factors of 2 are also negligible, so

$$\Omega_A \approx \omega \quad (2.10)$$

After dropping the $\dot{\phi}^2(t)$ term, the quadratic frequency expression can be reduced to

$$[\Omega_A^2 - [\omega + \dot{\phi}_A(t)]^2] \approx 2\omega [\Omega_A - \omega - \dot{\phi}_A] \quad (2.11)$$

Making this substitution and dividing equation (2.9) by 2ω gives

$$\begin{aligned} -i\dot{E}_A(t) + E_A(t) [\Omega_A - \omega - \dot{\phi}_A] - i\Gamma_A E_A &= \frac{\omega}{2\epsilon_0} P_A(t) \\ &= \frac{\omega}{2\epsilon_0} [\text{Re}\{P_A(t)\} + i \text{Im}\{P_A(t)\}] \end{aligned} \quad (2.12)$$

Equating the real and imaginary parts of both sides of the expression gives two first-order coupled differential equations in field and phase:

$$\dot{E}_A + \Gamma_A E_A = -\frac{\omega}{2\epsilon_0} \text{Im } P_A(t) \quad (2.13)$$

$$\dot{\phi}_A + \omega = \Omega_A - \frac{\omega}{2\epsilon_0} E_A^{-1} \text{Re } P_A(t)$$

A similar pair of expressions results from the treatment of E_B .

Once the field and phase equations have been obtained, expressions for the polarization of the medium in each cavity must be derived. This derivation involves the quantum mechanics of the laser medium and is specific to whether the medium is homogeneously or inhomogeneously broadened. Because the formulation of the polarization for a Doppler-broadened medium is long and difficult and provides little that is necessary to the understanding of this derivation, the results will be transferred directly. (For a complete derivation of both the

inhomogeneous and homogeneous media polarization, consult Lamb ²⁰, pp.

A1430-A1438, or Sargent, *et. al.* ²¹, pp. 144-152.) Finally, the field and phase equations describing a single mode oscillating in a Doppler-broadened medium of a Fabry-Perot resonator are

$$\dot{E}_n = (\alpha_n - \beta_n I_n) \quad (2.14)$$

$$\omega_n + \dot{\phi}_n = \Omega_n + \sigma_n - \rho_n I_n \quad (2.15)$$

where the symbols and coefficients are defined in Table 2.1.

Before the coupling terms are derived, it is useful at this point to examine the details of the coupling mirror. The mirror model used in this analysis is a single, non-absorbing, reflective surface detached from any glass substrate. The surface is mathematically described by complex coefficients of reflection and transmission which are assumed to be identical for waves incident on either side of the coupling mirror (See Figure 2.2):

$$r_A = r_B = r = r e^{i\phi_{\text{reflected}}} = \sqrt{R_c} e^{i\phi_r} \quad (2.16)$$

$$t_A = t_B = t = t e^{i\phi_{\text{transmitted}}} = \sqrt{T_c} e^{i\phi_t} \quad (2.17)$$

To couple the two pairs of equations for the field and phase of the modes in each cavity, Mirels' net perturbation per round trip coupling terms ¹⁴ are appended to equations (2.14) and (2.15). When photons cross the coupling mirror, there is a perturbation to the parent field and phase as shown in Figure 2.3, and

Table 1: Symbols and Definitions

$\alpha_n = F_{1n} e^{-\left(\frac{\gamma}{\gamma_d}\right)^2 \xi_n^2} - F_{2n}$	Linear Net Gain Coefficient
$\beta_n = F_{3n} (1 + \mathcal{Z}(\xi_n))$	Self-Saturation Coefficient
$\sigma_n = 2 F_{1n} e^{-\left(\frac{\gamma}{\gamma_d}\right)^2 \xi_n^2} \frac{\gamma}{\gamma_d} \xi_n \int_0^{\xi_n} e^{x^2} dx$	Linear Mode Pushing Coefficient
$\rho_n = F_{3n} \xi_n \mathcal{Z}(\xi_n)$	Self-Pushing Coefficient
$\theta_{nm} = F_{3n} [\mathcal{Z}(\frac{1}{2}\xi_n + \frac{1}{2}\xi_m) + \mathcal{Z}(\frac{1}{2}\xi_n - \frac{1}{2}\xi_m)]$ $+ F_{3n} \mathcal{Z}(\xi_n) \mathcal{Z}(\xi_n - \xi_m) [1 - \xi_n(\xi_n - \xi_m)]$ $+ F_{3n} \mathcal{Z}(\xi_n - \xi_m) \mathcal{Z}(\frac{1}{2}\xi_n - \frac{1}{2}\xi_m) [1 - \frac{1}{2}(\xi_n - \xi_m)^2]$	Cross Saturation Coefficient
$\tau_{nm} = \frac{1}{2} F_{3n} [(\xi_n + \xi_m) \mathcal{Z}(\frac{1}{2}\xi_n + \frac{1}{2}\xi_m) + (\xi_n - \xi_m) \mathcal{Z}(\frac{1}{2}\xi_n - \frac{1}{2}\xi_m)]$ $- F_{3n} \mathcal{Z}(\xi_n) \mathcal{Z}(\xi_n - \xi_m) (2\xi_n - \xi_m)$ $- \frac{3}{2} F_{3n} \mathcal{Z}(\xi_n - \xi_m) \mathcal{Z}(\frac{1}{2}\xi_n - \frac{1}{2}\xi_m) (\xi_n - \xi_m)$	Cross Pushing Coefficient
$F_{1n} = F_{3n} = \frac{\bar{N}}{N_T} \Gamma = \frac{g_0 c l}{2 L}$	Peak Unsaturated Gain Coefficient
$F_{2n} = \Gamma = \frac{c}{2L} \ln \left(\frac{1}{\sqrt{R_0 R_c}} \right)$	Distributed Cavity Attenuation Coefficient
$M_n = \frac{c}{2L} \left(\frac{T_c}{R_c} \right)^{\frac{1}{2}} e^{i\psi}$	Distributed Coupling Mirror Coefficient
$\xi_n = (\omega_0 - \omega_n)/\gamma$	Normalized Laser Frequency Detuning from Line Center
$\Delta_n = (\omega_0 - \Omega_n)/\gamma$	Normalized Cavity Frequency Detuning from Line Center
$\mathcal{Z}(x) = (1 + x^2)^{-1}$	Lorentzian Line Profile

Table 2.1: Symbols and Definitions (cont'd)

$\psi = \phi_t - \phi_r$	Phase Introduced by Coupling Mirror
$\gamma = \frac{1}{2} \frac{\bar{N}}{N_T} \frac{1}{\tau_{rad}}$	Power-broadened Natural Linewidth (HWHM)
$2\delta = \frac{2\pi c}{\gamma L}$	Normalized Free Spectral Range
$\phi_n = \phi_{Bn} - \phi_{An}$	Mode Phase Difference
ω_n	Laser Oscillation Frequency
ω_0	Line Center Frequency
Ω_n	Cavity Resonance Frequency
R_0	Output Mirror Reflectivity
R_c	Coupling Mirror Reflectivity
T_c	Coupling Mirror Transmission
g_0	Single-Pass Gain
l	Length of Gain Medium
L	Cavity Length

$$\Delta E_A = \left(\frac{T_c}{R_c} \right)^{\frac{1}{2}} E_B \cos(\phi_B - \phi_A + \psi) \quad (2.18)$$

$$\Delta \phi_A = \left(\frac{T_c}{R_c} \right)^{\frac{1}{2}} \frac{E_B}{E_A} \sin(\phi + \psi) \quad (2.19)$$

When all the pieces are assembled, the single-mode coupled laser equations become

$$\frac{dE_A}{dt} = (\alpha_1 - \beta_1 I_A) E_A + M_A E_B \cos(\phi + \psi) \quad (2.20)$$

$$\frac{dE_B}{dt} = (\alpha_2 - \beta_2 I_B) E_B + M_B E_A \cos(\phi - \psi) \quad (2.21)$$

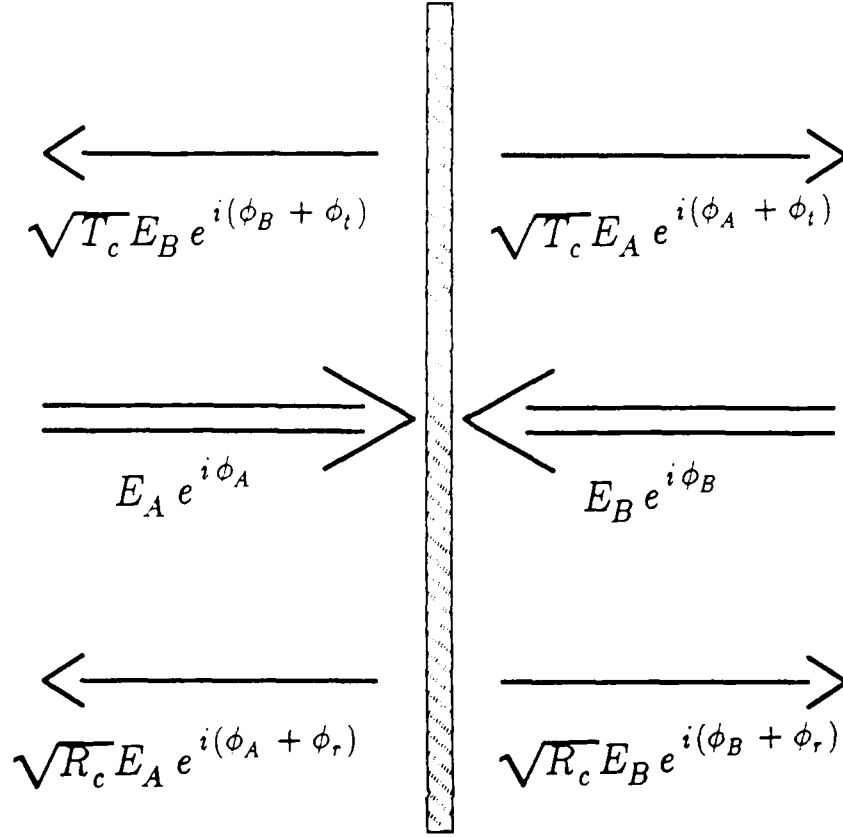


Figure 2.2: Reflected and transmitted waves at the coupling mirror interface.

$$\frac{d\phi_A}{dt} = \gamma(\xi - \Delta_A) + \sigma_1 - \rho_1 I_A + M_A \left(\frac{E_B}{E_A} \right) \sin(\phi + \psi) \quad (2.22)$$

$$\frac{d\phi_B}{dt} = \gamma(\xi - \Delta_B) + \sigma_2 - \rho_2 I_B + M_B \left(\frac{E_A}{E_B} \right) \sin(\phi - \psi) \quad (2.23)$$

whose symbols and coefficients are also defined in Table 2.1. These equations model the laser cavities and modes depicted in Figure 2.4(a).

In order to solve the equations in the steady state, the time derivatives were set to zero and the Jacobian Matrix was constructed to solve the system for the variables I_A , I_B , ξ , and $\sin\phi$ using the Newton-Raphson method²². Self-

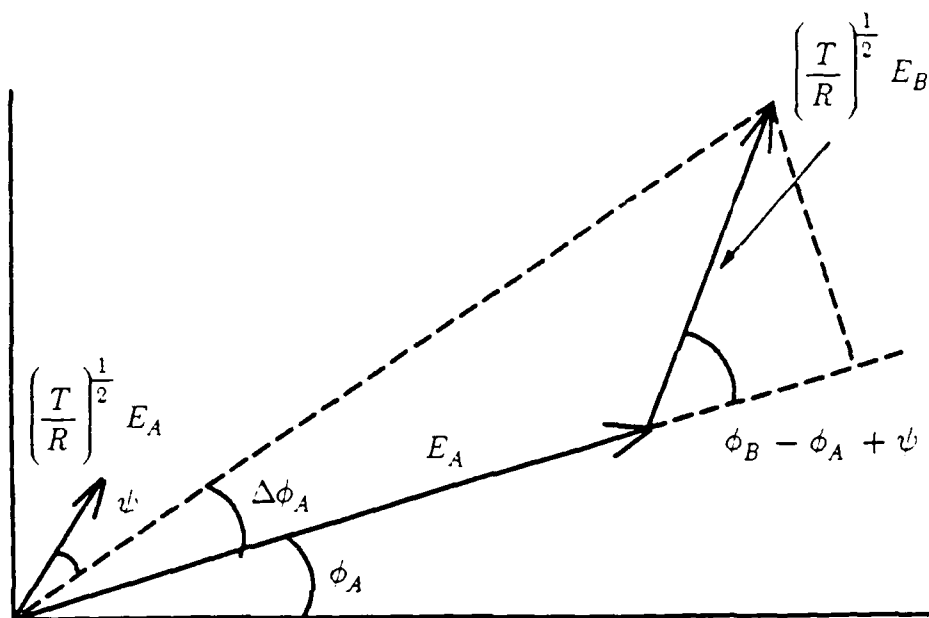


Figure 2.3: Geometry to derive net perturbation per round trip coupling terms.

consistent solutions were allowed to converge to within one part in a million by a computer program coded on a Zenith Z-248 computer. Each solution set was checked for stability by performing a perturbation calculation on the time-dependent field equations and an equation comprised of the difference between the two phase equations. If all the real parts of the eigenvalues of the perturbation matrix were negative, then the solution was considered stable. The details of the reduction of the equations to expressions readable by a computer and the computer code used to generate the solutions can be found in Appendix A.

The solutions to the coupled laser equations with Doppler-broadened media permitted the evaluation of the intensity of each mode, I_A and I_B , the total intensity, I_c , which is the coherent sum of the mode intensities, the offset of the lasing frequency from the line center frequency, ξ , and the phase difference between the

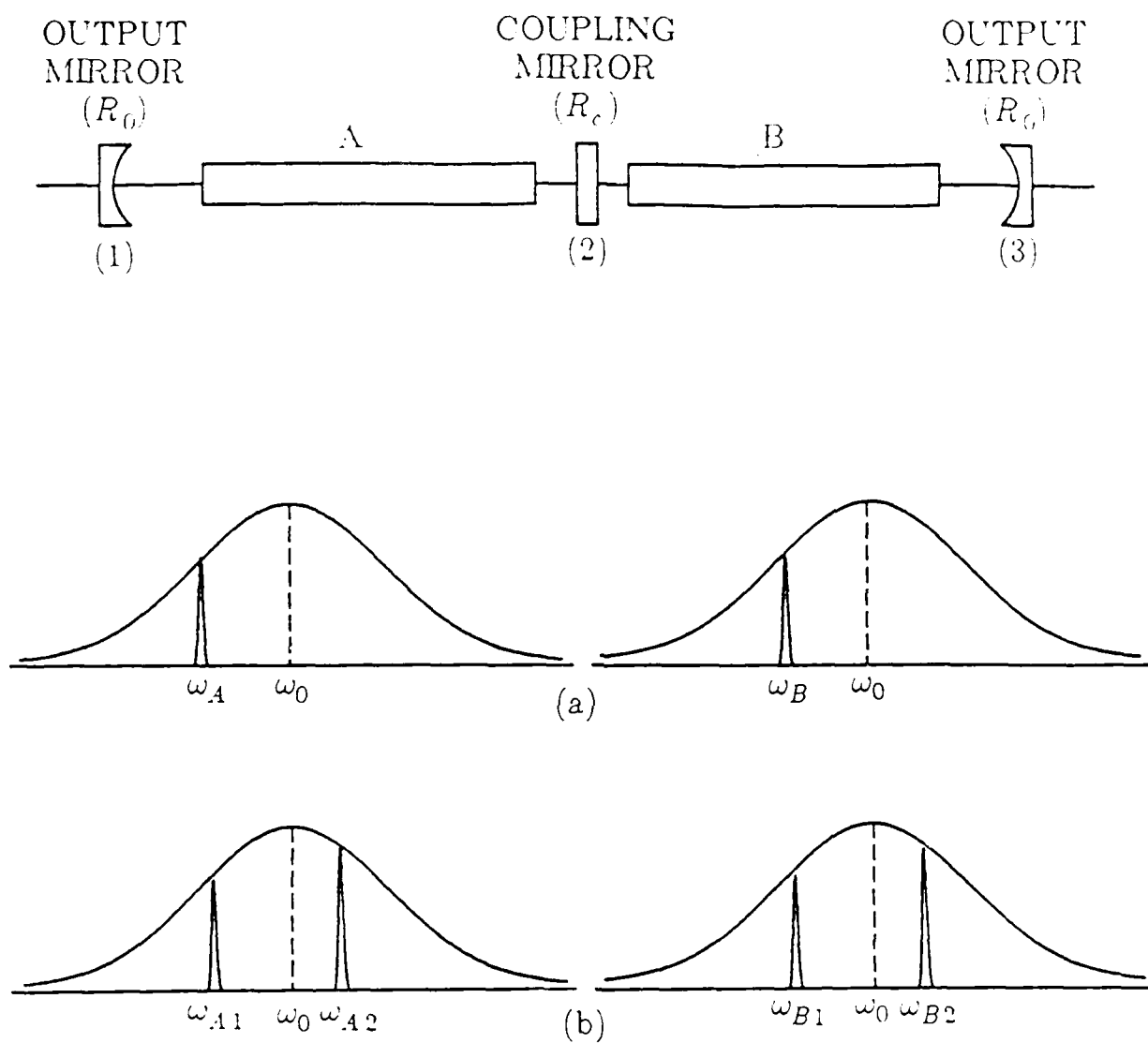


Figure 2.4: Schematic diagram of the coupled laser system for (a) a single mode oscillating in each cavity and (b) two modes oscillating in each cavity.

two modes, ϕ . The parameters describing the Ar-ion lasers are found in

Table 2.2. To generate the tuning curves, the mirrors were translated (by varying the cavity frequency term, Ω , contained in the Δ term of equations (2.22) and

(2.23)) in three different combinations. Each ω term contains the bare cavity frequency, Ω , implicitly, but ω need not be determined for each mirror displacement. The change in the bare cavity frequency is absorbed into the lasing frequency, ω , during each step of the iterative solution process. Therefore, the implicit relationship between ω and Ω is satisfied once a self-consistent solution is reached.

Table 2.2: Ar-ion Laser Parameters

$L = 1.75 \text{ m}$	$R_c = 0.6 \text{ to } 0.95$
$l = 0.38 \text{ m}$	$\nu_{FSR} = 85.6 \text{ MHz}$
$\gamma_d = 2 \pi \times 4 \text{ GHz}$	$\tau_{rad} = 7.5 \text{ ns}^{24}$
$g_0 = 0.01 \text{ cm}^{-1}^{23}$	$\lambda = 514.5 \text{ nm}$

Figures 2.5 (a)-(c) show the case of a symmetric tuning in which both output mirrors were translated simultaneously (mirrors 1 and 2 of Figure 2.4) while maintaining equal cavity lengths. As expected from the symmetric tuning, the intensities in each cavity both display the same behavior and, as the mode crosses the gain center, it burns out the Lamb dip. Although it is difficult to see on the figure, the minimum of the Lamb dip is slightly offset from the point where the resonator frequency is equal to the gain center frequency due to the phase shift, ψ , encountered as the light wave traverses the coupling mirror. Including this additional phase perturbation displaces the lasing frequency from the cavity

frequency. This displacement is more pronounced for two-mode coupling and will be discussed more extensively later in the chapter. Not surprisingly, the two modes exhibit zero phase difference in this case and the solutions remain stable throughout the tuning range. For the curves depicted by Figures 2.6 (a)-(c), mirrors 1 and 2 were kept stationary while mirror 3 was translated. The intensity curve (Figure 2.6(a)) shows that the maximum total intensity is reached when the two cavity lengths are made equal even though neither mode intensity is at its peak. This results because the phase angle is initially zero allowing the largest contribution from the cross product term of the coherent intensity sum. The final tuning case involved translating only the coupling mirror (mirror 2 of Figure 2.4) preserving a constant total cavity length (Figures 2.7 (a)-(c)). Once again, the coherent intensity was a maximum when the cavity lengths were equal, but in this instance, both the intensity and frequency curves are symmetric about the zero detuning point.

Notice also that the right side of Figure 2.6 (a) matches the intensity to the right of zero in Figure 2.7 (a). The reason this occurs is because it is immaterial which of the mirrors is translated when changing the cavity length insofar as one laser is concerned. Had the other output mirror of the asymmetric tuning been moved, then the left sides of the two figures would show identical intensities. One further piece of information concerning the desired operating point of the coupled laser system is available from the tuning curves. In order to achieve the maximum power output from the single-mode coupled laser system, both cavity lengths must be equal to each other while the laser frequencies should be detuned

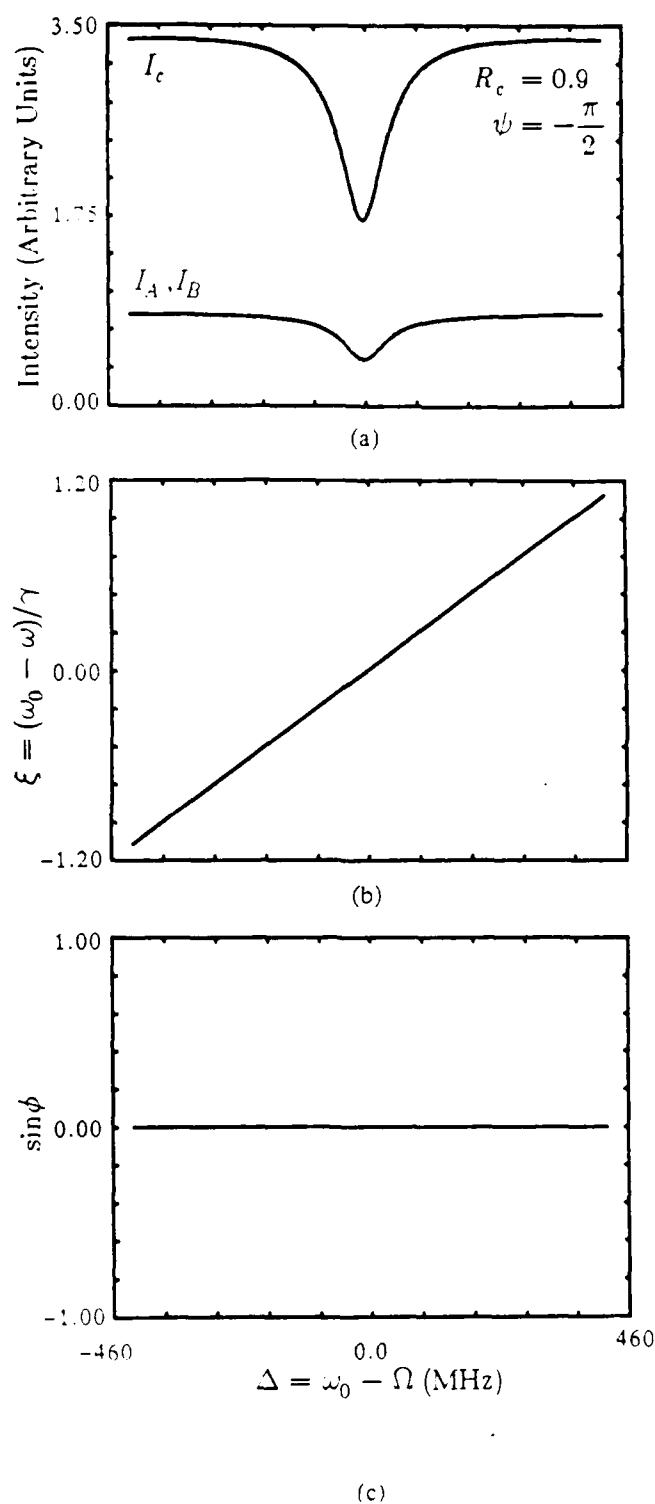


Figure 2.5: Intensity, frequency detuning, and phase as a function of cavity detuning for single-mode coupling for the case of translating both output mirrors. The solutions are stable for all displacements.

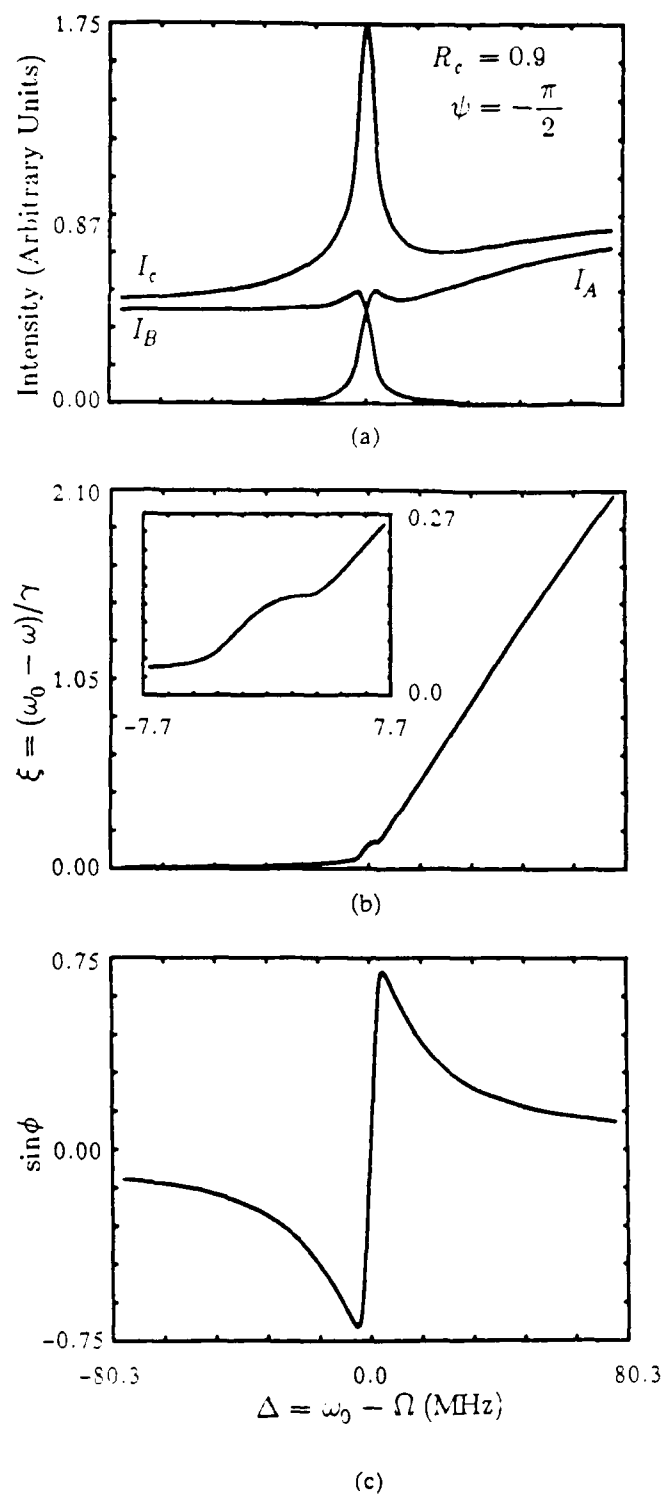


Figure 2.6: Intensity, frequency detuning, and phase as a function of cavity detuning for single-mode coupling for the case of translating a single output mirror. The solutions are stable from -3.48 MHz to +3.14 MHz.

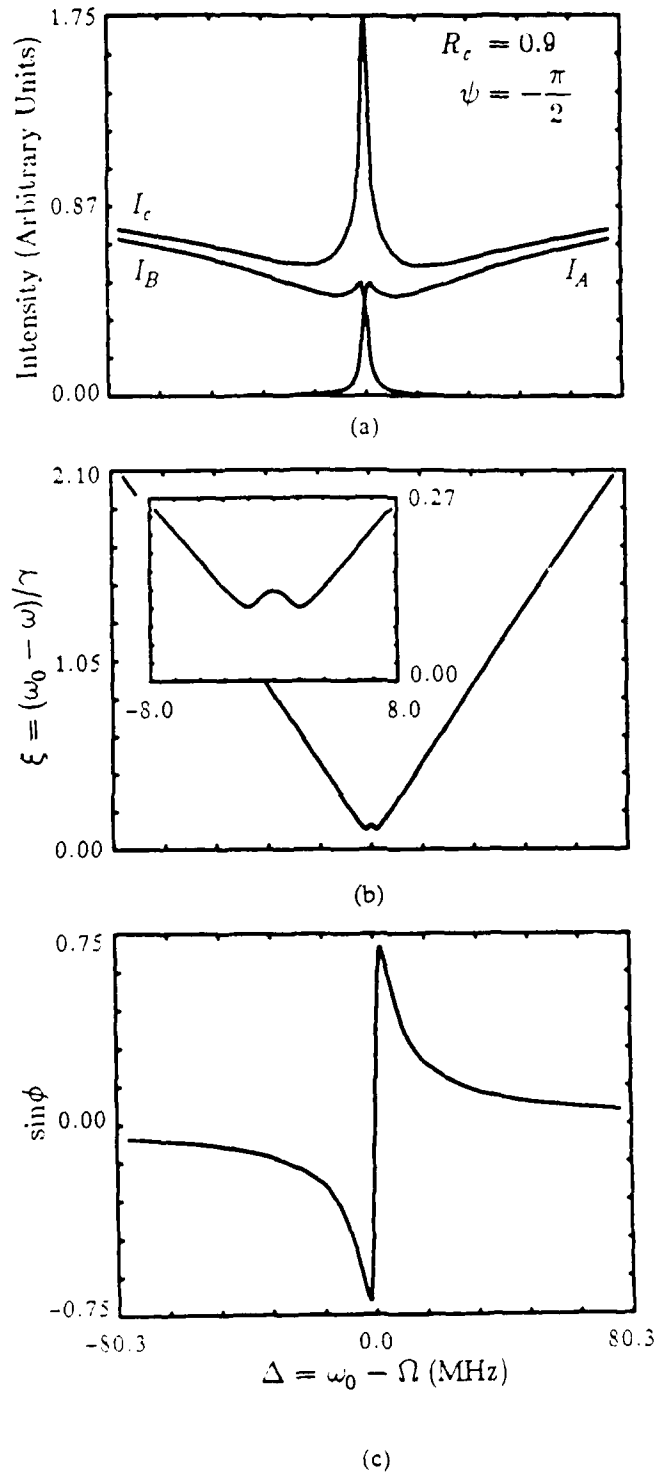


Figure 2.7: Intensity, frequency detuning, and phase as a function of cavity detuning for single-mode coupling for the case of translating the coupling mirror. The solutions are stable from -1.65 MHz to +1.65 MHz.

from the gain center to avoid the intensity drop which results from the hole-burning associated with the Lamb dip.

One motivation for studying coupled lasers is to determine the set of conditions that is necessary to generate the maximum stable coherent output. Stable operating regions were calculated for different values of the coupling mirror ranging from $R_c = 0.95$ to $R_c = 0.6$. Although there are several interpretations of the definition of locking range, the term locking range as used in this paper refers to the frequency region over which the solutions to the time-dependent coupled laser equations remained stable as determined by the perturbation calculations:

$$\frac{\Delta L}{\lambda} = \frac{\Delta \omega L}{2\pi c} \quad (2.24)$$

The upper curve of Figure 2.8 shows the locking ranges for the case of translating a single output mirror with an internal phase shift of $\psi = -\pi/2$ which was chosen to match the phase shift derived by Spencer and Lamb¹². As stated previously, when both output mirrors were translated, the solutions remained stable, but when tuning only the center mirror, the locking ranges were almost exactly one half of those resulting from tuning a single output mirror.

The internal phase shift encountered by the coupling beam as it crosses the coupling mirror depends on the optical length of the reflective surface of the mirror and the phase change introduced into the wave upon reflection at the mirror interface. Although exact determination of the phase shift is difficult, the choice of ψ is not arbitrary. The complex reflectivities and transmissivities must obey conservation of energy according to²⁵

$$r_A t_B^* + t_A r_B^* = 0 \quad (2.25)$$

If the reflection phase change is chosen to be π , then the only allowable values for ψ are $\pm\pi/2$.

As the amount of coupling increases, the locking range increases nearly linearly. The curve ends at 40% coupling because the population inversion ratio, \bar{N}/N_T , falls below 1 for any larger value of transmission. With larger coupling coefficients which correspond to lower reflectivities of the coupling mirror, each cavity can no longer sustain oscillation so the character of the coupled laser system changes. Instead of two independent lasers coupled through a common mirror, the system becomes a single laser oscillating between the two output mirrors with a phase disturbance in the center caused by the coupling mirror in the cavity interior.

The plateau at 5% transmission shows that only a small amount of coupling is required to initiate stable, phase-locked operation, but the cavity length restrictions necessary for phase locking are quite severe. For wavelengths on the order of $.5 \mu m$ for Ar-ion lasers, the corresponding locking ranges indicate that the laser cavities must be equal to each other to within about 100 nm. Control of this magnitude for a 1.75 m-long cavity would be an extraordinary engineering accomplishment. Since the locking range for stable operation is wavelength dependent, these control problems are relaxed somewhat for longer wavelength lasers. The values of the locking ranges determined by Palma *et.al.*⁹ in their theoretical analysis of coupled CO₂ lasers are on the same order as those computed here for the Ar-ion lasers, but with a $10.6 \mu m$ operating wavelength for CO₂, the lengths

of the two cavities can differ by several microns and still maintain single-mode, phase-locked oscillation.

Remember that the theory developed by Spencer and Lamb accurately models only cases of weak coupling. Weak coupling is a frequently-used but rarely-defined term which can be thought of as a coupled system in which the fraction of the coupling intensity compared to the cavity's internal intensity is small. Even though the theory in this dissertation was applied to lasers with as high as 40% coupling, no inconsistencies surfaced in the results, and therefore the risk was warranted. A strong coupling theory was developed by Chow ²⁶ in which the laser modes are expanded in terms of the composite resonator or supermodes and applicable to any amount of coupling.

C. Two-Mode Theory

Lamb laid the foundation for the development of multimode coupled laser theory by deriving the field and phase equations for two and three modes lasing in a single cavity ²⁰, but the application of these equations to coupled laser systems seems to have escaped the attention of researchers. Although mathematically not difficult to manipulate, the two-mode coupled Fabry-Perot laser equations contain many terms which generate long expressions for derivatives that must be carefully coded to produce computer solutions. This snowballing mathematical mass serves as an effective deterrent to pursuing multimode coupled laser theory, and the law of diminishing returns quickly manifests itself. Nevertheless, an interesting physical phenomenon was discovered during analysis of the two-mode theory.

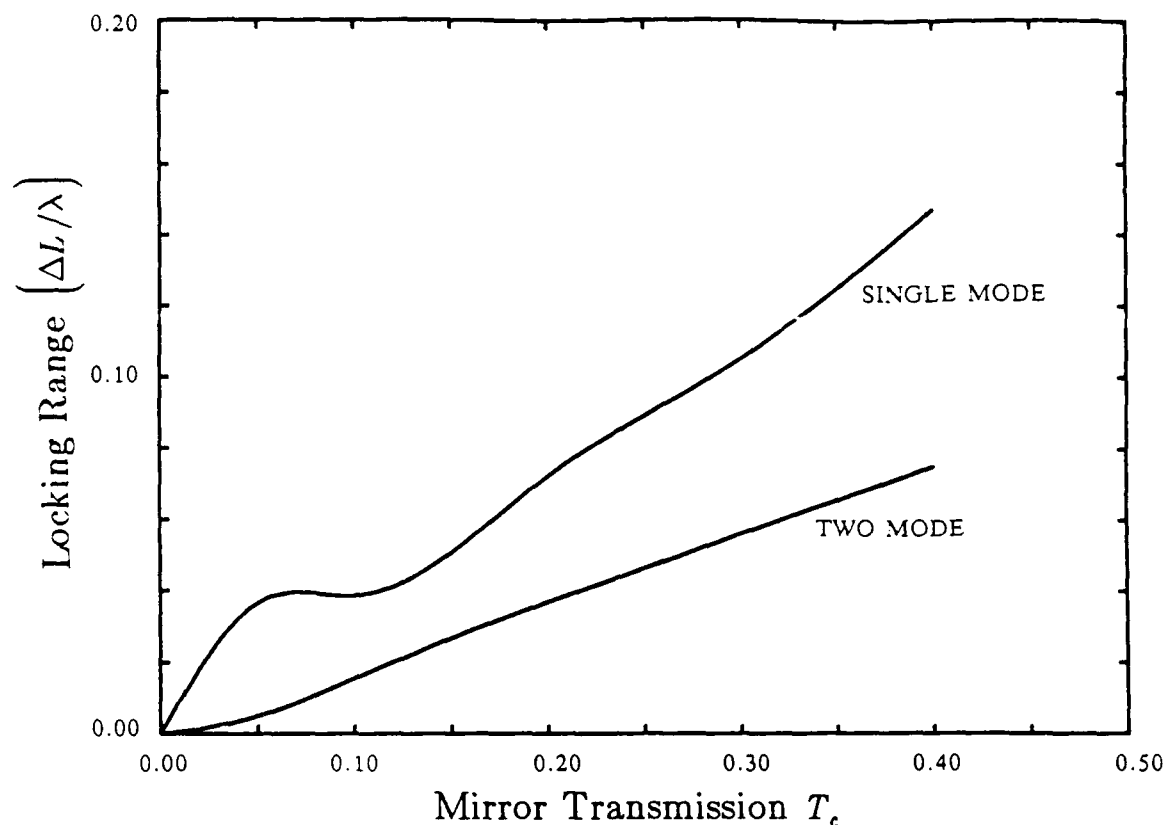


Figure 2.8: Locking range as a function of coupling mirror transmission for both single- and two-mode coupling during translation of a single output mirror.

Examination of the two-mode coupled laser system (represented pictorially in Figure 2.5(b)) closely paralleled that of the single mode case. It is important to note that the two-mode theory describes only two modes even though a real laser could sustain all the modes in the region of the gain curve above the threshold. The tuning curves were again created by translating the same mirror combinations, and the solutions for I_{A1} , I_{A2} , I_{B1} , I_{B2} , ξ_1 , ξ_2 , $\sin\phi_1$, and $\sin\phi_2$ were obtained by applying the Newton-Raphson method to the eight coupled equations. The eigenvalues, however, were numerically determined for the 6×6 perturbation

matrix using a program for computing the eigenvalues of an upper Hessenburg matrix ²⁷. The preparation of the two-mode equations for solution along with the computer program used to solve the system are also included in Appendix A.

To construct the two-mode coupled laser equations, Mirels' round-trip perturbation terms were added to Lamb's medium expressions for each pair of like-frequency modes. The net perturbation per round trip coupling terms for the second mode in each cavity are formed in exactly the same manner as those for the single-mode treatment except the subscripts are changed to indicated the new mode. With an additional mode oscillating in each cavity, it seemed necessary to allow the adjacent longitudinal modes from each cavity to interact with their respective mode pairs in the cross-saturation and cross-pushing terms. Because the adjacent longitudinal mode from the coupled cavity oscillates at the same frequency as the mode included in the cross terms, those two waves (adjusted by the proper phases and reflectivities or transmissivities) were allowed to mix coherently according to the general form of the expression

$$| \sqrt{R_c} E_{A_n} e^{i(\phi_{A_n} + \phi_r)} + \sqrt{T_c} E_{B_n} e^{i(\phi_{B_n} + \phi_t)} |^2 \quad (2.26)$$

The result of this amalgamation is equations (2.27)-(2.34) whose coefficients are defined in Table 2.1.

$$\begin{aligned} \frac{\partial E_{A1}}{\partial t} = E_{A1} [\alpha_1 - \beta_1 I_{A1} - \theta_{12} (R_c I_{A2} + T_c I_{B2} + 2\sqrt{R_c T_c} E_{A2} E_{B2} \cos(\phi_2 + \psi))] \\ + M_A E_{B1} \cos(\phi_1 + \psi) \end{aligned} \quad (2.27)$$

$$\begin{aligned} \frac{\partial E_{A2}}{\partial t} = & E_{A2} [\alpha_2 - \beta_2 I_{A2} - \theta_{21} (R_c I_{A1} + T_c I_{B1} + 2\sqrt{R_c T_c} E_{A1} E_{B1} \cos(\phi_1 + \psi))] \\ & + M_A E_{B2} \cos(\phi_2 + \psi) \end{aligned} \quad (2.28)$$

$$\begin{aligned} \frac{\partial E_{B1}}{\partial t} = & E_{B1} [\alpha_1 - \beta_1 I_{B1} - \theta_{12} (R_c I_{B2} + T_c I_{A2} + 2\sqrt{R_c T_c} E_{A2} E_{B2} \cos(\phi_2 - \psi))] \\ & + M_B E_{A1} \cos(\phi_1 - \psi) \end{aligned} \quad (2.29)$$

$$\begin{aligned} \frac{\partial E_{B2}}{\partial t} = & E_{B2} [\alpha_2 - \beta_2 I_{B2} - \theta_{21} (R_c I_{B1} + T_c I_{A1} + 2\sqrt{R_c T_c} E_{A1} E_{B1} \cos(\phi_1 - \psi))] \\ & + M_B E_{A2} \cos(\phi_2 - \psi) \end{aligned} \quad (2.30)$$

$$\begin{aligned} \frac{\partial \phi_{A1}}{\partial t} = & \gamma (\xi_1 - \delta_A - \Delta_A) + \sigma_1 - \rho_1 I_{A1} \\ & - \tau_{12} [R_c I_{A2} + T_c I_{B2} + 2\sqrt{R_c T_c} E_{A2} E_{B2} \cos(\phi_2 + \psi)] + M_A \left(\frac{E_{B1}}{E_{A1}} \right) \sin(\phi_1 + \psi) \end{aligned} \quad (2.31)$$

$$\begin{aligned} \frac{\partial \phi_{A2}}{\partial t} = & \gamma (\xi_2 + \delta_A - \Delta_A) + \sigma_2 - \rho_2 I_{A2} \\ & - \tau_{21} [R_c I_{A1} + T_c I_{B1} + 2\sqrt{R_c T_c} E_{A1} E_{B1} \cos(\phi_1 + \psi)] + M_A \left(\frac{E_{B2}}{E_{A2}} \right) \sin(\phi_2 + \psi) \end{aligned} \quad (2.32)$$

$$\begin{aligned} \frac{\partial \phi_{B1}}{\partial t} = & \gamma (\xi_1 - \delta_B - \Delta_B) + \sigma_1 - \rho_1 I_{B1} \\ & - \tau_{12} [R_c I_{B2} + T_c I_{A2} + 2\sqrt{R_c T_c} E_{A2} E_{B2} \cos(\phi_2 - \psi)] - M_B \left(\frac{E_{A1}}{E_{B1}} \right) \sin(\phi_1 - \psi) \end{aligned} \quad (2.33)$$

$$\begin{aligned} \frac{\partial \phi_{B2}}{\partial t} = & \gamma (\xi_2 + \delta_B - \Delta_B) + \sigma_2 - \rho_2 I_{B2} \\ & - \tau_{21} [R_c I_{B1} + T_c I_{A1} + 2\sqrt{R_c T_c} E_{A1} E_{B1} \cos(\phi_1 - \psi)] - M_B \left(\frac{E_{A2}}{E_{B2}} \right) \sin(\phi_2 - \psi) \end{aligned} \quad (2.34)$$

Since the equations did not explicitly contain two different frequencies, the computer program relaxed to a single intensity-phase solution satisfying all eight of the coupled equations. It was therefore necessary to artificially split the coded fre-

quencies by the free spectral range of the cavity (26) to force oscillation at two distinct frequencies.

Since the principal reason for studying coupled laser systems is the potential increase in the laser output power, the concept of a multifrequency intensity sum must be introduced. Electric fields oscillating at different frequencies add as simple intensities, but fields with the same frequency combine according to

$$I_c = E_A^2 + E_B^2 + 2E_A E_B \cos(\phi_B - \phi_A) \quad (2.35)$$

For the multimode intensities considered in the present analysis, it is presumed that the outputs from both lasers travel identical paths and are superposed. The mode oscillating at ω_{A1} is at the same frequency as the mode at ω_{B1} , therefore the associated fields add coherently and similarly for the modes at ω_{A2} and ω_{B2} . In addition, since the phases ϕ_1 and ϕ_2 are equal or nearly equal in each of the three tuning configurations for all mirror displacements, it can be assumed to a good approximation that the maxima and minima of the resultant interference fringes produced by the paired fields occur at the same points in space. The overall intensity sum is then the incoherent addition of the coherent combination of each pair of like-frequency fields:

$$I_{SUM} = [E_{A1}^2 + E_{B1}^2 + 2E_{A1}E_{B1}\cos\phi_1] + [E_{A2}^2 + E_{B2}^2 + 2E_{A2}E_{B2}\cos\phi_2] \quad (2.36)$$

Figures 2.9(a)-(d) show the solutions for both values of ψ during simultaneous displacement of both output mirrors. Because the general character of the two-mode tuning curves is similar to those from the single-mode case, only the

salient features will be discussed in detail. The top curve of Figure 2.9(a) is the intensity sum (scaled by one-half) discussed in the preceding paragraph, and the two lower curves trace the intensities of the like-frequency mode pairs. This unique intensity profile is identical in shape whether two coupled lasers or a single laser is allowed to oscillate on two longitudinal modes. Figure 2.10 is an output intensity curve of a single two-mode laser oscillating under the same conditions as the coupled laser case. To understand the profile, some of the aspects of Doppler-broadened laser media and spectral hole burning must be considered. As the modes are tuned across the gain curve and the first mode reaches the gain center, it burns out a Lamb dip decreasing the output intensity (Figure 2.10(b)). When the modes are symmetrically spaced about the line center frequency, the spectral holes burned into the medium by the two modes overlap and mutually reinforce each other by burning holes at exactly the same points on each side of the gain center. This mutual overlap causes a larger decrease in the output intensity than the decrease caused by a single mode (Figure 2.10(c)). Continued mirror translation draws the remaining mode across the gain center which burns a second Lamb dip (Figure 2.10(d)). In fact, this type of hole-burning phenomenon occurs in all Doppler-broadened multimode lasers. The existence of the mutual hole burning minimum was experimentally verified with a single He-Ne laser oscillating on two modes²⁸. Even though the He-Ne experiment investigated the hole burning phenomenon with a single (uncoupled) two-mode laser, the observation of the mutually-reinforced hole-burning minimum substantiates the interpretation of the theoretical curve and provides some experimental support for the validity of this two-mode laser theory. (See Appendix B for the details of the experiment.)

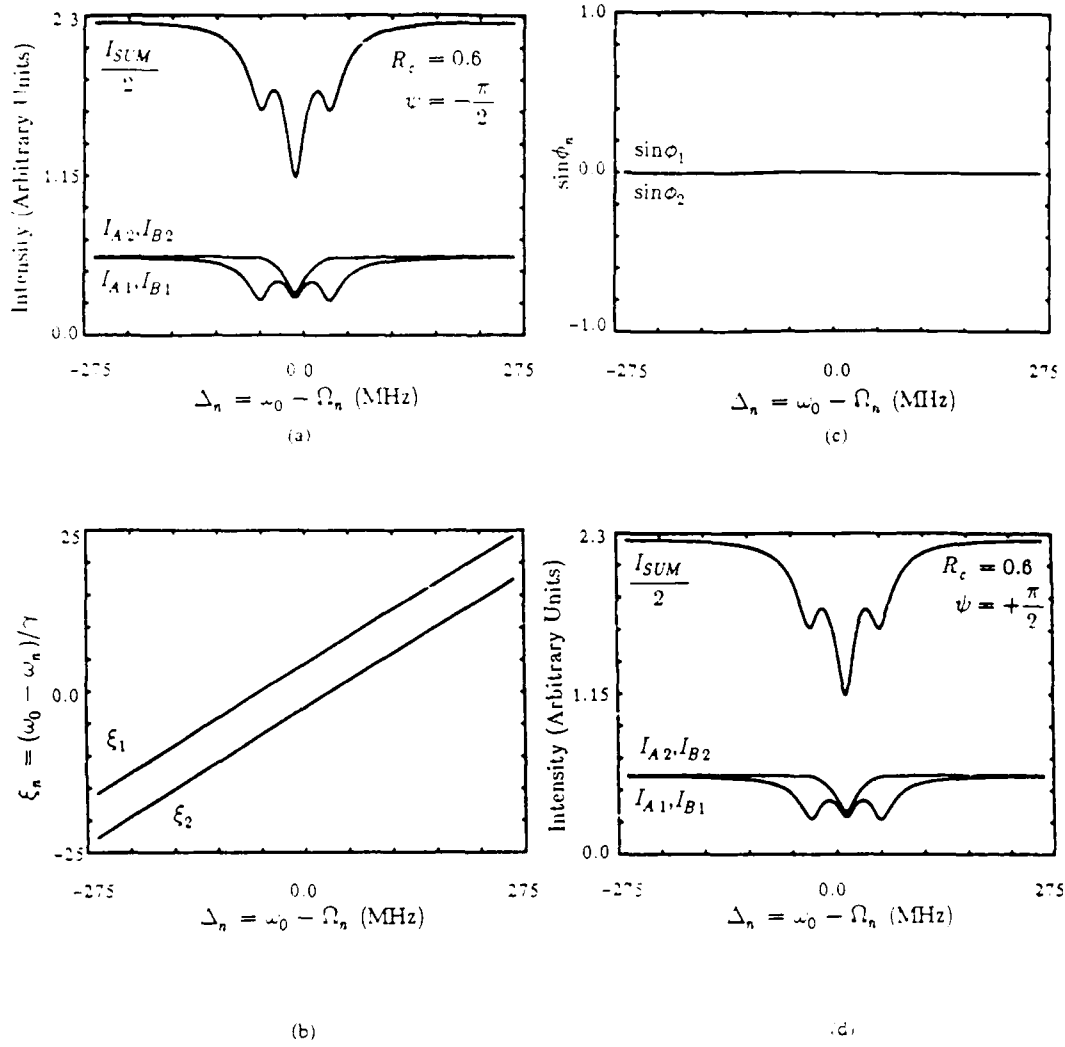


Figure 2.9: Intensity, frequency detuning, and phase as a function of cavity detuning for two-mode coupling for the case of translating both output mirrors simultaneously (a)-(c) $\psi = -\pi/2$, (d) $\psi = +\pi/2$. The solutions are stable for all displacements.

The transmitted waves of the coupled resonators encounter a phase shift as they transit the coupling mirror. This phase shift changes the effective length of

the resonators thereby displacing the actual cavity frequencies from the expected cavity frequencies. For the $\psi = -\pi/2$ phase difference used in Spencer and Lamb's theory¹², the modes are moved approximately 12 MHz higher in frequency (Figure 2.9(a)), but if the phase difference is $\pi/2$, then the laser modes are shifted roughly 11 MHz lower than the unperturbed cavity frequency (Figure 2.9(d)). If the phase difference can be manipulated such that $\psi = 0$, then not only are the solutions stable for all displacements, but the output intensities reach their maxima as well. This result is encouraging, but $\psi = 0$ does not satisfy conservation of energy when applied to the mirror model used in this analysis (*i.e.* $\phi_r = \pi$).

The behavior displayed in the remaining tuning curves is remarkably similar to those for the single-mode case. In the case of translating a single output mirror (Figures 2.11(a)-(c)), the maximum intensity sum does not occur at zero displacement because of the asymmetries of the individual intensities. The asymmetric tuning is also borne out by the appearance of the intensity and frequency curves. When translating the coupling mirror while maintaining a constant total resonator length (Figures 2.12(a)-(c)), the intensity sum in this instance reaches a maximum at zero detuning, and the curves are completely symmetric about this point. As in the case of the single-mode lasers, the desired operating point of a two-mode coupled laser system for maximum output intensity is when the two coupled cavities are equal in length but tuned such that the frequency of one mode is farther than at least one free spectral range from the gain center.

Perhaps the most notable comparison between the single- and two-mode theories is that the two-mode locking ranges are almost exactly one half of the

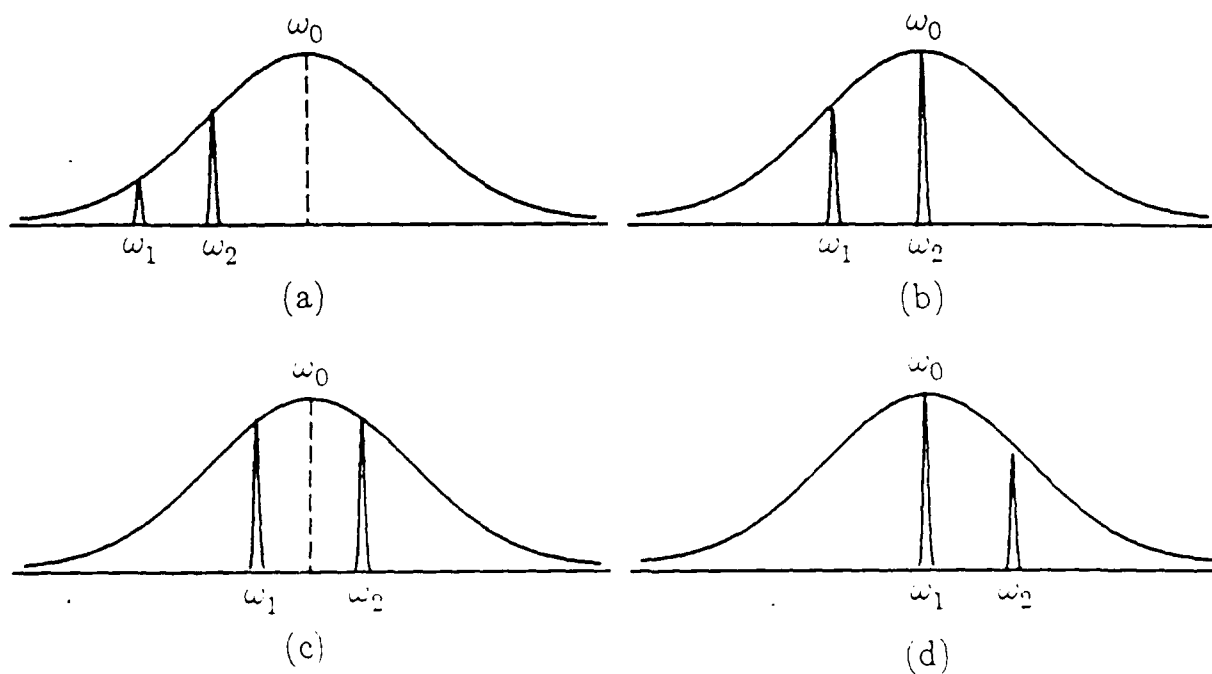
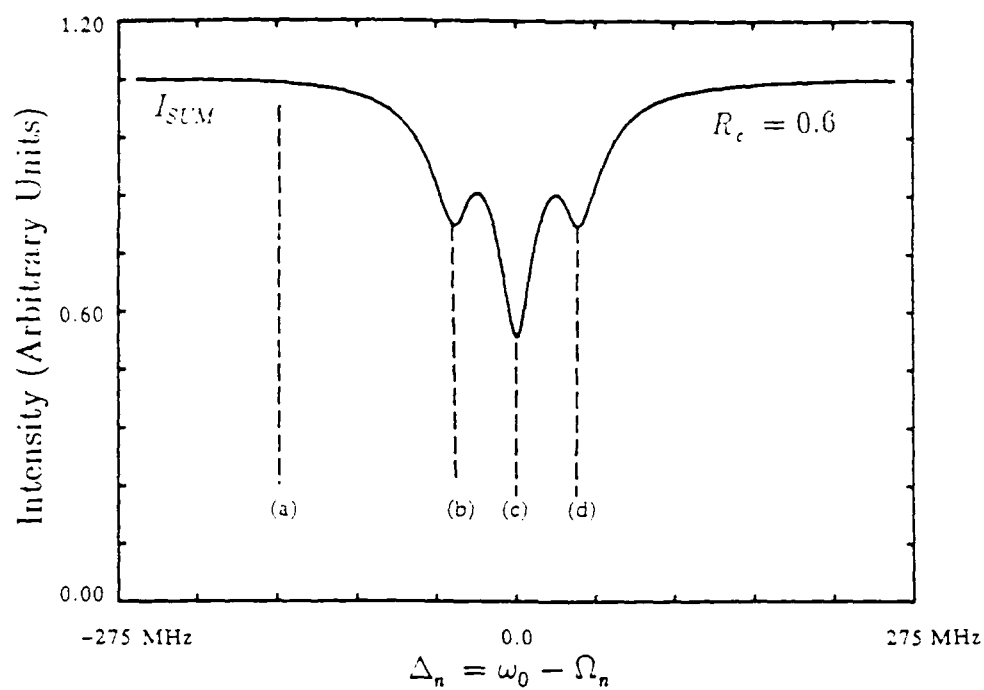


Figure 2.10: Mode structure of intensity verses cavity detuning for a single, uncoupled laser. See text for complete explanation.

single-mode locking ranges. The presence of the additional mode significantly affects the coupled laser stability (Lower curve of Figure 2.8). In the absence of any hard experimental evidence at the present time to support the predicted decrease in locking range from coupled single-mode lasers to coupled two-mode lasers and without additional information for other multimode systems, it is difficult to be absolutely certain that this locking range reduction should occur. In an analogous situation, Anderson, Chow, and Scully observed a decrease in the lockband of ring-laser gyros oscillating on two strong longitudinal modes and two weak transverse modes over ring-laser gyros oscillating on only two modes ²⁹. Although ring-laser gyros are different from coupled lasers in many respects, the interaction of the forward and reverse waves, in a sense, form coupled waves which should obey the same medium physics whether in gyros or coupled standing-wave cavities. Nevertheless, the difference in the two locking ranges is understandable because not only is there cross communication between adjacent longitudinal modes in each cavity, but the additional influence of the adjacent longitudinal modes of the coupled resonator causes further perturbation to the system.

Since there has been no analysis of systems with more than two modes, generalization of the reduction in locking range would be highly speculative. Further decrease in the locking range is expected with the addition of more modes, but because the interaction of the new mode with the non-adjacent mode is weaker than for adjacent modes, the incremental reduction in locking range should be smaller than the factor of one-half seen in going from one to two modes.

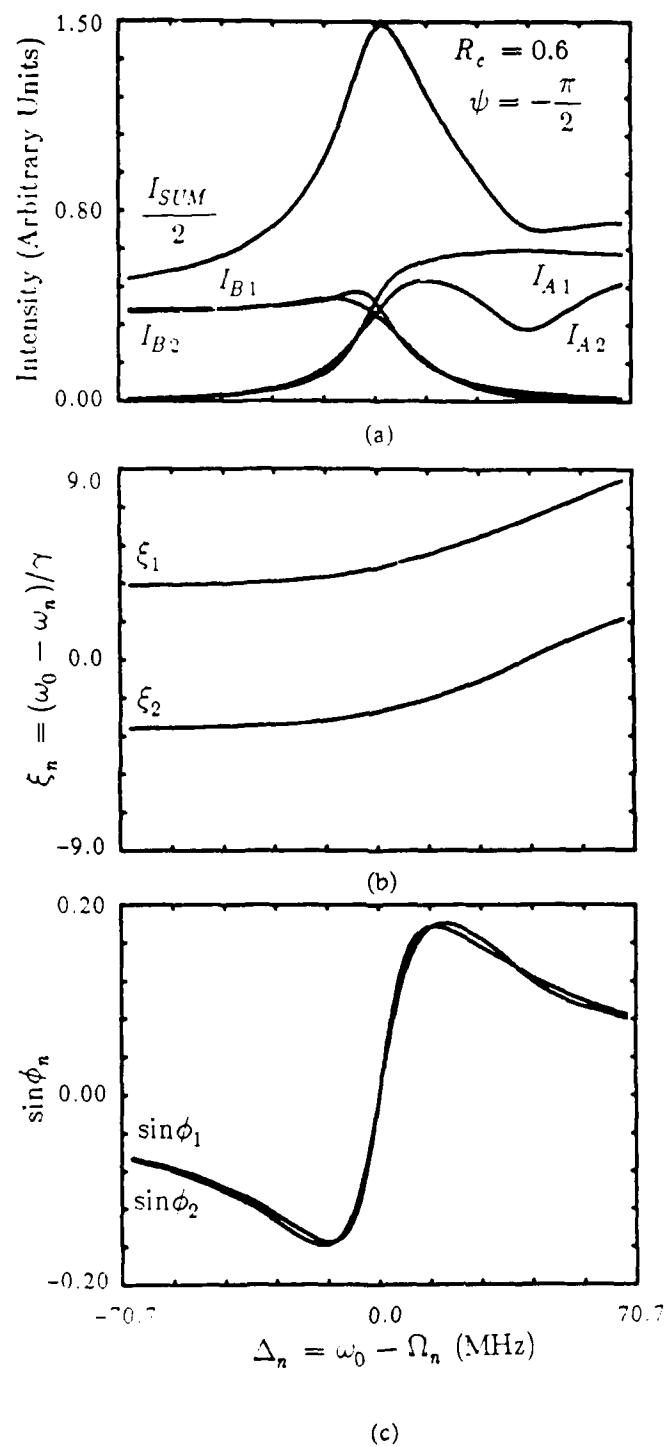


Figure 2.11: Intensity, frequency detuning, and phase as a function of cavity detuning for two-mode coupling for the case of translating a single output mirror. The solutions are stable from -6.41 MHz to +6.43 MHz.

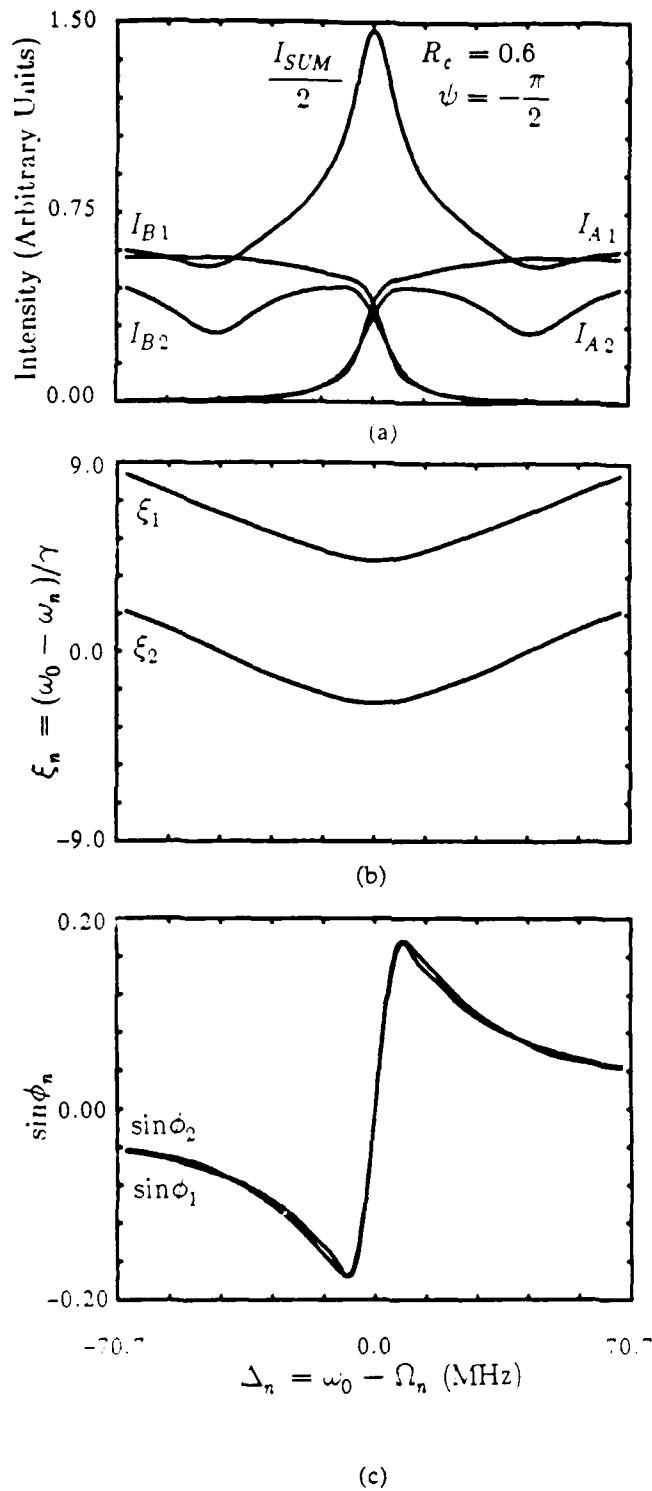


Figure 2.12: Intensity, frequency detuning, and phase as a function of cavity detuning for two-mode coupling for the case of translating the coupling mirror. The solutions are stable for -2.94 MHz to +3.26 MHz.

D. Conclusion

Existing coupled laser theories have been extended to analyze the case of two coupled lasers supporting two modes in each cavity. A number of oddities in behavior have been found to exist including a mutually-reinforced hole-burning minimum and a shift of the laser frequencies from the bare cavity frequencies. Locking ranges were computed for both the single- and two-mode coupled laser systems, and it was found that the presence of an additional mode reduces the locking range. The possible utility of coupled laser systems makes theoretical analysis necessary, but further development of Lamb's electromagnetic treatment may prove too tedious to apply to multimode/multiwavelength lasers. A new approach developed by Rinaldi and Erkilli¹⁹ which treats the coupling as an injection process may be the preferred method to completely model a real coupled laser system.

Chapter III. Coupled Ar-ion Lasers Experiment

This chapter will describe the experiment performed to phase lock two Ar-ion lasers using conventional resonator coupling. In the first section, the experimental configurations used to couple the lasers will be explained along with descriptions of some of the primary operating characteristics. The second section will detail the measurements made and the purpose of those measurements in diagnosing the phase-locked performance.

A. Experimental Configurations

The basic experimental configuration was based on the coupled laser system examined theoretically by Spencer and Lamb ¹² (*i.e.* two lasers coupled through a common end mirror). Unlike the idealized initial conditions conceived by Spencer and Lamb in which the lasers oscillate on a single mode in cavities of exactly equal length and identical gain media, the Ar-ion lasers were initially allowed to operate in multiline and multimode on as many wavelengths and modes as possible (the final experiment was on single wavelength) in order to increase the probability of phase locking. Phase locking can only occur between two modes of exactly the same frequency, so the chances of overlapping one or several of the hundreds of modes oscillating is greatly enhanced when air turbulence, vibrations, and thermal expansion and contraction tune the lasers. The Spencer and Lamb theory couples two single-mode lasers with homogeneously-broadened media, but more importantly, it assumes *a priori* that the lasers are phase locked. This is

certainly not a valid, realistic assumption. In fact, little is known about what mechanism may actually induce phase locking, and at least in the case of Ar-ion lasers, the coupling process is dynamic and the coupled system is poorly behaved in terms of frequency jitter and fringe stability.

Active stabilization is needed to tune and maintain the lasers at exactly the same frequency in order to allow single-mode lasers to phase lock. Not only was active stabilization not a desired requirement of this investigation, but it would have been extremely difficult to implement with such long, open cavities even if the equipment had been available. In addition to the problem of stabilization, no unambiguous diagnostics would have been possible because the single-mode coherence length is so long that the visibilities of the interference fringes measured in a preliminary experiment were uniformly high and exclusively due to self interference. Also, no radio frequency mode beat exists for single-mode lasers, so there could be no independent verification of phase locking.

Two nominally identical Spectra-Physics Model 165 Ar-ion lasers were configured in a U-shaped cavity with 90% reflective output couplers and coupled together through a common end mirror which also served as the coupling mirror for the lasers (See Figures 3.1, 3.2, and 3.3). Figure 3.2 also depicts the diagnostic equipment used to make the measurements for the various experiments. The two output beams were superposed in the near field by constructing an interferometer and matching the optical paths to within the coherence length of Ar-ion (about 3 cm). Two different experiments were performed, one to study multiline/ multimode coupling, and the other to study single-line coupling. In the first experi-

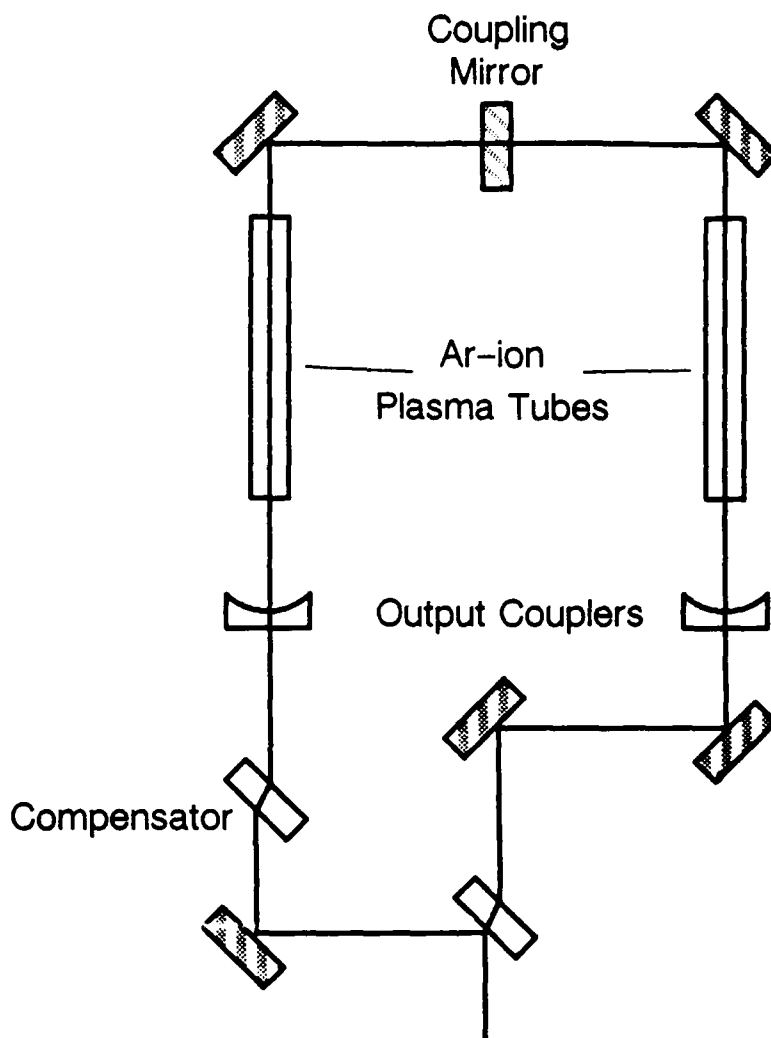


Figure 3.1: Schematic diagram for multiline coupling without an optical trombone for path length compensation.

ment (Figure 3.1 and 3.2), the lasers were operated in multiline and multimode and an optical trombone with submicron resolution was incorporated into one side of the coupling paths which were equalized to within a millimeter. The results without the optical trombone were essentially a benchmark for comparison for the more carefully controlled experiments. In the second experiment (Figure 3.3), single-line operation at 488.0 nm was studied by placing dispersing prisms in the cavities and realigning the output couplers while using the same coupling

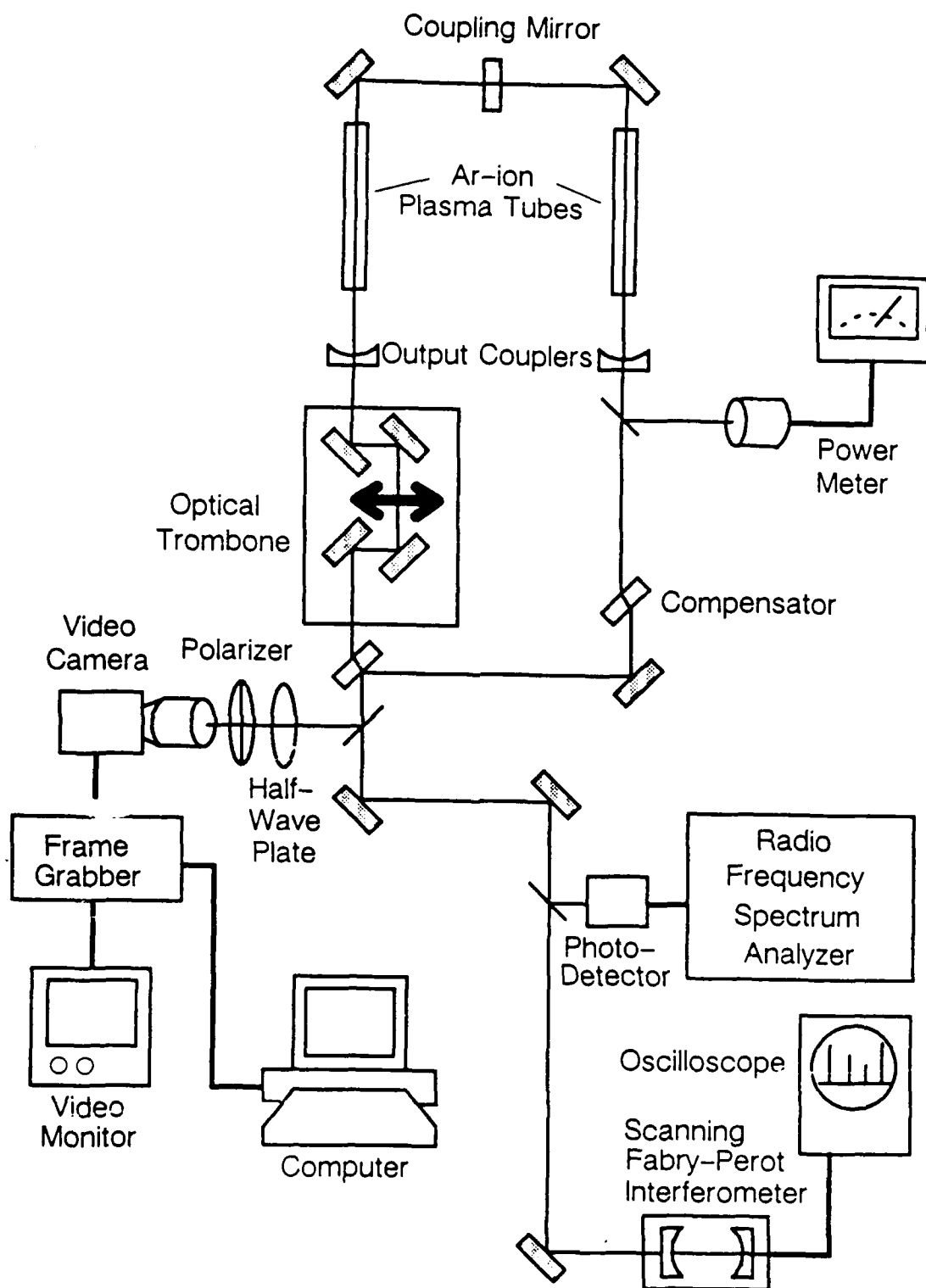


Figure 3.2: Schematic diagram for multiline coupling with an optical trombone for path length compensation and the diagnostic equipment used for the measurements.

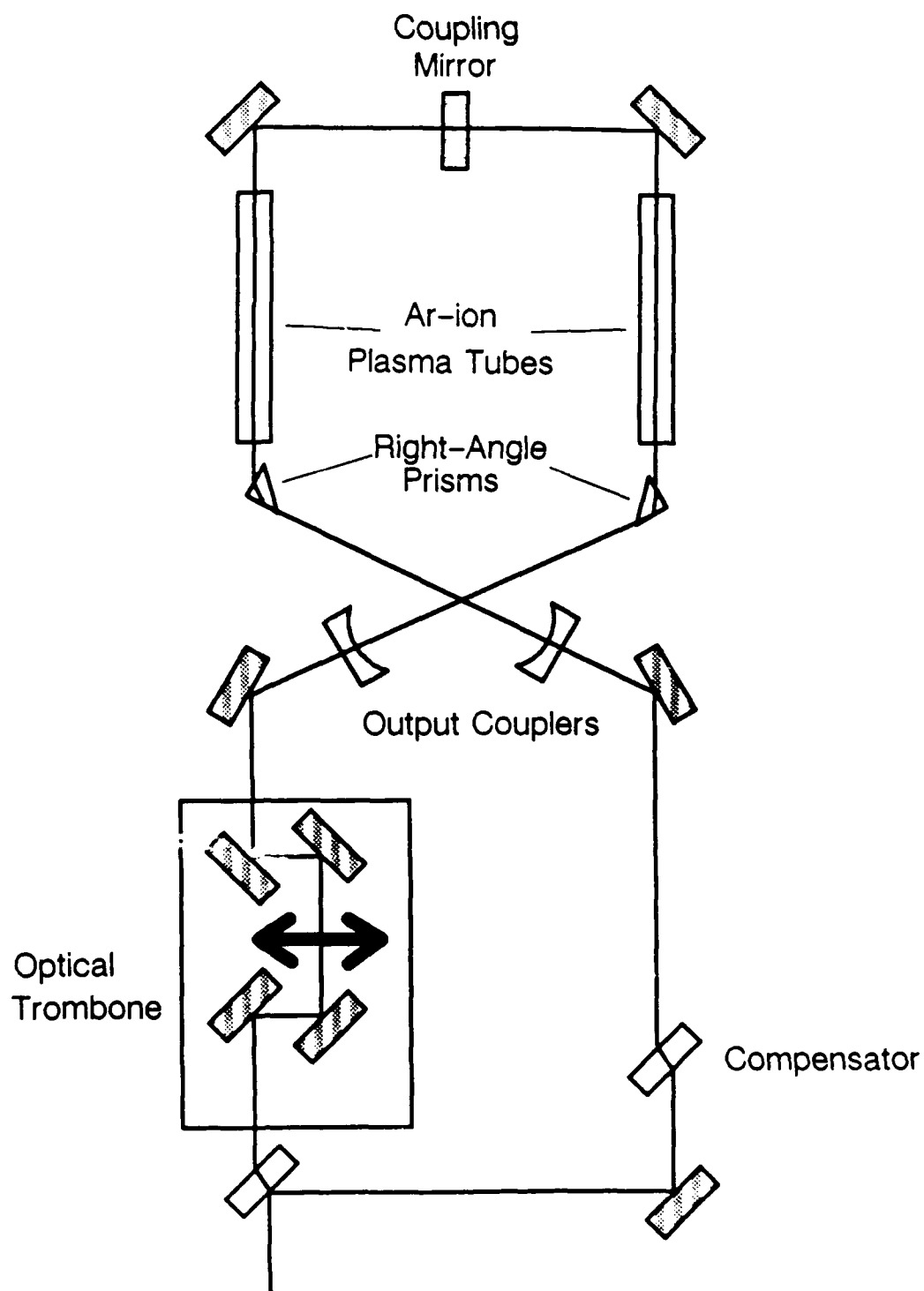


Figure 3.3: Schematic diagram for single wavelength coupling with an optical trombone for path length compensation.

configurations.

The total optical cavity length of the coupled system was 348.6 ± 0.4 cm with each sub resonator half of that optical length. Without the coupling mirror in the cavity, the transmitted power from each output coupler was 1.0 W on four multimode wavelengths (514.5 nm, 496.5 nm, 488.0 nm, and 476.5 nm). The Brewster windows of the laser plasma tubes force the lasers to emit vertically polarized light. For the single wavelength experiment at 488.0 nm, the dispersing prisms could only be oriented horizontally which meant the vertically polarized light incident on the prism faces would be strongly reflected and not transmitted as desired. Fortunately, the system gain was sufficiently high to overcome the losses induced by the reflections of the polarized cavity beam and still generate 500 mW of output intensity.

When multiple wavelengths interfere at some point in space, the fringe envelope of the composite pattern is governed by the equation

$$\frac{I_{coherent}}{I_{total}} = \sum_{i=1}^n P_{\lambda_i} \cos \left(\frac{4\pi\Delta L}{\lambda_i} \right) \quad (3.1)$$

where P_{λ_i} is the power fraction of each wavelength and ΔL is the path length detuning in microns. To determine which wavelengths were lasing and the intensity of each, the output beam was dispersed into four separate beams using a Pellin-Broca prism. The intensities were then measured by placing a power meter behind an adjustable iris to block all but one wavelength. The output intensities of each wavelength are shown in Table 3.1. With these values, the equation of the multiline fringe envelope is given by

$$\frac{I_c}{I_t} = 0.186 \cos(24.42\Delta L) + 0.064 \cos(25.31\Delta L) \quad (3.2)$$

$$+ 0.636 \cos(25.75\Delta L) + 0.114 \cos(26.37\Delta L)$$

where ΔL is in μm units, The equation is graphed in Figure 3.4 which shows the the theoretical multiline fringe envelope produced from the interference of two beams of equal intensity consisting of the four Ar-ion laser wavelengths as the coupling paths are detuned from each other.

Table 3.1: Ar-ion Wavelengths and Intensities	
Wavelength (nm)	Power (mW)
476.5	46.0
488.0	257.0
496.5	26.0
514.5	75.0

Even though the maximum multiline fringe visibility only occurs when there is zero path length difference between the two legs of the interferometer, the calculation shows the condition is not as stringent for interference of the four Ar-ion wavelengths listed previously. The figure shows most of the local maxima are roughly the same magnitude. When fluctuations of the fringes are taken into account, it is evident that the maximum practical fringe visibility could be obtained as long as the detuning remained within the peak region of one of the large envelopes. The low visibility regions were easily identified by scanning the optical trombone and watching the envelopes with a PIN diode connected to an

oscilloscope. Once the coupling path lengths were within a few millimeters of each other, the trombone was set at one of the local maxima close to the zero optical path difference and periodically readjusted as the path changed with thermal expansions and contractions.

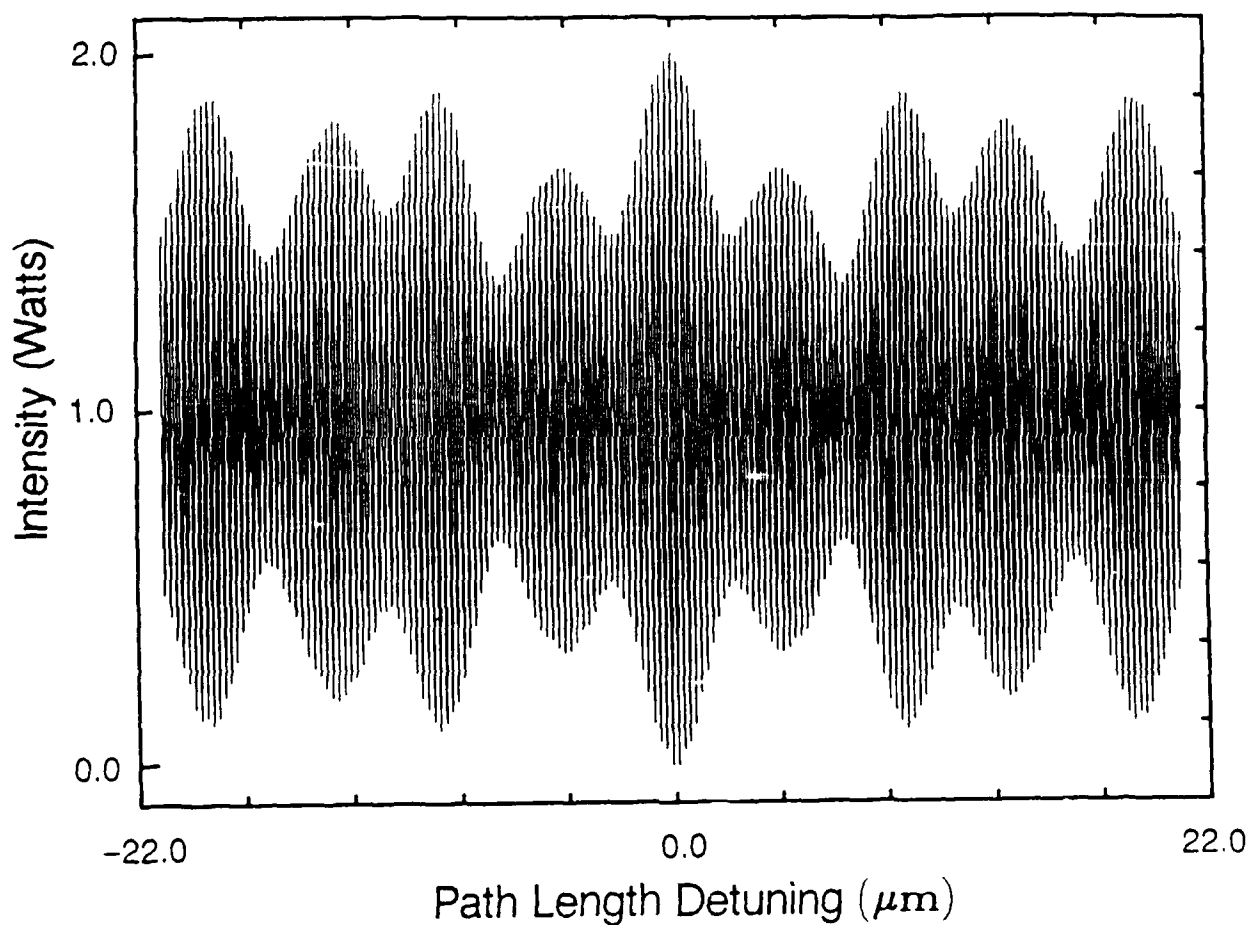


Figure 3.4: Multiline fringe envelope generated from the near-field interference of the four Ar-ion laser wavelengths described in the text as the optical trombone is scanned.

B. Measurements

To investigate the effect of coupling strength on the phase-locked behavior, eight different coupling mirrors ranging in reflectivity from 10% to 90% were inserted into the cavity. The mirrors were all of slightly different thicknesses, so it was impossible to control the exact cavity lengths to within the resolution of the ruler used to measure the cavity length. The thickness differences were on the order of 0.002 inches which is quite large on the optical scale but imperceptible in length measurements of 3.5 m. No measurements could be made with the 40% reflective mirror because the substrate wedge was so severe that balanced lasing could not be achieved between the two cavities. After each coupling mirror was placed in the cavity and aligned, the output couplers were then realigned to produce the maximum power output and the maximum activity of the frequency spectrum.

Phase locking means that the lasers are mutually coherent, and the principal diagnostic used to identify phase locking was the appearance of stable interference fringes. The fringe visibilities were measured by capturing a fringe pattern with a CID (charge-injected diode) camera and frame grabber and calculating the visibility according to equation (1.10). Since the fringe patterns fluctuated on a macroscopic time scale, 10 to 40 visibilities were averaged for each measurement. Single-line visibilities at 488.0 nm and 514.5 nm as well as the total multiline visibility were measured. The single-line visibilities during multiline operation were isolated with 100 Å narrow-bandpass interference filters placed in the interferometer immediately in front of the CID camera.

The lasers operated in a long open cavity and were combined along a sizeable coupling path so the beams were subject to a significant amount of air turbulence and mechanical vibrations which caused the fringes to fluctuate. One of the primary disturbances was the vibration caused by the water flowing through the cooling jackets of the laser plasma tubes. The visibility of each pattern changed continually so only the best fringes were captured for each mirror. Although somewhat subjective, this procedure gave solid statistics and reproduceable results.

Because fringes can also arise from reflections not related to phase locking (for example, interference is produced even with one laser turned off due to photons leaving the coupling mirror simultaneously), other diagnostics were needed to definitely determine the origin of the interference whether they resulted from phase locking or self interference. Detectors were slid into the beam to make a measurement or part of the beam was redirected into them with beamsplitters. In multimode lasers, each pair of adjacent modes beat with each other to generate a radio frequency signal which indicates the spacing between the modes. In his theoretical paper on coupled lasers, Chow found that coupled lasers oscillate at frequencies whose mode spacings are determined by the total length of the supercavity called "supermodes"²⁶. The presence of a radio frequency (RF) mode beat whose frequency is at the mode spacing of the entire resonator turned out to be the strongest corroborative evidence of phase locking since its presence meant that the two subcavities were operating as parts of one supercavity. In the limit of a single 3.5 m-long laser, the mode beat spectrum will display a peak at 43 MHz corresponding to the free spectral range of the supercavity. With coupling mirrors inserted into the laser, the appearance of supercavity mode beat,

particularly at low coupling powers, will indicate the two sub-cavities are phase locked with each other. Each mode also beats with the other modes and these signals show up as evenly spaced overtones in the mode beat spectrum. If any transverse modes are oscillating in the laser, these will also create mode beats, but the signals will be at odd frequencies and serve to broaden the spikes in the longitudinal mode beat spectrum.

In addition to the RF mode beat spectrum, the output intensities were measured with a power meter to track notable changes in output power and to determine which combination of mirrors generated the maximum output power. The information was also needed to balance the intensities of the coupling beams which were combined to form the fringes because the best visibilities are achieved when the intensities of the two beams are equal. The optical frequency spectrum was monitored using a scanning Fabry-Perot interferometer. The frequency spectrum proved to be a valuable tool in optimizing the laser cavity alignment and in understanding the mode selection of the coupled laser system by giving a visual representation of the frequency-locking process.

Chapter IV. Results and Analysis

This chapter will present the experimental results and an analysis of the behavior of the coupled laser system. The first section will describe the performance of the lasers in terms of the frequency and mode beat spectra, the power output, and the interference fringe patterns. In the second section, the data is tabulated and plotted and those plots are interpreted.

A. Data

i. General Descriptions

Not surprisingly, all three experimental configurations (the two multiline experiments with and without the optical trombone and the single line experiment) exhibited the same general behavior, so the descriptions which follow are applicable to all except where specifically stated. Without the coupling mirror, the multimode frequency spectrum which spans more or less uniformly over 6 GHz was broader than the free spectral range of the interferometer (1.5 GHz) and resulted in an an equal intensity "grass" (See Figure 4.1(a)). With any coupling mirror, a discrete number of modes were selectively reinforced and increased in intensity by about 3 to 5 times that of the other modes (Figure 4.1(b)). This mode spiking was a strong indication that the mirror alignments were good and that phase locking might occur. The frequency spikes were neither fixed nor steady but varied in intensity and jittered freely probably due to air turbulence, mechanical vibrations, and/or mode competition. Generally, the intensity of the

spikes was different among the different coupling mirrors with the spikes for the 90-70% transmission much less intense than those for the 50-10% coupling.

Both the output power and the mode beat spectra paralleled the behavior of the frequency spectrum. Rising from 1.2 W multiline output from each output coupler at 10% reflectivity, the output power reached a maximum of 1.85 W at 70% coupling mirror reflectivity before tapering off to 1.65 W at 90%. The power outputs measured for each of the coupling mirrors are compiled in Table 4.1.

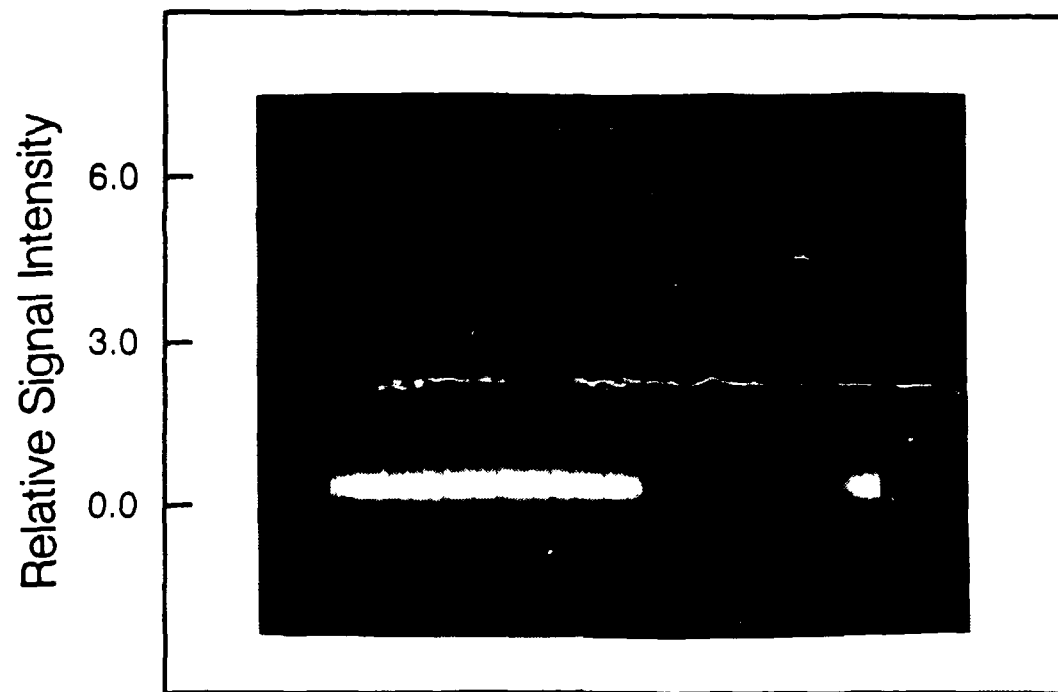
This intensity increase occurs because the higher reflectivity mirrors increased the saturation in each of the gain tubes and extracted more energy from the active media. The power output tapered off at 90% reflectivity as the out-coupled power fraction decreased faster than the cavity's internal power density increased. Even though the cavities were made as symmetric as possible, the intensity from both output couplers were close but not equal. This may be due in part to unequal gain in each tube, but it may also result from an intensity imbalance inherent in three mirror cavities. There will be a further discussion on this imbalance later in the chapter.

The intensity of the RF mode beat at 43 MHz (the composite resonator mode spacing) was also higher for the higher reflectivity coupling mirrors, and the signal was broad indicating both longitudinal and transverse modes were coupling. As the coupling strength was increased, the mode beat signal narrowed and eventually became a single spike. The importance of the interpretation of the RF mode beat spectra will be discussed in greater detail in conjunction with the analysis of the fringe patterns. The significance of these measurements and observations will

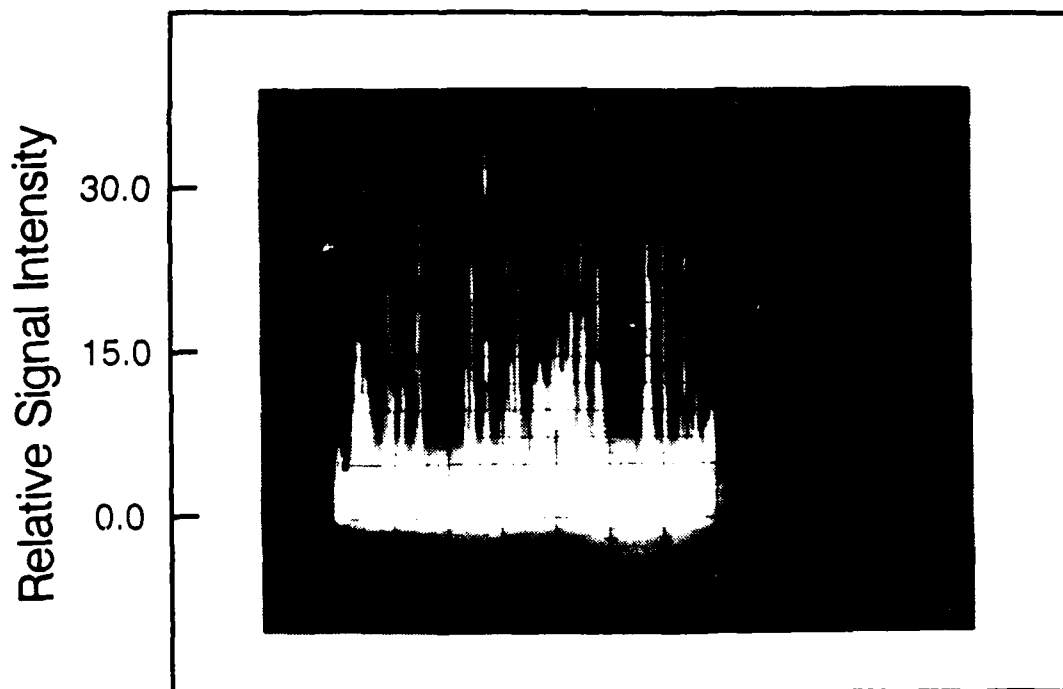
be more easily understood when viewed with the evolution of the visibility of the interference fringes.

ii. Interference Fringes

Interference fringes were present with every coupling mirror, but all were not produced as a result of phase locking. As stated in the previous chapter, the fringes jittered, wiggled, and danced in concert with the frequency spectrum. Fortunately, the sampling rate of the frame grabber was fast enough to capture usable patterns. The unstable activity varied among the different coupling mirrors. Some of the isolated wavelengths were more stable than others, and the stability varied from mirror to mirror following no discernable trend. Figures 4.2, 4.3, and 4.4 are samples of interference fringe pattern profiles from the three experiments. The fringes in Figure 4.2 were produced without benefit of the optical trombone. Figure 4.3 is the multiline coupling with the trombone, and Figure 4.4 shows the fringes from the single-line case also with the trombone incorporated into the coupling path. In Tables 4.2, 4.3, and 4.4, the number of samples, average visibilities, and standard deviations are recorded for the three experiments. Notice the sample standard deviations decrease in the second and third experiments. Not only does this result from more closely matched coupling paths but also from a refinement in measurement techniques as the experiment progressed.



(a)



Frequency

(b)

Figure 4.1: Multimode frequency spectrum showing (a) the equal intensity grass with no coupling mirror, and (b) the mode spiking with a 70% reflective coupling mirror.

Table 4.1: Output Power for each Coupling Mirror	
Coupling Mirror Reflectivity (%)	Power (W)
0	1.00
10	1.20
20	1.25
30	1.40
50	1.75
60	1.80
70	1.85
80	1.35
90	1.65

B. Analysis

The behavioral trends surface when the visibilities are plotted as a function of the coupling mirror transmission (See Figures 4.5, 4.6, and 4.7). Figures 4.5 and 4.7 are the plots of the visibilities for the multiline coupling experiments, the latter without the optical trombone, and Figure 4.6 is the single-line experiment at 488.0 nm. For comparison, the multiline experiment was repeated without the optical trombone but with the coupling paths adjusted to within 0.5 ± 0.4 cm. Equalizing the path lengths with the trombone increased the visibilities in most cases by about one-third. The results (plotted in Figure 4.7) show a degradation in the visibilities compared to those in Figure 4.5 which is consistent with coherence considerations. The data points were fitted with a cubic spline interpolation in order to enhance the salient features. Note that several of the points at 20% coupling (80% reflectivity) fall below the curve except for the visibilities at 514.5 nm. For this same mirror, the output intensity also showed a substantial drop below the trend exhibited with the other mirrors. The transmission of each

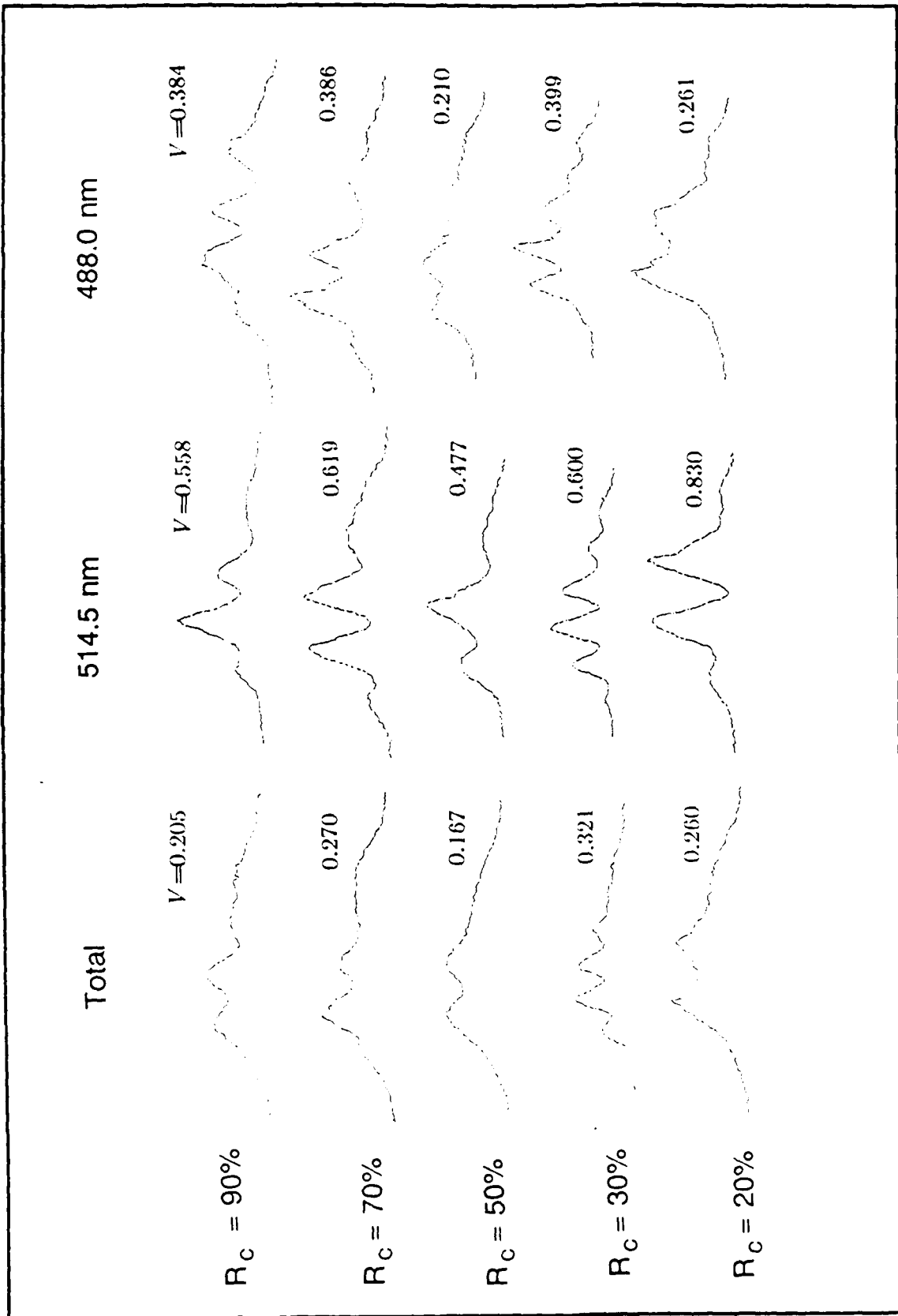


Figure 4.2: Sample near-field interference fringes from multiline coupling without the optical trombone. R_c = Coupling Mirror Reflectivity, V = Visibility.

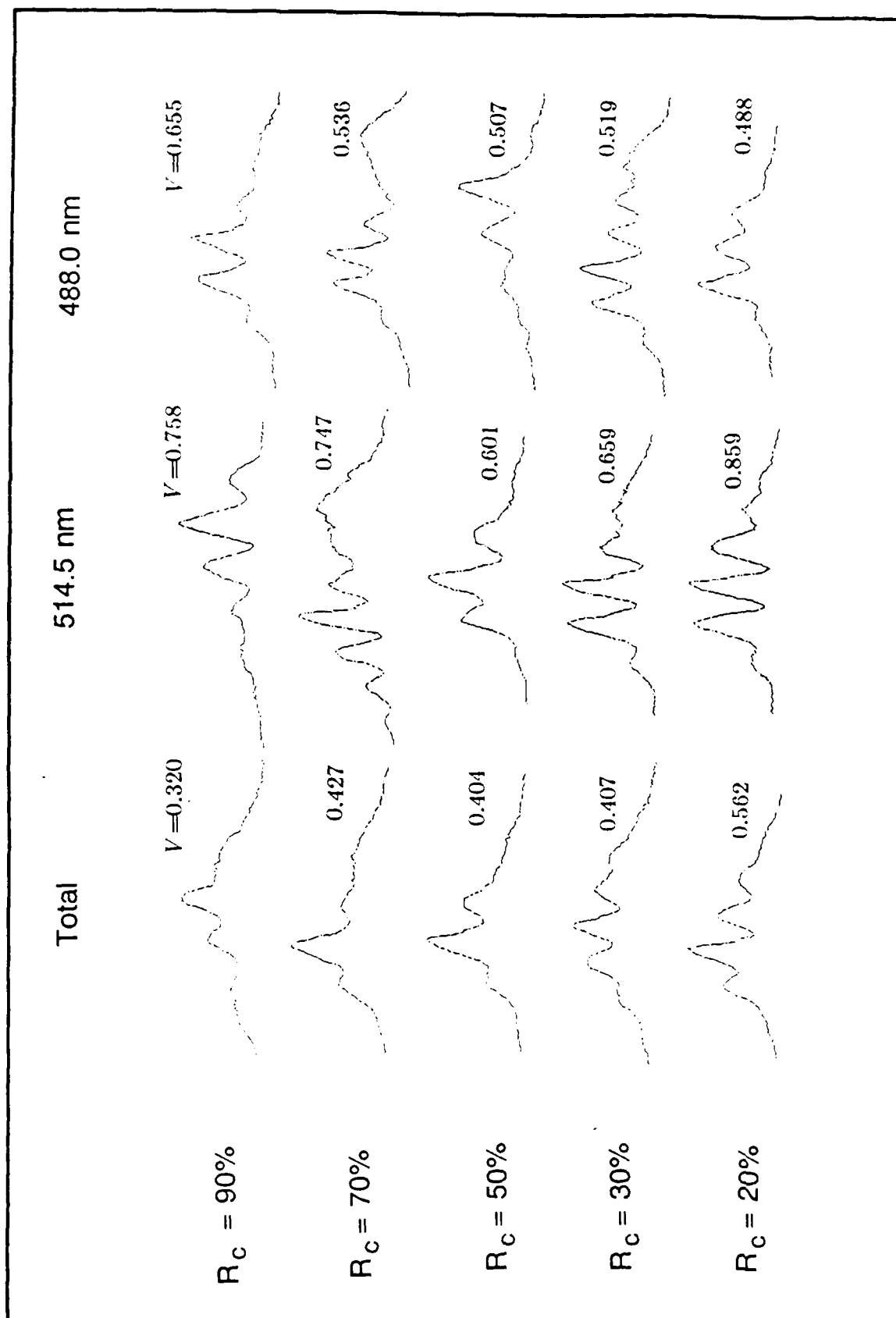


Figure 4.3: Sample near-field interference fringes from multiline coupling with the optical trombone. R_c = Coupling Mirror Reflectivity, V = Visibility.

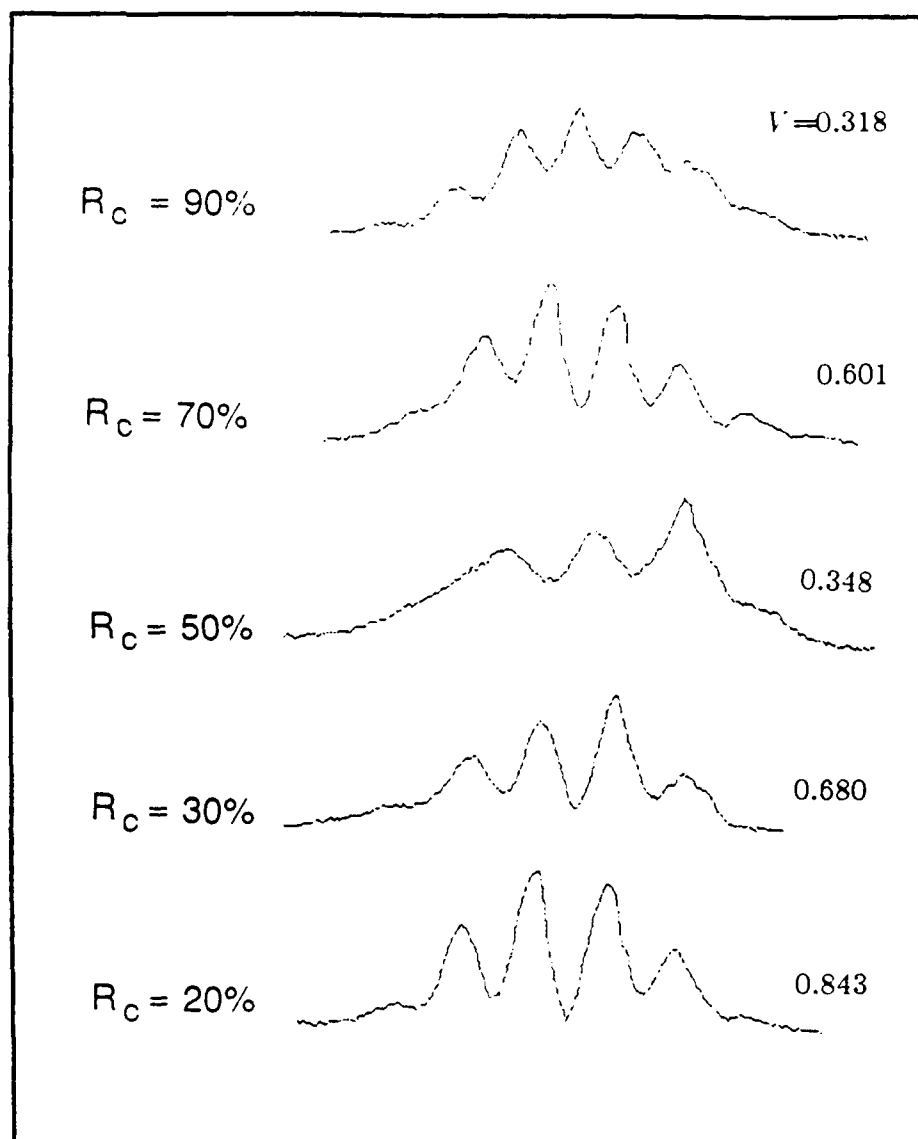


Figure 4.4: Sample near-field interference fringes from single line coupling at 488.0nm. R_c = Coupling Mirror Reflectivity, V = Visibility.

mirror was measured with a spectrophotometer, and the actual transmissivities varied from the manufacturers specifications by as much as 7%. The 80% mirror was approximately 17.5% transmissive (which is good, relatively speaking) so I am at a loss to explain the anomaly in the fringe visibilities. Since the actual transmissivities were available, the fringe visibilities were plotted as a function of

the true values of the coupling mirror transmission. Table 4.5 shows the measured transmissivities for 514.5 nm and 488.0 nm along with the estimated overall transmissivity compared to the manufacturers specifications.

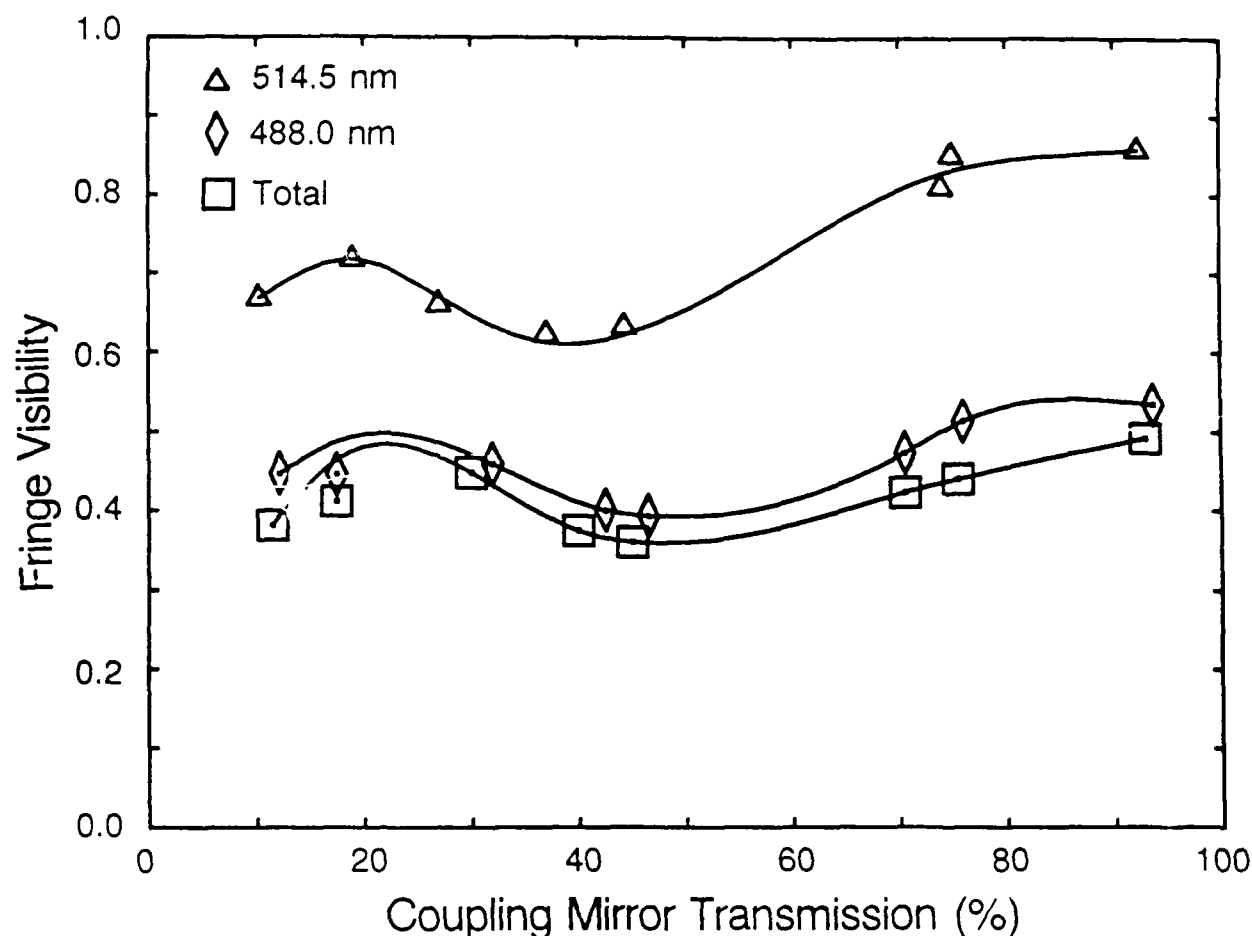


Figure 4.5: Fringe visibilities plotted as a function of coupling mirror transmission for two coupled multiline lasers with the optical trombone in the coupling path.

Before undertaking the experiment, it was expected that the fringe visibilities would be poor or non-existent for the low coupling powers, and then increase more or less monotonically as the coupling strength increased, since at 100% coupling (no coupling mirror) the two lasers are totally coherent with each other

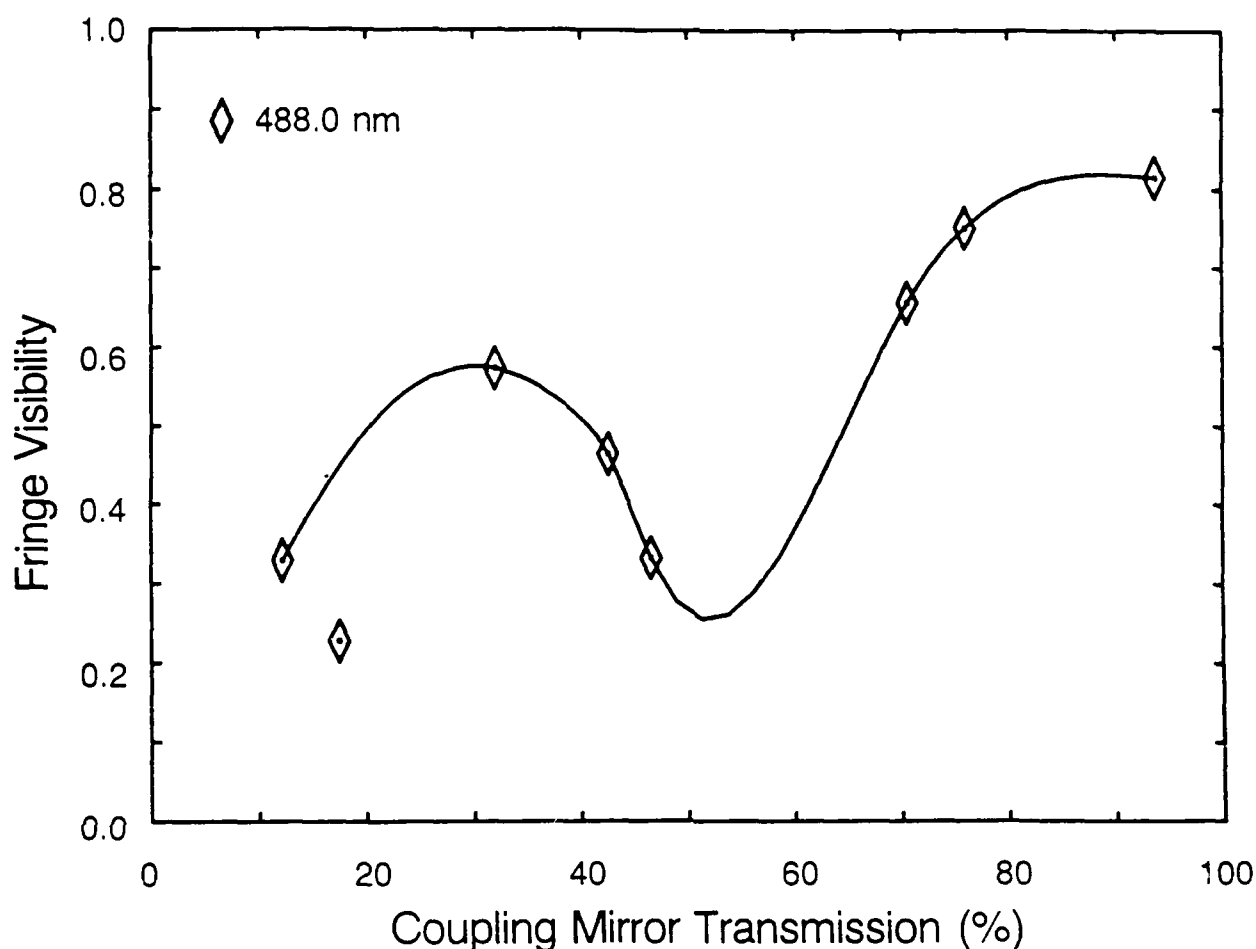


Figure 4.6: Fringe visibilities plotted as a function of coupling mirror transmission for two coupled single-line lasers oscillating at 488.0 nm with the optical trombone in the coupling path.

because they are in fact a single laser. In addition, it was also thought that the RF mode beat at the super cavity resonance would grow from a negligible level at high coupling mirror reflectivities and increase in strength as the mirror reflectivities were gradually lowered to smaller values and the two coupled lasers became closer to a single laser cavity. This was not observed in the experiment. Odd though the actual results appear to be, they are understable when interpreted in conjunction with information provided by the RF mode beat spectrum and

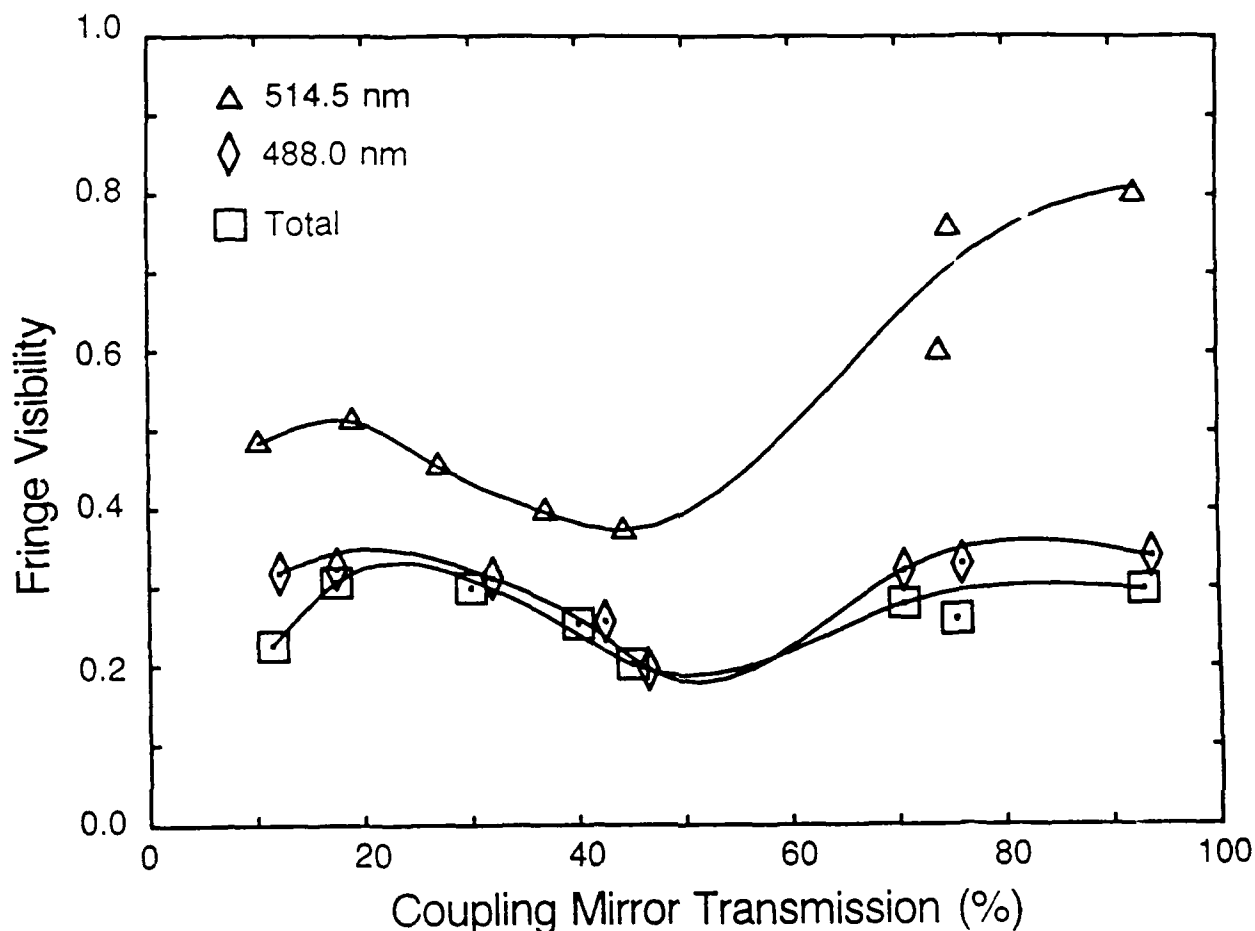


Figure 4.7: Fringe visibilities plotted as a function of coupling mirror transmission for two coupled multiline lasers without the optical trombone in the coupling path.

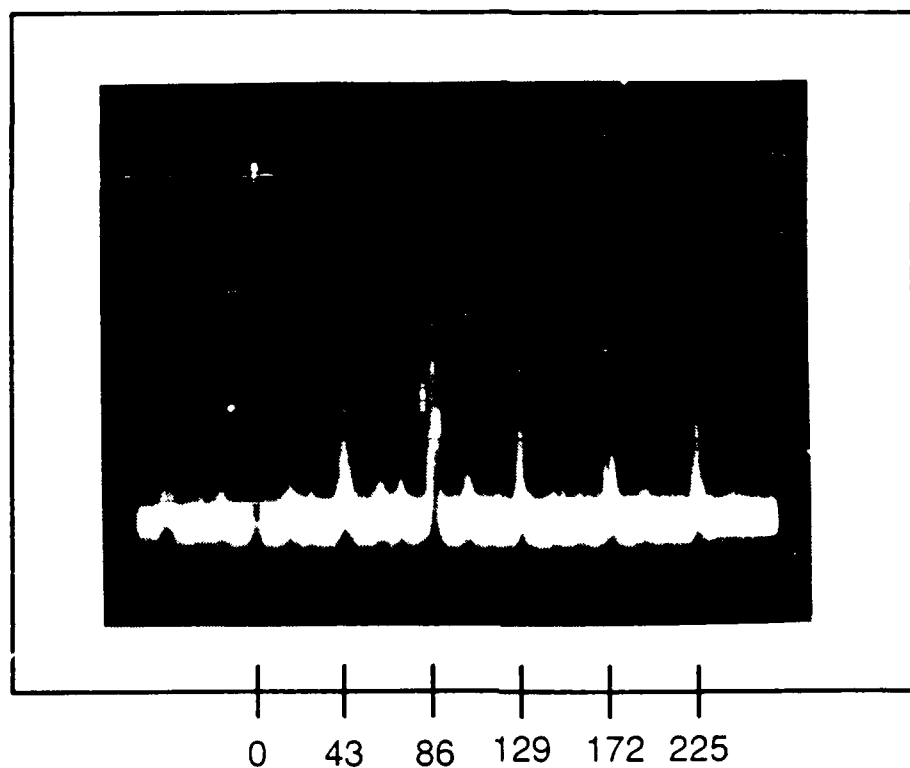
when treating the fringe production in terms of coherence packets.

The interference fringes are not formed exclusively from the phase-locked operation of the lasers. Consider a single packet of coherent photons. When the coherent packet is incident upon the coupling mirror, it is split into transmitted and reflected pieces. In some cases, both the transmitted and reflected packets travel back through the lasers without interacting with the media, along the coupling paths, and eventually arrive at the point of superposition at roughly the

same instant to form self-interference fringes. The desired outcome of coupling is for the two packets to influence both laser media to emit photons at the same frequency and in phase with each other, and to have these photons interfere to generate phase locked interference fringes. The resultant fringe pattern in the observation plane will be some combination of these two events.

Beginning from the left in Figures 4.5, 4.6, and 4.7 at 0% coupling, the curve should, in theory, show zero visibility because the two lasers are completely independent from each other. In the 10% to 20% coupling range, there is enough mutual injection to initiate phase locking and produce fringes. For these coupling strengths, there is also an RF mode beat at 43 MHz corresponding to the free spectral range of the super cavity, formed by the output couplers of Figures 3.1, 3.2, and 3.3, in addition to an 86 MHz mode beat from each subcavity (See Figure 4.8). With many modes in oscillation, the RF mode beat is not a single clean spike but an extended peak around 43 MHz with many secondary peaks caused by various beat combinations between the longitudinal and transverse modes. Increasing the coupling strength increases the fringe visibility to a local maximum near 25% coupling. Further increases in coupling strength begin to wash out the fringes because too much of the cavity's internal power is being transmitted to the coupled cavity, and the lasers lose their identities as separate oscillators. Each laser generates self-interference fringes from photons that don't interact with the coupled media to induce phase locking, and those fringes overlap and smear out any fringes produced from phase locking.

Beyond 50% coupling, the fringe visibility rises sharply, but this is no longer



Frequency (MHz)

Figure 4.8 Radio frequency mode beat spectrum of the multiline coupled lasers with a 70% reflective coupling mirror.

from phase locking but almost exclusively from self-interference. Each coherent packet of photons traversing the coupling mirror interferes with the reflected portion of the packet. The approximate equality in the coupling paths allows both packets leaving the coupling mirror to interfere with each other even if they do not contribute to phase locking. This can be seen from the fact that when one laser gain tube is off, the fringes are actually more stable and higher in visibility than with both tubes on. In the region of 60-70% coupling, there is no longer self-oscillation in the subcavities since the threshold for oscillation becomes too

high for those values, and the mode beat at 43 MHz narrows and becomes a single clean spike indicating all the subsidiary modes are extinguished. There are no longer two distinct lasers but one laser in a 3.5 m-long cavity with an internal perturbation caused by the weakly reflecting rear mirror. So much power is going into coupling that there is not enough intensity on each side of the coupled resonators for them to function as independent lasers. If the coupling mirror is removed for 100% coupling, the system becomes a single laser and is completely coherent with itself, but no fringes can be formed since a coherent packet leaving one output mirror is not coherent with the packet leaving the other output coupler at the same time. The two packets are separated by 3.5 m and well beyond the coherence length of the Ar-ion laser.

The visibility curves indicate an optimal coupling strength exists for the Ar-ion lasers around 25% transmission. As the fringes reach their highest phase-locked visibility at 25% coupling, the output laser power also reaches its maximum as well. Increasing the coupling strength not only decreases the output laser power, but it also inhibits phase locking. A similar phenomenon was observed in the frequency locking of semiconductor lasers using external feedback injection of the output beam. In the semiconductor lasers, the most stable frequency locked operation occurred at a finite injection level rather than increasing with increased power injection³⁰. The second maximum merely determines the optimal mirror parameters for production of high visibility self-interference fringes and the visibilities appear to reach a saturation limit around 75% coupling.

Now where does the event of 100% phase locking occur (i.e. a visibility meas-

urement of one). There are several possible explanations for this and one of the arguments is that there is competition for gain between 514.5 nm and 488.0 nm since both share a common lower laser level. Disturbances to the lasers will continually shift the relative strengths of the two competing lines and alter the fringe visibilities. Interestingly enough, 488.0 nm is the stronger transition, but the 514.5 nm line dominates in the multiline coupling. Even when operating on a single transition, there are evidently other perturbations of sufficient magnitude to prevent 100% phase locking.

Even if gain competition is not a significant contributor, there is another factor which turns out to be quite self-defeating when coupling lasers in standing-wave cavities. In his theoretical treatment of phase-locked lasers using the supermode expansion of the laser fields, Chow ²⁶ found that when there is strong coupling between the two lasers, symmetric and antisymmetric modes, which differ in phase from each other by π radians, oscillate simultaneously. (The two supermodes are the same frequency only when the lengths of the coupled cavities are equal.) Although it would be difficult to verify the presence of the symmetric and antisymmetric supermodes experimentally, if a mixture of these modes truly exists, then complete constructive interference would be extremely difficult to obtain because the maxima of the fringe pattern of one frequency would nearly overlap the minima of the fringe pattern of the other frequency creating a fairly uniform intensity distribution. The obvious result would certainly be fringe visibilities of less than $V=1.00$.

Another possible explanation can be found in the analysis of the resonant

modes of the three-mirror Fabry-Perot cavity used in the experiment. All the fields indicated in Figure 4.9 must satisfy stringent boundary conditions and conservation of energy at each interface and therefore a system of equations can be written for the cavity which specify the amplitude and phase of each field in terms of the other fields. Since the current interest is in the strength of each field when the lasers are oscillating on a phase-locked mode (a mode at the super-cavity frequency), one of many possible solutions is to set the round trip gain term for the left hand cavity, g , equal to the round trip gain term for the right hand cavity, h , thereby demanding solutions for the round trip gain which satisfies a super cavity mode. By enforcing a steady-state condition which means the fields must reproduce their amplitudes and phase after a round trip in order to constitute a mode, it was found that the system can oscillate at three different frequencies: the composite resonator frequency determined by $L_1 + L_2$, the frequency determined by $2L_1$, and the frequency determined by $2L_2$. For all cases, the magnitude of the of the round trip field amplitude gain was

$$g^4 = \frac{1}{r_1 r_3} \quad (4.1)$$

Incidentally, this is the same value for the round trip field amplitude gain for a two-mirror cavity. (For an in depth treatment of the passive cavity analysis along with other applications of this method, see Appendix C.) By substituting these values into the equations for the fields and choosing one field amplitude ($C=1.00$), the relative strengths of the remaining fields can be evaluated. Those field strengths at resonance for two 90% output couplers and a range of coupling

mirror reflectivities are found in Table 4.6.

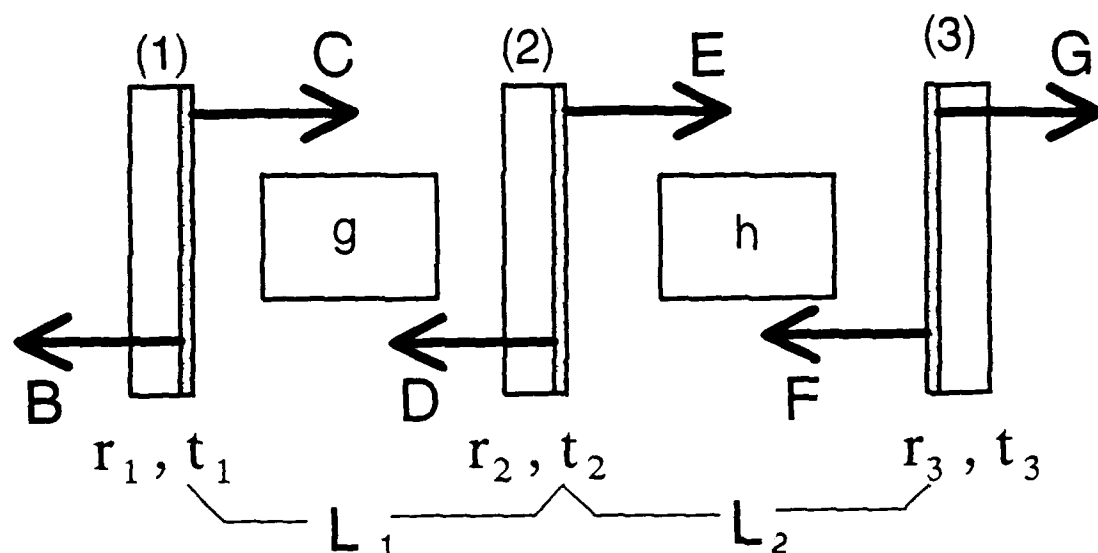


Figure 4.9: Fields, phases, mirror reflectivities and transmissivities, and round trip gains for a three mirror cavity.

Choosing the value for field C fixes the relationship between B , C , and D when the detuning is zero, but those field amplitudes are only equal with G , F , and E , respectively, when there is no coupling mirror. The imbalance in the intensity on each side of the resonator at any particular frequency or mode increases drastically as the reflectivity of the coupling mirror increases. The imbalance also alternates between the two cavities when the laser oscillates on the even or odd modes. At the mirror transmissions shown to generate optimal phase locking, the intensity imbalance is nearly its greatest. The intensity imbalance associated with the three mirror cavity may also explain, in part, why the intensities from the output couplers were not equal. The main point of this digression,

however, is that it is unlikely that the two lasers could phase lock completely when then there is such a disparity in the circulating intensities in the two cavities. It must be noted, however, that only selected values for g and h were examined. Incorporating a saturation model into this formulation may readjust the intensity imbalances predicted by the passive cavity analysis.

Table 4.2: Fringe Visibilities and Standard Deviations for Coupling without the Optical Trombone (R_c : Coupling Mirror Reflectivity, N: Number of Samples, V: Visibility, σ : Standard Deviation)

	Total			514.5 nm			488.0 nm		
R_c	N	V	σ	N	V	σ	N	V	σ
0.9	19	.226	.038	20	.483	.104	14	.319	.050
0.8	19	.307	.055	8	.511	.101	20	.324	.020
0.7	15	.300	.051	19	.454	.115	14	.312	.046
0.6	17	.254	.072	22	.396	.094	19	.257	.065
0.5	16	.202	.037	18	.372	.069	14	.196	.030
0.3	13	.279	.050	20	.599	.093	12	.322	.047
0.2	14	.259	.064	15	.756	.090	14	.330	.055
0.1	17	.298	.074	16	.800	.053	16	.340	.058

Table 4.3: Fringe Visibilities and Standard Deviations for Coupling with the Optical Trombone (R_c : Coupling Mirror Reflectivity, N: Number of Samples, V: Visibility, σ : Standard Deviation)

	Total			514.5 nm			488.0 nm		
R_c	N	V	σ	N	V	σ	N	V	σ
0.9	37	.382	.040	37	.668	.095	31	.447	.044
0.8	23	.412	.049	30	.717	.056	32	.446	.076
0.7	41	.448	.086	23	.660	.048	34	.459	.087
0.6	35	.375	.040	35	.622	.069	32	.401	.061
0.5	30	.361	.047	29	.632	.056	24	.394	.046
0.3	41	.424	.038	39	.810	.062	35	.474	.050
0.2	32	.441	.055	36	.851	.031	31	.514	.060
0.1	19	.492	.037	23	.858	.025	14	.535	.041

Table 4.4: Fringe Visibilities and Standard Deviations for Single Line Coupling (488.0 nm) with the Optical Trombone (R_c : Coupling Mirror Reflectivity, N: Number of Samples, V: Visibility, σ : Standard Deviation)			
R_c	N	V	σ
0.9	18	.330	.019
0.8	18	.228	.022
0.7	19	.574	.028
0.6	19	.465	.023
0.5	20	.333	.020
0.3	18	.656	.022
0.2	18	.751	.020
0.1	18	.815	.021

Table 4.5: Actual Coupling Mirror Reflectivities Measured with
a Spectrophotometer Compared to the Manufacturers
Specifications for the Experimental Wavelengths

R_c Specified (%)	Total (%)	514.5 nm (%)	488.0 nm (%)
90	88.5	87.8	89.7
80	82.5	82.5	81.0
70	70.0	68.0	73.0
60	60.0	57.5	63.0
50	55.0	53.5	55.7
30	29.4	29.4	26.0
20	7.0	6.3	7.7
10	24.5	24.0	25.0

Table 4.6: Wave Intensities for Passive Cavity Mode Analysis of
Two Coupled Fabry-Perot Resonators (R_2 : Coupling
Mirror Reflectivity; See Figure 4.9 for Symbols; $C=1.00$)

	0					$\frac{\pi}{2}$				
R_2	B	D	E	F	G	B	D	E	F	G
0.0	0.111	1.054	1.054	1.000	0.111	0.111	1.054	1.054	1.000	0.111
0.1	0.111	1.054	2.029	1.924	0.213	0.111	1.054	0.547	0.519	0.057
0.2	0.111	1.054	2.759	2.618	0.290	0.111	1.054	0.402	0.381	0.042
0.3	0.111	1.054	3.607	3.422	0.380	0.111	1.054	0.308	0.292	0.032
0.4	0.111	1.054	4.681	4.441	0.493	0.111	1.054	0.237	0.225	0.025
0.5	0.111	1.054	6.143	5.828	0.647	0.111	1.054	0.180	0.171	0.019
0.6	0.111	1.054	8.298	7.872	0.874	0.111	1.054	0.133	0.127	0.014
0.7	0.111	1.054	11.852	11.244	1.249	0.111	1.054	0.093	0.088	0.009
0.8	0.111	1.054	18.914	17.944	1.993	0.111	1.054	0.587	0.055	0.006
0.9	0.111	1.054	40.027	37.973	4.219	0.111	1.054	0.027	0.026	0.002

Chapter V. Conclusions and Recommendations

A wide variety of topics relating to phase locking lasers was studied during this dissertation research, so this chapter will highlight and summarize the findings and point out the original contributions to the field of coupled lasers. The first section will review the theoretical and experimental results, and the second section will advance some recommendations for further research, both theoretical and experimental, in coupled lasers.

A. Summary

The study of coupled lasers is currently and will continue to be an important area of research as the limits of technology are strained in development of high-energy lasers for both civilian and military applications. When two or more lasers are coherently combined, or phase locked, the effect of far-field narrowing increases the peak power density which scales as the square of the number of coupled lasers. This along with the graceful degradation of the systems realizes several of the criteria desirable in high-energy lasers.

Two coupled Ar-ion lasers each oscillating on a single mode were examined theoretically using pre-existing mathematical frameworks. Coupled lasers with homogeneous-broadened media have been studied previously, but although the theory existed, it had not been applied to Doppler-broadened media to compute intensity, frequency, and phase tuning curves until this analysis. By continuing the development, these theories were extended to model two modes oscillating in

each cavity containing Doppler-broadened media which also had not been accomplished before this dissertation research. Using a computer code programmed on a desktop computer to solve the single- and two-mode coupled systems, the solutions showed that the two laser cavities should be equal in length with frequencies detuned from the gain center to generate the maximum possible coherent output. Adding another mode to the single-mode lasers yielded a two-fold decrease in the laser locking range which is on the order of hundreds of nanometers for Ar-ion laser wavelengths. Without further investigation into multimode coupling, it is difficult to predict if this trend would continue as the number of modes in oscillation increases. Additionally, despite extensive observation of hole-burning phenomena by other researchers, the two-mode analysis uncovered a mutually-reinforced hole-burning minimum whose existence was verified experimentally with a two-mode He-Ne laser. A discovery of this nature adds credibility to the theoretical models in spite of the many necessary approximations involved in their formulation.

Using the fundamental configuration studied in the theoretical analysis, an experiment was performed on coupled Ar-ion lasers operating on multiple wavelengths and multiple modes with and without interference path length compensation and also operating on a single wavelength (488.0 nm). The Ar-ion lasers were chosen because the gain media exhibit many of the same media characteristics as the higher energy IIF and COIL lasers but can be operated for extended periods of time without any of the latter's associated hazards. To determine the degree of laser phase locking, near field interference fringes from the coherent mixing of the two output laser beams were measured as the amount of

coupling was varied from 10% to 90% of the internal laser intensity. The output power and the RF mode beat and frequency spectra were also measured to further characterize and aid in the understanding of the phase-locked behavior.

When the data collected was plotted as a function of the coupling mirror transmission, each of the three configurations showed that phase locking occurred for less than 50% coupling with the maximum phase-locked fringe visibility and the maximum output power at about 25% coupling before the deleterious affects of self-interference took over and dominated the coupled resonators. That the lasers were in fact phase locked was corroborated by the appearance of a 43 MHz RF mode beat which indicated the lasers were oscillating at the super-cavity frequency. In addition, it was found that phase locking occurs for low coupling strengths (10%) which was a fact notably in contrast to the expected behavior. Air turbulence, mode competition, mechanical vibrations, and thermal expansion and contraction caused the interference fringes to fluctuate and were also partly responsible for decreasing the fringe visibilities. The experimental results suggest that there is an optimum coupling strength for phase-locked operation of Ar-ion lasers. Apparently no other researcher has performed coupling experiments over a wide range of coupling strengths nor has any observed such an optimum operating condition. This knowledge may influence the design of future coupled laser experiments. Even though Ar-ion lasers will not be used for high-energy laser applications, the information from this experiment should be applicable to other lasers which also have Doppler-broadened gain media and possibly other types of lasers as well.

The desired condition of total phase-locked operation ($V=1.00$) was never reached. When several wavelengths oscillate, some of those wavelengths compete for the same gain. If the coupling is too strong and the symmetric and antisymmetric modes oscillate, their phase difference spoils near field interference. A passive cavity mode analysis showed that there is a severe imbalance in the internal intensities of the two coupled lasers. One or more of these factors serves to explain why complete phase locking was not achieved.

B. Recommendations

There are two areas of further theoretical research that are a logical extension of the theories discussed in this dissertation. Since there are equations which describe a laser in which three modes are oscillating (Lamb ²⁰), it would be possible, although painstaking and labor intensive, to solve the coupled laser system for three modes oscillating in each cavity. Results from such an analysis would provide valuable information in projecting the behavior of coupled lasers oscillating on many modes. The passive cavity mode analysis also seems to be crying out for application to active laser cavities. By including saturation expressions for the circulating intensities, the specific operating characteristics of the coupled lasers could be determined unambiguously.

Experimentally, similar studies to that undertaken in this research could be conducted with He-Ne, CO₂, Nd:YAG, and dye lasers to support or disprove the previous observations and continue to fill in some of the vast, unexplored frontier of coupled lasers. Finally, active stabilization could be implemented with the laser

cavities in an attempt to control and stabilize phase locking and fringe stability. It would then also be possible to investigate single- and two-mode coupling experimentally as well as theoretically.

C. Finis

This research touched a broad range of topics and at times appeared to ask as many, if not more, questions than it answered. The results are new, interesting, and valuable, but more importantly, the insight gained is applicable to continued research in this area. No aspect of the study of coupled lasers is even partially complete, but the contribution of this dissertation research has expanded the present knowledge base of an emerging field and hopefully will serve as a welcome trail blaze to those who follow.

Appendix A: Computer Simulation

This appendix consists of two sections of three parts each. In both parts, the first section will derive the mathematics necessary to cast the the coupled laser equations into forms suitable for computer simulations followed by the perturbation calculations used to check for solution stability. The third sections of each part contain the computer codes with explanations of their important features. The single-mode equations are treated first followed by the two-mode coupled laser equations.

A. Single-Mode Equations

i. Mathematics

Since the transients of the laser system diminish rapidly and are of little interest when considering continuous-wave lasers, only the steady-state solutions to the coupled laser equations are necessary. To obtain the steady-state solutions, each of the time derivatives of equations (2.20)-(2.23) in chapter II are set equal to zero. Because all the equations are similar in form and differ only in the signs and subscripts, only one field and one phase equation will be manipulated. With the symbols explicitly written, the equations are

$$\begin{aligned} F(1) = \frac{F_{1A}}{\gamma} e^{-\left(\frac{\gamma}{\gamma_d}\right)^2 \xi^2} - \frac{F_{2A}}{\gamma} - \frac{F_{3A}}{\gamma} I_A [1 + (1 + \xi^2)^{-1}] \\ + \frac{M_A}{I} \left(\frac{I_B}{I_A} \right)^{\frac{1}{2}} \cos(\phi + \psi) = 0 \end{aligned} \quad (\text{A.1})$$

$$F(3) = \xi - \Delta_A + 2 \frac{F_{1A}}{\gamma} e^{-\left(\frac{\gamma}{\gamma_d}\right)^2 \xi^2} \int_0^{\frac{\gamma}{\gamma_d} \xi} e^{x^2} dx - \frac{F_{1A}}{\gamma} I_A \xi (1 + \xi^2)^{-1} \quad (\text{A.2})$$

$$+ \frac{M_A}{\gamma} \left(\frac{I_B}{I_A} \right)^{\frac{1}{2}} \sin(\phi + \psi) = 0$$

Even though the distinction between F_{nA} and F_{nB} is retained throughout this treatment, these coefficients are equal because it is assumed that both laser gain media are identical, but this need not be true in general. The variables of interest are I_A , I_B , ξ , and $\sin\phi$. To employ the Newton-Raphson method ²², the Jacobi matrix consisting of four partial differentials for each of the four equations is formed:

$$J(I_A, I_B, \xi, \sin\phi) = \begin{bmatrix} \frac{\partial F(1)}{\partial I_A} & \frac{\partial F(1)}{\partial I_B} & \frac{\partial F(1)}{\partial \xi} & \frac{\partial F(1)}{\partial \sin\phi} \\ \frac{\partial F(2)}{\partial I_A} & \frac{\partial F(2)}{\partial I_B} & \frac{\partial F(2)}{\partial \xi} & \frac{\partial F(2)}{\partial \sin\phi} \\ \frac{\partial F(3)}{\partial I_A} & \frac{\partial F(3)}{\partial I_B} & \frac{\partial F(3)}{\partial \xi} & \frac{\partial F(3)}{\partial \sin\phi} \\ \frac{\partial F(4)}{\partial I_A} & \frac{\partial F(4)}{\partial I_B} & \frac{\partial F(4)}{\partial \xi} & \frac{\partial F(4)}{\partial \sin\phi} \end{bmatrix} \quad (\text{A.3})$$

where

$$\frac{\partial F(1)}{\partial I_A} = -\frac{F_{1A}}{\gamma} [1 + (1 + \xi^2)^{-1}] - \frac{1}{2} \frac{M_A}{I_A} \left(\frac{I_B}{I_A} \right)^{\frac{1}{2}} \cos(\phi + \psi) = J(1,1) \quad (\text{A.4})$$

$$\frac{\partial F(1)}{\partial I_B} = \frac{1}{2} M_A (I_A I_B)^{-\frac{1}{2}} \cos(\phi + \psi) = J(1,2) \quad (\text{A.5})$$

$$\frac{\partial F(1)}{\partial \xi} = 2\xi \frac{F_{1A}}{\gamma} \left[I_A (1 + \xi^2)^{-2} - \left(\frac{\gamma}{\gamma_d} \right)^2 e^{-\left(\frac{\gamma}{\gamma_d}\right)^2 \xi^2} \right] = J(1,3) \quad (\text{A.6})$$

$$\frac{\partial F(1)}{\partial \sin \phi} = -M_A \left(\frac{I_B}{I_A} \right)^{\frac{1}{2}} [\sin \phi \cos \psi (1 - \sin^2 \phi)^{-\frac{1}{2}} + \sin \psi] = J(1,4) \quad (A.7)$$

and

$$\frac{\partial F(3)}{\partial I_A} = -\frac{F_{1A}}{\gamma} \xi (1 + \xi^2)^{-1} - \frac{1}{2} \frac{M_A}{I_A} \left(\frac{I_B}{I_A} \right)^{\frac{1}{2}} \sin(\phi + \psi) = J(3,1) \quad (A.8)$$

$$\frac{\partial F(3)}{\partial I_B} = \frac{1}{2} M_A (I_A I_B)^{-\frac{1}{2}} \sin(\phi + \psi) = J(3,2) \quad (A.9)$$

$$\begin{aligned} \frac{\partial F(3)}{\partial \xi} &= 1 - 4 \frac{F_{1A}}{\gamma} \xi \left(\frac{\gamma}{\gamma_d} \right)^2 e^{-\left(\frac{\gamma}{\gamma_d} \right)^2 \xi^2} \int_0^{\frac{\gamma}{\gamma_d} \xi} e^{x^2} dx + 2 \frac{F_{1A}}{\gamma} \left(\frac{\gamma}{\gamma_d} \right) \\ &\quad - \frac{F_{1A}}{\gamma} I_A (1 + \xi^2)^{-\frac{1}{2}} + 2 \frac{F_{1A}}{\gamma} I_A \xi^2 (1 + \xi^2)^{-2} = J(3,3) \end{aligned} \quad (A.10)$$

$$\frac{\partial F(3)}{\partial \sin \phi} = M_A \left(\frac{I_B}{I_A} \right)^{\frac{1}{2}} [\cos \psi - \sin \phi \sin \psi (1 - \sin^2 \phi)^{-\frac{1}{2}}] = J(3,4) \quad (A.11)$$

Notice that the equations are solved for $\sin \phi$ rather than ϕ to eliminate some operations and to simplify the equations. The Jacobian is used to solve the matrix equation

$$J(x_1, x_2, x_3, x_4) X(x_1, x_2, x_3, x_4) = F(x_1, x_2, x_3, x_4) \quad (A.12)$$

(where J is the Jacobian, X is the solution vector, and F is the steady-state equation vector) by choosing an initial guess vector for the variables and iterating until the matrix equation converges to a self-consistent solution. For a tolerance of one part in a million, a convergent solution was usually produced in less than 10 iterations taking 2-3 seconds of computing time. Each solution served as the

initial estimate for the next detuning step, so subsequent solutions required fewer iterations. Experience showed that $X = [0.1, 0.1, 0.1, 0.0]$ was a good initial guess. Wild guesses, especially for the ξ term, commonly forced the solutions to diverge.

ii. Stability

Once a solution vector was determined, it was checked for stability by performing a perturbation calculation on the time-dependent field amplitude equations and an equation containing the phase difference:

$$\begin{aligned} \frac{d\phi_{BA}}{dt} = \frac{d\phi_B}{dt} - \frac{d\phi_A}{dt} = & \gamma (\Delta_A - \Delta_B) + 2 (F_{1B} F_{1A}) e^{-\left(\frac{\gamma}{\gamma_d}\right)^2 \xi^2} \int_0^{\frac{\gamma}{\gamma_d} \xi} e^{-x^2} dx \\ & + (F_{3A} I_A - F_{3B} I_B) \xi (1 + \xi^2)^{-1} - M_B \left(\frac{E_A}{E_B} \right) \sin(\phi - \psi) \\ & - M_A \left(\frac{E_B}{E_A} \right) \sin(\phi + \psi) \end{aligned} \quad (\text{A.13})$$

The perturbation calculation is done by solving for the eigenvalues of the matrix equation

$$\begin{bmatrix} \Delta \dot{E}_A \\ \Delta \dot{E}_B \\ E_A \Delta \dot{\phi} \end{bmatrix} = \begin{bmatrix} a & b & c \\ d & e & f \\ g & h & j \end{bmatrix} \begin{bmatrix} \Delta E_A \\ \Delta E_B \\ E_A \Delta \phi \end{bmatrix} \quad (\text{A.14})$$

where each row of the equation is computed according to the general form of

$$\Delta G = \frac{\partial G}{\partial E_A} \Delta E_A + \frac{\partial G}{\partial E_B} \Delta E_B + \frac{\partial G}{\partial \phi} \Delta \phi \quad (\text{A.15})$$

and $G = \frac{dE_A}{dt}$, $\frac{dE_B}{dt}$, or $\frac{d\phi_{BA}}{dt}$. The elements of the coefficient matrix can be found in Table A.1.

Table A.1: Single-Mode Perturbation Matrix Coefficients

$$\begin{aligned} a &= F_{1A} e^{-\left(\frac{\gamma}{\gamma_d}\right)^2 \xi^2} - F_{2A} - 3F_{3A} E_A^2 [1 + (1 + \xi^2)^{-1}] \\ b &= M_A \cos(\phi + \psi) \\ c &= -M_A \left(\frac{E_A}{E_B} \right) \sin(\phi + \psi) \\ d &= M_B \cos(\phi - \psi) \\ e &= F_{1B} e^{-\left(\frac{\gamma}{\gamma_d}\right)^2 \xi^2} - F_{2B} - 3F_{3B} [1 + (1 + \xi^2)^{-1}] \\ f &= -M_B \sin(\phi - \psi) \\ g &= -M_B \left(\frac{E_A}{E_B} \right) \sin(\phi - \psi) + 2F_{3A} \xi (1 + \xi^2)^{-1} E_A^2 + M_A \left(\frac{E_B}{E_A} \right) \sin(\phi + \psi) \\ h &= -2F_{3B} \xi (1 + \xi^2)^{-1} E_A E_B + M_B \left(\frac{E_A}{E_B} \right)^2 \sin(\phi - \psi) - M_A \sin(\phi + \psi) \\ j &= -M_B \left(\frac{E_A}{E_B} \right) \cos(\phi - \psi) - M_A \left(\frac{E_A}{E_B} \right) \cos(\phi + \psi) \end{aligned}$$

The solution of the stationary state is stable if all the real parts of the eigenvalues are negative. For a 3×3 perturbation calculation, it is possible to analyti-

cally determine the conditions necessary to satisfy such a constraint. The stability criteria, already derived by Spencer and Lamb ¹² are

$$\begin{aligned}\nu_1 &> 0 \\ \nu_1 \nu_2 &> \nu_3 \\ \nu_3 &> 0\end{aligned}\tag{A.16}$$

where

$$\nu_1 = -(a + e + j)\tag{A.17}$$

$$\nu_2 = a(e + j) + ej - hf - bd - cg\tag{A.18}$$

$$\nu_3 = a(hf - ej) + b(dj - fg) + c(eg - dh)\tag{A.19}$$

iii. Computer Program for Single-Mode Coupled Laser Equations

Translating the single-mode coupled laser equations into acceptable computer language was not a difficult problem. Because of the inherent flexibilities of desktop personal computers, the equations were coded in the BASIC language for a Zenith Z-248 computer to allow for easy parameter variations. The code is explained in the paragraphs to follow.

The first 16 lines of the program input the parameters into the machine. The coded parameters are cross-referenced to the equation parameters in Table A.2. In this example of the code, the input parameters are for a coupling mirror of $R_c = 0.9$.

```

10 CLEAR
20 CLS
30 DIM A(10,10),M(10,10),J(10,10)
40 L1=1.75
50 L2=1.75
60 N=4
70 M1=.1187
80 M2=M1
90 AA=.2708
100 AB=AA
110 BA=.03754
120 BB=BA
130 SG=2.404E+08
140 G=.009568
150 GAM1=9025000
160 GAM2=GAM1

```

Table A.2: Definitions of Computer Symbols

$M1, M2 = \frac{M_A}{\gamma}, \frac{M_B}{\gamma}$	$BA, BB = \frac{F_{2A}}{\gamma}, \frac{F_{2B}}{\gamma}$
$AA, AB = \frac{F_{1A}}{\gamma}, \frac{F_{1B}}{\gamma}$	$SG = \gamma$
$GAM1, GAM2 = \Gamma_A, \Gamma_B$	$G = \frac{\gamma}{\gamma_d}$
$PSI = \psi$	$PHI = \phi$

Because the polarization expressions for a Doppler-broadened medium contain integrals, those integrals must be evaluated for each value of ξ . The next four values are the constants used for the five-point Gaussian quadrature needed to evaluate the integrals.

```

170 X1=.7745967
180 X2=0

```


190 W1=.5555556

200 W2=.8888889

The desired tolerance is defined

210 TOL=.000001

and then the initial guess vector is input from the keyboard

220 PRINT "ENTER THE INITIAL GUESS VECTOR: I1,I2,Z,SINPHI"

230 FOR I=1 TO N

240 INPUT X(I)

250 NEXT I

where $X(1) = I1 = I_A$, $X(2) = I2 = I_B$, $X(3) = Z = \xi$, and $X(4) = SF = \sin\phi$

along with the choice of phase angle ψ :

260 INPUT "ENTER THE PHASE ANGLE PSI ",PSI

Since certain functional forms are repeated frequently throughout the computer code, two general functions were defined

270 DEF FNE(X)=EXP(-G^2*X^2)

280 DEF FNZ(X)=1/(1+X^2)

where

$$FNE = e^{-\left(\frac{\gamma}{\gamma_d}\right)^2 x^2} \quad (A.20)$$

and

$$FNZ = [1 + \xi^2]^{-1} \quad (A.21)$$

The next three steps are important because they determine exactly how the cavity mirrors are displaced while tuning and how far the cavities are detuned.

```
290 FOR COUNT=0 TO .2 STEP .01
300 D1=COUNT
310 D2=D1
```

The COUNT variable is a measure of the number of halfwidths of the power-broadened linewidth, γ , the mirrors are to be detuned. D1 corresponds to Δ_A and $D2 = \Delta_B$. When $D1 = D2$, both output mirrors are translated simultaneously. If $D2 = 0$, then only a single output mirror is displaced, but if $D2 = -D1$, the central coupling mirror is tuned. Positive values of COUNT decrease the cavity length while negative values increase it.

Variable K is the abort counter used in case the program does not converge within the specified number of iterations. A maximum of $K < 100$ was adequate. Next, the input vector is converted to the equation variables and the integral is also computed

```
320 K=1
330 I1=X(1)
340 I2=X(2)
350 Z=X(3)
360 SF=X(4)
370 GD=ABS(Z)*G/2
380 NT=GD*(W1*EXP((GD*(X1+1))^2)+W2*EXP((GD*(X2+1))^2)
      +W1*EXP((GD*(1-X1))^2))
```

where

$$NT = \int_0^{\frac{\gamma}{\gamma_d} \xi} e^{x^2} dx \quad (A.22)$$

The next 20 lines define the equation vector, F(x), and the Jacobi matrix, J(x,y), and the abort counter is checked before proceeding.

```

390 F(1)=AA*FNE(Z)-BA-AA*I1*(1+FNZ(Z))+M1*(I2/I1)^.5*(COS(PSI)
      *(1-SF^2)^.5-SF*SIN(PSI))
400 F(2)=AB*FNE(Z)-BB-AB*I2*(1+FNZ(Z))+M2*(I1/I2)^.5*(COS(PSI)
      *(1-SF^2)^.5+SF*SIN(PSI))
410 F(3)=Z-D1+2*AA*FNE(Z)*NT-AA*I1*Z*FNZ(Z)+M1*(I2/I1)^.5
      *(SF*COS(PSI)+SIN(PSI)*(1-SF^2)^.5)
420 F(4)=Z-D2+2*AB*FNE(Z)*NT-AB*I2*Z*FNZ(Z)-M2*(I1/I2)^.5
      *(SF*COS(PSI)-SIN(PSI)*(1-SF^2)^.5)
430 J(1,1)=-AA*(1+FNZ(Z))-5*M1*(I2/I1)^.5*(1/I1)*(COS(PSI)
      *(1-SF^2)^.5-SF*SIN(PSI))
440 J(1,2)=.5*M1*(I1*I2)^.5*(COS(PSI)*(1-SF^2)^.5-SF*SIN(PSI))
450 J(1,3)=-AA*G^2*Z*FNE(Z)+AA^2*Z*I1*(FNZ(Z))^2
460 J(1,4)=-M1*(I2/I1)^.5*(SF*COS(PSI)*(1-SF^2)^.5+SIN(PSI))
470 J(2,1)=.5*M2*(I1*I2)^.5*(COS(PSI)*(1-SF^2)^.5+SF*SIN(PSI))
480 J(2,2)=-AB*(1+FNZ(Z))-5*M2*(I1/I2)^.5*(1/I2)*(COS(PSI)
      *(1-SF^2)^.5+SF*SIN(PSI))
490 J(2,3)=-AB*G^2*Z*FNE(Z)+AB^2*Z*I2*(FNZ(Z))^2
500 J(2,4)=M2*(I1/I2)^.5*(-SF*COS(PSI)*(1-SF^2)^.5+SIN(PSI))
510 J(3,1)=-AA*Z*FNZ(Z)-5*(M1/I1)*(I2/I1)^.5*(SF*COS(PSI)
      +SIN(PSI)*(1-SF^2)^.5)
520 J(3,2)=(M1/2)*(I1*I2)^.5*(SF*COS(PSI)+SIN(PSI)*(1-SF^2)^.5)
530 J(3,3)=1-4*AA*NT*G^2*Z*FNE(Z)+2*AA*G-AA*I1*FNZ(Z)
      +2*Z^2*AA*I1*(FNZ(Z))^2
540 J(3,4)=M1*(I2/I1)^.5*(COS(PSI)-SF*SIN(PSI)*(1-SF^2)^.5)
550 J(4,1)=-.5*M2*(I1*I2)^.5*(SF*COS(PSI)-SIN(PSI)*(1-SF^2)^.5)
560 J(4,2)=-AB*Z*FNZ(Z)+.5*(M2/I2)*(I1/I2)^.5*(SF*COS(PSI)
      -SIN(PSI)*(1-SF^2)^.5)
570 J(4,3)=1-4*AB*NT*G^2*Z*FNE(Z)+2*AB*G-AB*I2*FNZ(Z)
      +2*Z^2*AB*I2*(FNZ(Z))^2
580 J(4,4)=-M2*(I1/I2)^.5*(COS(PSI)+SIN(PSI)*SF*(1-SF^2)^.5)
590 IF K>100 THEN 1230

```

Once all the parameters, equations, and matrices have been digested, the next routine searches for a self-consistent solution to the matrix equation (A.12).

```

600 FOR R=1 TO N
610 FOR Q=1 TO N
620 A(R,Q)=J(R,Q)
630 NEXT Q
640 A(R,N+1)=F(R)

```

```

650 NEXT R
660 FOR I=1 TO N-1
670 FOR J=I+1 TO N
680 M(J,I)=A(J,I)/A(I,I)
690 FOR Q=1 TO N+1
700 A(J,Q)=A(J,Q)-M(J,I)*A(I,Q)
710 NEXT Q
720 NEXT J
730 NEXT I
740 Y(N)=A(N,N+1)/A(N,N)
750 FOR I=N-1 TO 1 STEP-1
760 FOR J=I+1 TO N
770 P=P+A(I,J)*Y(J)
780 NEXT J
790 Y(I)=(A(I,N+1)-P)/A(I,I)
800 P=0
810 NEXT I
820 FOR I=1 TO N
830 X(I)=X(I)-Y(I)
840 NEXT I
850 MAX=0
860 FOR I=1 TO N
870 IF ABS(Y(I))<=MAX THEN 890
880 MAX=ABS(Y(I))
890 NEXT I
900 IF MAX<TOL THEN 930
910 K=K+1
920 GOTO 330

```

The matrix system is solved using the Newton-Raphson method ²² which is outlined below:

To solve $F(x) = 0$ given an initial guess vector X to within a predefined tolerance:

1. Calculate $F(x_1, x_2, x_3, x_4)$ and $J(x_1, x_2, x_3, x_4)$.
2. Solve the 4 X 4 system $J(x) Y = - F(x)$ for the small correction Y .
3. Add the small correction Y to X

$$X = X + Y$$

4. When Y is less than the tolerance, a solution has been reached, otherwise repeat from step 1.

After a solution is found, the vector is printed along with the coherent intensity,

IC:

```
930 PRINT "THE FREQUENCY OFFSET IS ";COUNT
940 PRINT
950 PRINT "THE SOLUTION VECTOR IS "
960 FOR I=1 TO N
970 PRINT "X(";I;")= ";X(I)
980 NEXT I
990 IC=X(1)+X(2)+2*(X(1)*X(2))^.5*(1-X(4)^2)^.5
1000 PRINT
1010 PRINT "THE COHERENT INTENSITY IS ";IC
1020 PRINT
```

The final subsections check each solution for stability:

```
1030 PHI=ATN(SF/((1-SF^2)^.5))
1040 A1=SG*AA*FNE(Z)-GAM1-3*I1*AA*SG*(1+FNZ(Z))
1050 B1=SG*M1*COS(PHI+PSI)
1060 C1=-SG*M1*(I2/I1)^.5*SIN(PHI+PSI)
1070 D3=SG*M2*COS(PHI-PSI)
1080 E1=AB*SG*FNE(Z)-GAM2-3*I2*AB*SG*(1+FNZ(Z))
1090 F1=-SG*M2*SIN(PHI-PSI)
1100 G1=2*Z*AA*SG*FNZ(Z)*I1+SG*(-M2*(I1/I2)^.5*SIN(PHI-PSI)
      +M1*(I2/I1)^.5*SIN(PHI+PSI))
1110 H1=-2*Z*AB*SG*(I1*I2)^.5*FNZ(Z)+SG*(M2*(I1/I2)*SIN(PHI-PSI)
      -M1*SIN(PHI+PSI))
1120 J1=-SG*(M2*(I1/I2)^.5*COS(PHI-PSI)+M1*(I2/I1)^.5*COS(PHI+PSI))
1130 NU1=-(A1+E1+J1)
1140 NU2=A1*(E1+J1)+E1*J1-H1*F1-B1*D3-C1*G1
1150 NU3=A1*(H1*F1-E1*J1)+B1*(D3*J1-F1*G1)+C1*(E1*G1-D3*H1)
1160 PRINT "NU1= ";NU1
1170 PRINT "NU2= ";NU2
1180 PRINT "NU3= ";NU3
1190 PRINT "NU1*NU2= ";NU1*NU2
1200 PRINT
1210 NEXT COUNT
1220 END
```

The value for ϕ is extracted from $\sin \phi$, and then the computed values from Table A.1 are inserted into the stability criteria equations (A.16-A.19) and printed. At this juncture, one complete solution has been determined, and the loop is repeated

for the next mirror displacement. The final line of the code is the abort message:

1230 PRINT "EXCEDED MAXIMUM NUMBER OF STEPS"

B. Two-Mode Equations

i. Mathematics

The reduction of the two-mode equations to expressions usable by a computer is understandably quite similar to the treatment of the single-mode equations even though many more terms are involved. As in the first section, only one field and one phase equation will be treated because there are no fundamental mathematical difference between them and the other six equations and their derivatives. The time derivatives of equations (2.27)- (2.34) of chapter II are set to zero, and the two representative equations explicitly written are

$$\begin{aligned}
 F(1) = & \frac{F_{1A}}{\gamma} e^{-\left(\frac{\gamma}{\gamma_d}\right)^2 \xi_1^2} - \frac{F_{2A}}{\gamma} - \frac{F_{3A}}{\gamma} I_{A1} [1 + (1 + \xi^2)^{-1}] \\
 & - \frac{F_{3A}}{\gamma} [R_c I_{A2} + T_c I_{B2} + 2 (R_c T_c I_{A2} I_{B2})^{-\frac{1}{2}} \cos(\phi_2 + \psi)] \\
 & \{ [1 + \frac{1}{4} (\xi_1 + \xi_2)^2]^{-1} + [1 + \frac{1}{4} (\xi_1 - \xi_2)^2]^{-1} \\
 & + [1 + (\xi_1 - \xi_2)^2]^{-1} [1 + \xi_1^2]^{-1} [1 - \xi_1 (\xi_1 - \xi_2)] \\
 & + [1 + (\xi_1 - \xi_2)^2]^{-1} [1 + \frac{1}{4} (\xi_1 - \xi_2)^2]^{-1} [1 - \frac{1}{2} (\xi_1 - \xi_2)^2] \} \\
 & + \frac{M_A}{\gamma} \left(\frac{I_{B1}}{I_{A1}} \right)^{\frac{1}{2}} \cos(\phi_1 + \psi) = 0
 \end{aligned} \tag{A.23}$$

$$\begin{aligned}
F(5) = & \xi_1 - \Delta_A - \delta_A + 2 \frac{F_{1A}}{\gamma} e^{-\left(\frac{\gamma}{\gamma_d}\right)^2 \xi_1^2} \int_0^{\frac{\gamma \xi_1}{\gamma_d}} e^{x^2} dx - \frac{F_{3A}}{\gamma} I_{A1} [1 + \xi^2]^{-1} \\
& - \frac{1}{2} \frac{F_{3A}}{\gamma} [R_c I_{A2} + T_c I_{B2} + 2 (R_c T_c I_{A2} I_{B2})^{\frac{1}{2}} \cos(\phi_2 + \psi)] \\
& \{(\xi_1 + \xi_2) [1 + \frac{1}{4} (\xi_1 + \xi_2)^2]^{-1} + (\xi_1 - \xi_2) [1 + \frac{1}{4} (\xi_1 - \xi_2)^2]^{-1} \quad (A.24) \\
& - 2 (2\xi_1 - \xi_2) [1 + (\xi_1 - \xi_2)^2]^{-1} [1 + \xi_1^2]^{-1} \\
& - 3 (\xi_1 - \xi_2) [1 + (\xi_1 - \xi_2)^2]^{-1} [1 + \frac{1}{4} (\xi_1 - \xi_2)^2]^{-1} \} \\
& + \frac{M_A}{\gamma} \left[\frac{I_{B1}}{I_{A1}} \right]^{\frac{1}{2}} \sin(\phi_1 + \psi) = 0
\end{aligned}$$

From the preceding equations, it is readily apparent that great care must be taken to ensure that all signs and subscripts are accurately transcribed during each step of the development. One saving grace is that there are many symmetric relationships which can be exploited, so it is only truly necessary to compute the partial derivatives of the two previous equations and then perform the appropriate sign and subscript changes to generate the 48 remaining matrix elements. The reader will be relieved to see that the partial derivatives will not be written in the interest of brevity.

Solutions for the two-mode equations are produced in exactly the same manner as the single-mode equations, except an eight-element guess vector, X , is substituted into the 8×8 Jacobian, J , and eight-element steady-state equation vector, F . Self-consistent solutions converged to within a tolerance of less than one part in a million again in less than 10 iterations, but the computer time was increased

to 10-15 seconds per detuning step with an initial input vector of

$$X = [0.1, 0.1, 0.1, 0.1, 0.1, 0.1, 0.0, 0.0].$$

ii. Stability

To check each solution for stability, a perturbation calculation was performed on the four time-dependent field equations and two equations formed from the difference between each pair of time-dependent phase equations:

$$\begin{aligned} \dot{\phi}_{B1} - \dot{\phi}_{A1} = \dot{\phi}_{31} = & \gamma (\Delta_A + \delta_A - \Delta_B - \delta_B) + \rho_1 (I_{A1} - I_{B1}) \\ & + \tau_{12} [R_c I_{A2} + T_c I_{B2} + 2 (R_c T_c)^{\frac{1}{2}} E_{A2} E_{B2} \cos(\phi_2 + \psi) \\ & - (R_c I_{B2} + T_c I_{A2} + 2 (R_c T_c)^{\frac{1}{2}} E_{A2} E_{B2} \cos(\phi_2 - \psi)] \\ & - M_A \left(\frac{E_{B1}}{E_{A1}} \right) \sin(\phi_1 + \psi) - M_B \left(\frac{E_{A1}}{E_{B1}} \right) \sin(\phi_1 - \psi) \end{aligned} \quad (A.25)$$

and a similar expression for $\dot{\phi}_{B2} - \dot{\phi}_{A2}$. The perturbation matrix

$$\begin{bmatrix} \Delta \dot{E}_{A1} \\ \Delta \dot{E}_{B1} \\ \Delta \dot{E}_{A2} \\ \Delta \dot{E}_{B2} \\ \Delta \dot{\phi}_{31} \\ \Delta \dot{\phi}_{42} \end{bmatrix} = \begin{bmatrix} a & b & c & d & e & f \\ g & h & i & j & k & l \\ m & n & o & p & q & r \\ s & t & u & v & w & x \\ y & z & aa & bb & cc & dd \\ ee & ff & gg & hh & ii & jj \end{bmatrix} \begin{bmatrix} \Delta E_{A1} \\ \Delta E_{B1} \\ \Delta E_{A2} \\ \Delta E_{B2} \\ \Delta \phi_{31} \\ \Delta \phi_{42} \end{bmatrix} \quad (A.26)$$

is produced by taking the total derivative of each of the six time-dependent equations according to

$$\Delta G = \frac{\partial G}{\partial E_{A1}} \Delta E_{A1} + \frac{\partial G}{\partial E_{B1}} \Delta E_{B1} + \frac{\partial G}{\partial E_{A2}} \Delta E_{A2} + \frac{\partial G}{\partial E_{B2}} \Delta E_{B2} + \frac{\partial G}{\partial \phi_{31}} \Delta \phi_{31} + \frac{\partial G}{\partial \phi_{42}} \Delta \phi_{42} \quad (A.27)$$

(For the expressions contained in the perturbation matrix, consult the values of

B(i,j) in lines 1930-2280 of the computer listing which follows.) Each stationary state of the two-mode system will be stable if the eigenvalues of the matrix equation (A.26) have negative real parts. In the case of a 6 X 6 matrix, no simple analytical solution is possible for such complicated elements. Therefore, the eigenvalues were computed numerically by first balancing the matrix, casting it into an upper Hessenberg matrix, and then using a numerical routine from Press, *et.al.'s Numerical Recipes* ²⁷.

iii. Computer Program for Two-Mode Coupled Laser Equations

Since the framework of the computer codes were the same for both the single- and two-mode programs, only the unique features of the second code will be discussed in detail. The first 47 lines of the program perform the same function as the first 40 lines of the single-mode program except the number of elements in the input vector is doubled and the free spectral range of the cavity is defined in line 70.

```

10 CLEAR
20 CLS
30 DIM A(10,10), M(10,10), J(10,10), B(10,10), WR(10), WI(10)
40 L1=1.75
50 L2=1.75
60 N=8
70 FSR=3.2724
80 M1=.8506
90 MT=.4
100 MR=.6
110 M2=M1
120 F11=.7916
130 F12=F11
140 F21=.3211
150 F22=F21

```

```

160 SG=8.223E+07
170 G=.003272
180 GAM1=2.693E+07
190 GAM2=GAM1
200 X1=.7745967
210 X2=0
220 W1=.5555556
230 W2=.8888889
240 TOL=.000001
250 PRINT "ENTER THE INITIAL GUESS VECTOR: I1,I2,I3,I4,Z1,Z2,SINPHI31,SINPHI42"
260 FOR I=1 TO N
270 INPUT X(I)
280 NEXT I
290 INPUT "ENTER THE PHASE ANGLE PSI ", PSI
300 DEF FNE (X)=EXP(-G^2 * X^2)
310 DEF FNZ (X) = 1/(1 + X^2)
320 FOR COUNT = 0 TO 20 STEP .1
330 D1=COUNT
340 D2=-D1
350 K=1
360 I1=X(1)
370 I2=X(2)
380 I3=X(3)
390 I4=X(4)
400 Z1=X(5)
410 Z2=X(6)
420 SF31=X(7)
430 SF42=X(8)
440 GD1=ABS(Z1) * G/2
450 GD2=ABS(Z2) * G/2
460 NT1=GD1*(W1*EXP((GD1*(X1+1))^2)+W2*EXP((GD1*(X2+1))^2)
      +W1*EXP((GD1 * (1 - X1))^2))
470 NT2=GD2*(W1*EXP((GD2*(X1+1))^2)+W2*EXP((GD2*(X2+1))^2)
      +W1*EXP((GD2*(1-X1))^2))

```

The input parameters describe the system with a coupling mirror of 60% reflectivity. Because some of the equations are unmanageably large and also because many common expressions are frequently repeated, lines 480 through 710 divide the functions of ξ_1 and ξ_2 into acceptable lengths. Lines 720-750 contain the coherent mixing expressions used with the cross saturation and cross pushing terms.

480 FACT1=FNZ(.5*Z1+.5*Z2)+FNZ(.5*Z1-.5*Z2)+FNZ(Z1)
 FNZ(Z1-Z2)(1-Z1*(Z1-Z2))+(1-.5*(Z1-Z2)^2)
 *FNZ(Z1-Z2)*FNZ(.5*Z1-.5*Z2)
 490 FACT2=FNZ(.5*Z1+.5*Z2)+FNZ(.5*Z2-.5*Z1)+FNZ(Z2)
 FNZ(Z2-Z1)(1-Z2*(Z2-Z1))+(1-.5*(Z2-Z1)^2)
 *FNZ(Z2-Z1)*FNZ(.5*Z2-.5*Z1)
 500 FACT3=(Z1+Z2)*FNZ(.5*Z1+.5*Z2)+(Z1-Z2)*FNZ(.5*Z1-.5*Z2)
 -2*(2*Z1-Z2)*FNZ(Z1-Z2)*FNZ(Z1)-3*(Z1-Z2)
 *FNZ(Z1-Z2)*FNZ(.5*Z1-.5*Z2)
 510 FACT4=(Z1+Z2)*FNZ(.5*Z1+.5*Z2)+(Z2-Z1)*FNZ(.5*Z2-.5*Z1)
 -2*(2*Z2-Z1)*FNZ(Z2-Z1)*FNZ(Z2)-3*(Z2-Z1)
 *FNZ(Z2-Z1)*FNZ(.5*Z2-.5*Z1)
 520 FACT11=-.5*(Z1+Z2)*FNZ(.5*Z1+.5*Z2)^2-.5*(Z1-Z2)
 *FNZ(.5*Z1-.5*Z2)^2+FNZ(Z1)*FNZ(Z1-Z2)
 *(-2*Z1+Z2-2*(1-Z1*(Z1-Z2)))*(Z1-Z2)*FNZ(Z1-Z2)
 -2*Z1*(1-Z1*(Z1-Z2))*FNZ(Z1))
 530 FACT21=-.5*(Z1+Z2)*FNZ(.5*Z1+.5*Z2)^2-.5*(Z2-Z1)
 *FNZ(.5*Z2-.5*Z1)^2+FNZ(Z2)*FNZ(Z2-Z1)
 *(-2*Z2+Z1-2*(1-Z2*(Z2-Z1)))*(Z2-Z1)*FNZ(Z2-Z1)
 -2*Z2*(1-Z2*(Z2-Z1))*FNZ(Z2))
 540 FACT12=-FNZ(Z1-Z2)*(Z1-Z2)*FNZ(.5*Z1-.5*Z2)
 (.5(1-.5*(Z1-Z2)^2)*FNZ(.5*Z1-.5*Z2)
 +2*(1-.5*(Z1-Z2)^2)*FNZ(Z1-Z2)+1)
 550 FACT22=-FNZ(Z2-Z1)*(Z2-Z1)*FNZ(.5*Z2-.5*Z1)
 (.5(1-.5*(Z2-Z1)^2)*FNZ(.5*Z2-.5*Z1)
 +2*(1-.5*(Z2-Z1)^2)*FNZ(Z2-Z1)+1)
 560 FACT13=-.5*(Z1+Z2)*FNZ(.5*Z1+.5*Z2)^2+.5*(Z1-Z2)
 *FNZ(.5*Z1-.5*Z2)^2+FNZ(Z1)*FNZ(Z1-Z2)
 (Z1+2(Z1-Z2)*(1-Z1*(Z1-Z2))*FNZ(Z1-Z2))
 570 FACT23=-.5*(Z1+Z2)*FNZ(.5*Z1+.5*Z2)^2+.5*(Z2-Z1)
 *FNZ(.5*Z2-.5*Z1)^2+FNZ(Z2)*FNZ(Z2-Z1)
 (Z2+2(Z2-Z1)*(1-Z2*(Z2-Z1))*FNZ(Z2-Z1))
 580 FACT14=(Z1-Z2)*FNZ(Z1-Z2)*FNZ(.5*Z1-.5*Z2)
 (.5(1-.5*(Z1-Z2)^2)*FNZ(.5*Z1-.5*Z2)
 +2*(1-.5*(Z1-Z2)^2)*FNZ(Z1-Z2)+1)
 590 FACT24=(Z2-Z1)*FNZ(Z2-Z1)*FNZ(.5*Z2-.5*Z1)
 (.5(1-.5*(Z2-Z1)^2)*FNZ(.5*Z2-.5*Z1)
 +2*(1-.5*(Z2-Z1)^2)*FNZ(Z2-Z1)+1)
 600 FACT31=-.5*(Z1+Z2)^2*FNZ(.5*Z1+.5*Z2)^2
 +FNZ(.5*Z1+.5*Z2)*.5*(Z1-Z2)^2
 *FNZ(.5*Z1-.5*Z2)^2+FNZ(.5*Z1-.5*Z2)
 610 FACT41=-.5*(Z1+Z2)^2*FNZ(.5*Z1+.5*Z2)^2
 +FNZ(.5*Z1+.5*Z2)*.5*(Z2-Z1)^2
 *FNZ(.5*Z2-.5*Z1)^2+FNZ(.5*Z2-.5*Z1)
 620 FACT32=FNZ(Z1-Z2)*FNZ(Z1)*(Z1*(8*Z1-4*Z2)
 *FNZ(Z1)+(8*Z1-4*Z2)*(Z1-Z2)*FNZ(Z1-Z2)-4)
 630 FACT42=FNZ(Z2-Z1)*FNZ(Z2)*(Z2*(8*Z2-4*Z1)

```

      *FNZ(Z2)+(8*Z2-4*Z1)*(Z2-Z1)*FNZ(Z2-Z1)-4)
640 FACT33=3*FNZ(Z1-Z2)*FNZ(.5*Z1-.5*Z2)*(.5*(Z1-Z2)^2
      *FNZ(.5*Z1-.5*Z2)+2*(Z1-Z2)^2*FNZ(Z1-Z2)-1)
650 FACT43=3*FNZ(Z2-Z1)*FNZ(.5*Z2-.5*Z1)*(.5*(Z2-Z1)^2
      *FNZ(.5*Z2-.5*Z1)+2*(Z2-Z1)^2*FNZ(Z2-Z1)-1)
660 FACT34=-.5*(Z1+Z2)^2*FNZ(.5*Z1+.5*Z2)^2
      +FNZ(.5*Z1+.5*Z2)+.5*(Z1-Z2)^2
      *FNZ(.5*Z1-.5*Z2)^2-FNZ(.5*Z1-.5*Z2)
670 FACT44=-.5*(Z1+Z2)^2*FNZ(.5*Z1+.5*Z2)^2
      +FNZ(.5*Z1+.5*Z2)+.5*(Z2-Z1)^2
      *FNZ(.5*Z2-.5*Z1)^2-FNZ(.5*Z2-.5*Z1)
680 FACT35=FNZ(Z1)*FNZ(Z1-Z2)*(-(8*Z1-4*Z2)*(Z1-Z2)
      *FNZ(Z1-Z2)+2)
690 FACT45=FNZ(Z2)*FNZ(Z2-Z1)*(-(8*Z2-4*Z1)*(Z2-Z1)
      *FNZ(Z2-Z1)+2)
700 FACT36=-3*FNZ(Z1-Z2)*FNZ(.5*Z1-.5*Z2)*(.5*(Z1-Z2)^2
      *FNZ(.5*Z1-.5*Z2)+2*(Z1-Z2)^2*FNZ(Z1-Z2)-1)
710 FACT46=-3*FNZ(Z2-Z1)*FNZ(.5*Z2-.5*Z1)*(.5*(Z2-Z1)^2
      *FNZ(.5*Z2-.5*Z1)+2*(Z2-Z1)^2*FNZ(Z2-Z1)-1)
720 NWT1=2*(MT*MR*I2*I4)^.5*(COS(Psi)*(1-SF42^2)^.5
      -SF42*SIN(Psi))
730 NWT2=2*(MT*MR*I1*I3)^.5*(COS(Psi)*(1-SF31^2)^.5
      -SF31*SIN(Psi))
740 NWT3=2*(MT*MR*I2*I4)^.5*(COS(Psi)*(1-SF42^2)^.5
      +SF42*SIN(Psi))
750 NWT4=2*(MT*MR*I1*I3)^.5*(COS(Psi)*(1-SF31^2)^.5
      +SF31*SIN(Psi))

```

The next section defines the Jacobian, $J(i, j)$, and the equation vector $F(i)$.

```

760 F(1)=F11*FNE(Z1)-F21-F11*I1*(1+FNZ(Z1))
      -F11*(MR*I2+MT*I4+NWT1)*FACT1+M1*(I3/I1)^.5
      *(COS(Psi)*(1-SF31^2)^.5-SIN(Psi)*SF31)
770 F(2)=F11*FNE(Z2)-F21-F11*I2*(1+FNZ(Z2))
      -F11*(MR*I1+MT*I3+NWT2)*FACT2+M1*(I4/I2)^.5
      *(COS(Psi)*(1-SF42^2)^.5-SIN(Psi)*SF42)
780 F(3)=F12*FNE(Z1)-F22-F12*I3*(1+FNZ(Z1))
      -F12*(MR*I4+MT*I2+NWT3)*FACT1+M2*(I1/I3)^.5
      *(COS(Psi)*(1-SF31^2)^.5+SIN(Psi)*SF31)
790 F(4)=F12*FNE(Z2)-F22-F12*I4*(1+FNZ(Z2))
      -F12*(MR*I3+MT*I1+NWT4)*FACT2+M2*(I2/I4)^.5
      *(COS(Psi)*(1-SF42^2)^.5+SIN(Psi)*SF42)
800 F(5)=Z1-(D1+FSR)+2*F11*FNE(Z1)*NT1-F11*I1*Z1*FNZ(Z1)
      -.5*F11*(MR*I2+MT*I4+NWT1)*FACT3+M1*(I3/I1)^.5
      *(SF31*COS(Psi)+SIN(Psi)*(1-SF31^2)^.5)
810 F(6)=Z2-(D1+FSR)+2*F11*FNE(Z2)*NT2-F11*I2*Z2*FNZ(Z2)

```

$$-.5 * F11 * (MR * I1 + MT * I3 + NWT2) * FACT1 + M1 * (I4 / I2) ^ .5$$

$$* (SF42 * COS(Psi) + SIN(Psi) * (1 - SF42 ^ 2) ^ .5)$$
820
$$F(7) = Z1 - (D2 + FSR) + 2 * F12 * FNE(Z1) * NT1 - F12 * I3 * Z1 * FNZ(Z1)$$

$$-.5 * F12 * (MR * I4 + MT * I2 + NWT3) * FACT3 - M2 * (I1 / I3) ^ .5$$

$$* (SF31 * COS(Psi) - SIN(Psi) * (1 - SF31 ^ 2) ^ .5)$$
830
$$F(8) = Z2 - (D2 + FSR) + 2 * F12 * FNE(Z2) * NT2 - F12 * I4 * Z2 * FNZ(Z2)$$

$$-.5 * F12 * (MR * I3 + MT * I1 + NWT4) * FACT4 - M2 * (I2 / I4) ^ .5$$

$$* (SF42 * COS(Psi) - SIN(Psi) * (1 - SF42 ^ 2) ^ .5)$$
840
$$J(1,1) = -F11 * (1 + FNZ(Z1)) - .5 * M1 * (I3 / I1) ^ .5 * (1 / I1)$$

$$* (COS(Psi) * (1 - SF31 ^ 2) ^ .5 - SIN(Psi) * SF31)$$
850
$$J(1,2) = -F11 * FACT1 * (MR + (MT * MR * I4 / I2) ^ .5 * (COS(Psi)$$

$$* (1 - SF42 ^ 2) ^ .5 - SF42 * SIN(Psi)))$$
860
$$J(1,3) = .5 * M1 * (I1 * I3) ^ -.5 * (COS(Psi) * (1 - SF31 ^ 2) ^ .5$$

$$- SIN(Psi) * SF31)$$
870
$$J(1,4) = -F11 * FACT1 * (MT + (MT * MR * I2 / I4) ^ .5 * (COS(Psi)$$

$$* (1 - SF42 ^ 2) ^ .5 - SF42 * SIN(Psi)))$$
880
$$J(1,5) = -2 * F11 * G ^ 2 * FNE(Z1) + 2 * F11 * I1 * Z1 * FNZ(Z1)$$

$$- F11 * (MR * I2 + MT * I4 + NWT1) * (FACT11 + FACT12)$$
890
$$J(1,6) = -F11 * (MR * I2 + MT * I4 + NWT1) * (FACT13 + FACT14)$$
900
$$J(1,7) = -M1 * (I3 / I1) ^ .5 * (COS(Psi) * SF31 * (1 - SF31 ^ 2) ^ -.5$$

$$+ SIN(Psi))$$
910
$$J(1,8) = F11 * FACT1 * 2 * (MT * MR * I2 * I4) ^ .5 * (COS(Psi)$$

$$* SF42 * (1 - SF42 ^ 2) ^ -.5 + SIN(Psi))$$
920
$$J(2,1) = -F11 * FACT2 * (MR + (MT * MR * I3 / I1) ^ .5 * (COS(Psi)$$

$$* (1 - SF31 ^ 2) ^ .5 - SF31 * SIN(Psi)))$$
930
$$J(2,2) = -F11 * (1 + FNZ(Z2)) - .5 * M1 * (I4 / I2) ^ .5 * (1 / I2)$$

$$* (COS(Psi) * (1 - SF42 ^ 2) ^ .5 - SIN(Psi) * SF42)$$
940
$$J(2,3) = -F11 * FACT2 * (MT + (MT * MR * I1 / I3) ^ .5 * (COS(Psi)$$

$$* (1 - SF31 ^ 2) ^ .5 - SF31 * SIN(Psi)))$$
950
$$J(2,4) = .5 * M1 * (I2 * I4) ^ -.5 * (COS(Psi) * (1 - SF42 ^ 2) ^ .5$$

$$- SIN(Psi) * SF42)$$
960
$$J(2,5) = -F11 * (MR * I1 + MT * I3 + NWT2) * (FACT23 + FACT24)$$
970
$$J(2,6) = -2 * F11 * G ^ 2 * FNE(Z2) + 2 * F11 * I2 * Z2 * FNZ(Z2)$$

$$- F11 * (MR * I1 + MT * I3 + NWT2) * (FACT21 + FACT22)$$
980
$$J(2,7) = F11 * FACT2 * 2 * (MT * MR * I1 * I3) ^ .5 * (COS(Psi)$$

$$* SF31 * (1 - SF31 ^ 2) ^ -.5 + SIN(Psi))$$
990
$$J(2,8) = -M1 * (I4 / I2) ^ .5 * (COS(Psi) * SF42 * (1 - SF42 ^ 2) ^ -.5$$

$$+ SIN(Psi))$$
1000
$$J(3,1) = .5 * M2 * (I1 * I3) ^ -.5 * (COS(Psi) * (1 - SF31 ^ 2) ^ .5$$

$$+ SIN(Psi) * SF31)$$
1010
$$J(3,2) = -F12 * FACT1 * (MT + (MT * MR * I4 / I2) ^ .5 * (COS(Psi)$$

$$* (1 - SF42 ^ 2) ^ .5 + SF42 * SIN(Psi)))$$
1020
$$J(3,3) = -F12 * (1 + FNZ(Z1)) - .5 * M2 * (I1 / I3) ^ .5 * (1 / I3)$$

$$* (COS(Psi) * (1 - SF31 ^ 2) ^ .5 + SIN(Psi) * SF31)$$
1030
$$J(3,4) = -F12 * FACT1 * (MR + (MT * MR * I2 / I4) ^ .5 * (COS(Psi)$$

$$* (1 - SF42 ^ 2) ^ .5 + SF42 * SIN(Psi)))$$
1040
$$J(3,5) = -2 * F12 * G ^ 2 * FNE(Z1) + 2 * F12 * I3 * Z1 * FNZ(Z1)$$

$$-F12*(MR*I4+MT*I2+NWT3)*(FACT11+FACT12)$$
1050 J(3,6)=-F12*(MR*I4+MT*I2+NWT3)*(FACT13+FACT14)
1060 J(3,7)=-M2*(I1/I3)^.5*(COS(PSI)*SF31*(1-SF31^2)^-.5
-SIN(PSI))
1070 J(3,8)=-F12*FACT1*2*(MT*MR*I2*I4)^.5*(-COS(PSI)
SF42(1-SF42^2)^-.5+SIN(PSI))
1080 J(4,1)=-F12*FACT2*(MT+(MT*MR*I3/I1)^.5*(COS(PSI)
*(1-SF31^2)^.5+SF31*SIN(PSI)))
1090 J(4,2)=.5*M2*(I2*I4)^-.5*(COS(PSI)*(1-SF42^2)^.5
+SIN(PSI)*SF42)
1100 J(4,3)=-F12*FACT2*(MR+(MT*MR*I1/I3)^.5*(COS(PSI)
*(1-SF31^2)^.5+SF31*SIN(PSI)))
1110 J(4,4)=-F12*(1+FNZ(Z2))-.5*M2*(I2/I4)^.5*(1/I4)
(COS(PSI)(1-SF42^2)^.5+SIN(PSI)*SF42)
1120 J(4,5)=-F12*(MR*I3+MT*I1+NWT4)*(FACT23+FACT24)
1130 J(4,6)=-2*F12*G^2*FNE(Z2)+2*F12*I4*Z2*FNZ(Z2)
-F12*(MR*I3+MT*I1+NWT4)*(FACT21+FACT22)
1140 J(4,7)=-F12*FACT2*2*(MT*MR*I1*I3)^.5*(-COS(PSI)
SF31(1-SF31^2)^-.5+SIN(PSI))
1150 J(4,8)=-M2*(I2/I4)^.5*(COS(PSI)*SF42*(1-SF42^2)^-.5
-SIN(PSI))
1160 J(5,1)=-F11*Z1*FNZ(Z1)-.5*M1*(I3/I1)^.5*(1/I1)
*(SF31*COS(PSI)+SIN(PSI)*(1-SF31^2)^.5)
1170 J(5,2)=-.5*F11*FACT3*(MR+(MT*MR*I4/I2)^.5*(COS(PSI)
*(1-SF42^2)^.5-SF42*SIN(PSI)))
1180 J(5,3)=.5*M1*(I1*I3)^-.5*(SF31*COS(PSI)+SIN(PSI)
*(1-SF31^2)^.5)
1190 J(5,4)=-.5*F11*FACT3*(MT+(MT*MR*I2/I4)^.5*(COS(PSI)
*(1-SF42^2)^.5-SF42*SIN(PSI)))
1200 J(5,5)=1-4*Z1*G^2*F11*FNE(Z1)*NT1+2*F11*G-F11*I1
*(FNZ(Z1)-2*Z1^2*FNZ(Z1)^2)-.5*F11
*(MR*I2+MT*I4+NWT1)*(FACT31+FACT32+FACT33)
1210 J(5,6)=-.5*F11*(MR*I2+MT*I4+NWT1)*(FACT34+FACT35+FACT36)
1220 J(5,7)=M1*(I3/I1)^.5*(COS(PSI)-SIN(PSI)*SF31
*(1-SF31^2)^-.5)
1230 J(5,8)=F11*FACT3*(MT*MR*I2*I4)^.5*(COS(PSI)*SF42
*(1-SF42^2)^-.5+SIN(PSI))
1240 J(6,1)=-.5*F11*FACT4*(MR+(MT*MR*I3/I1)^.5*(COS(PSI)
*(1-SF31^2)^.5-SF31*SIN(PSI)))
1250 J(6,2)=-F11*Z2*FNZ(Z2)-.5*M1*(I4/I2)^.5*(1/I2)
*(SF42*COS(PSI)+SIN(PSI)*(1-SF42^2)^.5)
1260 J(6,3)=-.5*F11*FACT4*(MT+(MT*MR*I1/I3)^.5*(COS(PSI)
*(1-SF31^2)^.5-SF31*SIN(PSI)))
1270 J(6,4)=.5*M1*(I2*I4)^-.5*(SF42*COS(PSI)+SIN(PSI)
*(1-SF42^2)^.5)
1280 J(6,5)=-.5*F11*(MR*I1+MT*I3+NWT2)*(FACT44+FACT45+FACT46)
1290 J(6,6)=1-4*Z2*G^2*F11*FNE(Z2)*NT2+2*F11*G-F11*I2*(FNZ(Z2)

```

-2*Z2^2*FNZ(Z2)^2)-.5*F11*(MR*I1+MT*I3+NWT2)
*(FACT41+FACT42+FACT43)
1300 J(6,7)=F11*FACT4*(MT*MR*I1*I3)^.5*(COS(PSI)*SF31
*(1-SF31^2)^-.5+SIN(PSI))
1310 J(6,8)=M1*(I4/I2)^.5*(COS(PSI)-SIN(PSI)*SF42
*(1-SF42^2)^-.5)
1320 J(7,1)=-.5*M2*(I1*I3)^-.5*(SF31*COS(PSI)-SIN(PSI)
*(1-SF31^2)^.5)
1330 J(7,2)=-.5*F12*FACT3*(MT+(MT*MR*I4/I2)^.5*(COS(PSI)
*(1-SF42^2)^.5+SF42*SIN(PSI)))
1340 J(7,3)=-F12*Z1*FNZ(Z1)+.5*M2*(I1/I3)^.5*(1/I3)
*(SF31*COS(PSI)-SIN(PSI)*(1-SF31^2)^.5)
1350 J(7,4)=-.5*F12*FACT3*(MR+(MR*MT*I2/I4)^.5*(COS(PSI)
*(1-SF42^2)^.5+SF42*SIN(PSI)))
1360 J(7,5)=1-4*Z1^2*F12*FNE(Z1)*NT1+2*F12*G-F12
*I3*(FNZ(Z1)-2*Z1^2*FNZ(Z1)^2)-.5*F12
*(MR*I4+MT*I2+NWT3)*(FACT31+FACT32+FACT33)
1370 J(7,6)=-.5*F12*(MR*I4+MT*I2+NWT3)*(FACT34+FACT35+FACT36)
1380 J(7,7)=-M2*(I1/I3)^.5*(COS(PSI)+SIN(PSI)*SF31
*(1-SF31^2)^-.5)
1390 J(7,8)=-F12*FACT3*(MT*MR*I2*I4)^.5*(-COS(PSI)*SF42
*(1-SF42^2)^-.5+SIN(PSI))
1400 J(8,1)=-.5*F12*FACT4*(MT+(MT*MR*I3/I1)^.5*(COS(PSI)
*(1-SF31^2)^.5+SF31*SIN(PSI)))
1410 J(8,2)=-.5*M2*(I2*I4)^-.5*(SF42*COS(PSI)-SIN(PSI)
*(1-SF42^2)^.5)
1420 J(8,3)=-.5*F12*FACT4*(MR+(MT*MR*I1/I3)^.5*(COS(PSI)
*(1-SF31^2)^.5+SF31*SIN(PSI)))
1430 J(8,4)=-F12*Z2*FNZ(Z2)+.5*M2*(I2/I4)^.5*(1/I4)
*(SF42*COS(PSI)-SIN(PSI)*(1-SF42^2)^.5)
1440 J(8,5)=-.5*F12*(MR*I3+MT*I1+NWT4)*(FACT44+FACT45+FACT46)
1450 J(8,6)=1-4*Z2^2*F12*FNE(Z2)*NT2+2*F12*G-F12*I4
*(FNZ(Z2)-2*Z2^2*FNZ(Z2)^2)-.5*F12
*(MR*I3+MT*I1+NWT4)*(FACT41+FACT42+FACT43)
1460 J(8,7)=-F12*FACT4*(MT*MR*I1*I3)^.5*(-COS(PSI)*SF31
*(1-SF31^2)^-.5+SIN(PSI))
1470 J(8,8)=-M2*(I2/I4)^.5*(COS(PSI)+SIN(PSI)*SF42
*(1-SF42^2)^-.5)

```

The Newton-Raphson method is used again to solve for a self consistent solution.

```

1480 IF K > 100 THEN 4430
1490 FOR R = 1 TO N
1500 FOR Q = 1 TO N
1510 A(R,Q) = J(R,Q)
1520 NEXT Q

```

```

1530 A(R,N + 1) = F(R)
1540 NEXT R
1550 FOR I = 1 TO N-1
1560 FOR J = I+1 TO N
1570 M(J,I) = A(J,I)/A(I,I)
1580 FOR Q = 1 TO N+1
1590 A(J,Q) = A(J,Q)-M(J,I)*A(I,Q)
1600 NEXT Q
1610 NEXT J
1620 NEXT I
1630 Y(N) = A(N,N+1)/A(N,N)
1640 FOR I = N-1 TO 1 STEP -1
1650 FOR J = I+1 TO N
1660 PP = PP + A(I,J) * Y(J)
1670 NEXT J
1680 Y(I) = (A(I,N+1)-PP)/A(I,I)
1690 PP = 0
1700 NEXT I
1710 FOR I = 1 TO N
1720 X(I) = X(I) - Y(I)
1730 NEXT I
1740 MAX = 0.
1750 FOR I = 1 TO N
1760 IF ABS(Y(I)) <= MAX THEN 1780
1770 MAX = ABS(Y(I))
1780 NEXT I
1790 IF MAX < TOL THEN 1820
1800 K = K + 1
1810 GOTO 360
1820 PRINT "THE FREQUENCY OFFSET IS "; COUNT
1830 PRINT
1840 PRINT "THE SOLUTION VECTOR IS "
1850 FOR I = 1 TO N
1860 PRINT "X("; I; ") = "; X(I)
1870 NEXT I
1880 PRINT
1890 PRINT "THE INTENSITY SUM IS "; X(1) + X(2)
1900 PRINT

```

The remainder of the program checks each solution for stability. Lines 1910-2280 input the perturbation matrix (A.26) which then undergoes a balancing operation (2290-2660) is reduced to an upper Hessenberg matrix (2670-3060), and then the eigenvalues for the upper Hessenberg matrix are determined and printed (3070-

4440). (For complete details of the matrix manipulations using a QR algorithm, consult *Numerical Recipes* pages 366-376 ²⁷.)

```

1910 PHI31=ATN(SF31/((1-SF31^2)^.5))
1920 PHI42=ATN(SF42/((1-SF42^2)^.5))
1930 B(1,1)=SG*(F11*FNE(Z1)-F21-3*I1*F11
      *(1+FNZ(Z1))-F11*(MR*I2+MT*I4+NWT1)*FACT1)
1940 B(1,2)=-2*I1^.5*SG*F11*FACT1*(MR*I2^.5
      +(MR*MT*I4)^.5*COS(PHI42+PSI))
1950 B(1,3)=SG*M1*COS(PHI31+PSI)
1960 B(1,4)=-2*I1^.5*SG*F11*FACT1*(MT*I4^.5
      +(MR*MT*I2)^.5*COS(PHI42+PSI))
1970 B(1,5)=-SG*M1*I3^.5*SIN(PHI31+PSI)
1980 B(1,6)=-2*F11*SG*FACT1*(I1*I2*I4*MR*MT)^.5
      *SIN(PHI42+PSI)
1990 B(2,1)=-2*I2^.5*SG*F11*FACT2*(MR*I1^.5+(MR*MT*I3)^.5
      *COS(PHI31+PSI))
2000 B(2,2)=SG*(F11*FNE(Z2)-F21-3*I2*F11*(1+FNZ(Z2))
      -F11*(MR*I1+MT*I3+NWT2)*FACT2)
2010 B(2,3)=-2*I3^.5*SG*F11*FACT2*(MT*I3^.5+(MR*MT*I1)^.5
      *COS(PHI31+PSI))
2020 B(2,4)=M1*SG*COS(PHI42+PSI)
2030 B(2,5)=-2*F11*FACT2*SG*(I2*I1*I3*MR*MT)^.5
      *SIN(PHI31+PSI)
2040 B(2,6)=-M1*SG*I4^.5*SIN(PHI42+PSI)
2050 B(3,1)=SG*M2*COS(PHI31-PSI)
2060 B(3,2)=-2*I3^.5*SG*F12*FACT1*(MT*I2^.5+(MR*MT*I4)^.5
      *COS(PHI42-PSI))
2070 B(3,3)=SG*(F12*FNE(Z1)-F22-3*I3*F12*(1+FNZ(Z1))
      -F12*(MR*I4+MT*I2+NWT3)*FACT1)
2080 B(3,4)=-2*I3^.5*SG*F12*FACT1*(MR*I4^.5+(MR*MT*I2)^.5
      *COS(PHI42-PSI))
2090 B(3,5)=-M2*SG*I1^.5*SIN(PHI31-PSI)
2100 B(3,6)=2*SG*F12*FACT1*(MR*MT*I3*I2*I1)^.5
      *SIN(PHI42-PSI)
2110 B(4,1)=-2*I4^.5*SG*F12*FACT2*(MT*I1^.5+(MR*MT*I3)^.5
      *COS(PHI31-PSI))
2120 B(4,2)=M2*SG*COS(PHI42-PSI)
2130 B(4,3)=-2*I4^.5*SG*F12*FACT2*(MR*I3^.5+(MR*MT*I1)^.5
      *COS(PHI31-PSI))
2140 B(4,4)=SG*(F12*FNE(Z2)-F22-3*I4*F12*(1+FNZ(Z2))
      -F12*(MR*I3+MT*I1+NWT4)*FACT2)
2150 B(4,5)=2*SG*F12*FACT2*(MR*MT*I4*I1*I3)^.5
      *SIN(PHI31-PSI)
2160 B(4,6)=-M2*SG*I2^.5*SIN(PHI42-PSI)

```

```

2170 B(5,1)=SG*(2*F11*I1^.5*Z1*FNZ(Z1)-(M2/I3^.5)
      *SIN(PHI31-PSI)+(M1/I1)*I3^.5*SIN(PHI31+PSI))
2180 B(5,2)=2*F11*SG*FACT3*((MR*I2^.5+(MR*MT*I4)^.5
      *COS(PHI42+PSI))-(MT*I2^.5+(MR*MT*I4)^.5
      *COS(PHI42-PSI)))
2190 B(5,3)=SG*(-2*F11*I3^.5*Z1*FNZ(Z1)+(M2/I3)*I1^.5
      *SIN(PHI31-PSI)-(M1/I1^.5)*SIN(PHI31+PSI))
2200 B(5,4)=2*F11*SG*FACT3*((MT*I4^.5+(MT*MR*I2)^.5
      *COS(PHI42+PSI))-(MR*I4^.5+(MT*MR*I2)^.5
      *COS(PHI42-PSI)))
2210 B(5,5)=-SG*(M2*(I1/I3)^.5*COS(PHI31-PSI)+M1*(I3/I1)^.5
      *COS(PHI31+PSI))
2220 B(5,6)=-4*SG*F11*FACT3*(MR*MT*I2*I4)^.5
      *SIN(PSI)*COS(PHI42)
2230 B(6,1)=2*F12*SG*FACT4*((MR*I1^.5+(MR*MT*I3)^.5
      *COS(PHI31+PSI))-(MT*I1^.5+(MR*MT*I3)^.5
      *COS(PHI31-PSI)))
2240 B(6,2)=SG*(2*F12*I2^.5*Z2*FNZ(Z2)-(M2/I4^.5)
      *SIN(PHI42-PSI)+(M1/I2)*(I4^.5)
      *SIN(PHI42+PSI))
2250 B(6,3)=2*F12*SG*FACT4*((MT*I3^.5+(MT*MR*I1)^.5
      *COS(PHI31+PSI))-(MR*I3^.5+(MT*MR*I1)^.5
      *COS(PHI31-PSI)))
2260 B(6,4)=SG*(-2*F12*I4^.5*Z2*FNZ(Z2)+(M2/I4)*I2^.5
      *SIN(PHI42-PSI)-(M1/I2)*SIN(PHI42+PSI))
2270 B(6,5)=-4*SG*F12*FACT4*(MR*MT*I1*I3)^.5
      *SIN(PSI)*COS(PHI31)
2280 B(6,6)=-SG*(M2*(I2/I4)^.5*COS(PHI42-PSI)+M1*(I4/I2)^.5
      *COS(PHI42+PSI))
2290 LAST = 1
2300 FOR I=1 TO 6
2310 C = 0
2320 R = 0
2330 FOR J=1 TO 6
2340 IF J<>I THEN
2350 C = C+ABS(B(J,I))
2360 R = R+ABS(B(I,J))
2370 END IF
2380 NEXT J
2390 IF C<>0 AND R<>0 THEN
2400 GG = R/2
2410 F = 1
2420 S = C+R
2430 IF C<GG THEN
2440 F = F*2
2450 C = C*4
2460 GOTO 2430

```

```

2470 END IF
2480 GG = R*2
2490 IF C>GG THEN
2500 F = F/2
2510 C = C/4
2520 GOTO 2490
2530 END IF
2540 IF (C+R)/F<.95*S THEN
2550 LAST = 0
2560 GG = 1/F
2570 FOR J=1 TO 6
2580 B(I,J)=B(I,J)*GG
2590 NEXT J
2600 FOR J = 1 TO 6
2610 B(J,I)=B(J,I)*F
2620 NEXT J
2630 END IF
2640 END IF
2650 NEXT I
2660 IF LAST=0 THEN 2290
2670 CN = 6
2680 IF CN>2 THEN
2690 FOR M=2 TO CN-1
2700 X = 0
2710 I = M
2720 FOR J=M TO CN
2730 IF ABS(B(J,M-1))>ABS(X) THEN
2740 X = B(J,M-1)
2750 I = J
2760 END IF
2770 NEXT J
2780 IF I<>M THEN
2790 FOR J=M-1 TO CN
2800 Y = B(I,J)
2810 B(I,J)=B(M,J)
2820 B(M,J)=Y
2830 NEXT J
2840 FOR J=1 TO CN
2850 Y = B(J,I)
2860 B(J,I)=B(J,M)
2870 B(J,M)=Y
2880 NEXT J
2890 END IF
2900 IF X<>0 THEN
2910 FOR I=M+1 TO CN
2920 Y = B(I,M-1)
2930 IF Y<>0 THEN

```

```

2940 Y = Y/X
2950 B(I,M-1)=Y
2960 FOR J=M TO CN
2970 B(I,J)=B(I,J)-Y*B(M,J)
2980 NEXT J
2990 FOR J=1 TO CN
3000 B(J,M)=B(J,M)+Y*B(J,I)
3010 NEXT J
3020 END IF
3030 NEXT I
3040 END IF
3050 NEXT M
3060 END IF
3070 ANORM = ABS(B(1,1))
3080 FOR I=2 TO CN
3090 FOR J=I-1 TO CN
3100 ANORM = ANORM + ABS(B(I,J))
3110 NEXT J
3120 NEXT I
3130 NN = CN
3140 T = 0
3150 IF NN>1 THEN
3160 ITS = 0
3170 FOR L = NN TO 2 STEP -1
3180 S = ABS(B(L-1,L-1)) + ABS(B(L,L))
3190 IF S=0 THEN S=ANORM
3200 IF ABS(B(L,L-1))+S=S THEN 3230
3210 NEXT L
3220 L = 1
3230 X = B(NN,NN)
3240 IF L = NN THEN
3250 WR(NN) = X+T
3260 WI(NN) = 0
3270 NN = NN-1
3280 ELSE
3290 Y = B(NN-1,NN-1)
3300 W = B(NN,NN-1)*B(NN-1,NN)
3310 IF L = NN-1 THEN
3320 P = .5*(Y-X)
3330 Q = P^2+W
3340 Z = (ABS(Q))^.5
3350 X = X+T
3360 IF Q=0 THEN
3370 IF P>=0 THEN Z=P+ABS(Z)
3380 IF P<=0 THEN Z=P-ABS(Z)
3390 WR(NN) = X+Z
3400 WR(NN-1) = WR(NN)

```

```

3410 IF Z<>0 THEN WR(NN)=X-W/Z
3420 WI(NN) = 0
3430 WI(NN-1) = 0
3440 ELSE
3450 WR(NN) = X+P
3460 WR(NN-1) = WR(NN)
3470 WI(NN) = Z
3480 WI(NN-1) = -Z
3490 END IF
3500 NN = NN-2
3510 ELSE
3520 IF ITS=30 THEN PRINT "NO ROOTS FOUND"
3530 IF ITS=10 OR ITS=20 THEN
3540 T = T+X
3550 FOR I=1 TO NN
3560 B(I,I)=B(I,I)-X
3570 NEXT I
3580 S = ABS(B(NN,NN- ))+ABS(B(NN-1,NN-2))
3590 X = .75*S
3600 Y = X
3610 W = -.4375*S^2
3620 END IF
3630 ITS = ITS+1
3640 FOR M=NN-2 TO L STEP -1
3650 Z = B(M,M)
3660 R = X-Z
3670 S = Y-Z
3680 P = (R*S-W)/B(M+1,M)+B(M,M+1)
3690 Q = B(M+1,M+1)-Z-R-S
3700 R = B(M+2,M+1)
3710 S = ABS(P)+ABS(Q)+ABS(R)
3720 P = P/S
3730 Q = Q/S
3740 R = R/S
3750 IF M=L THEN 3800
3760 U = ABS(B(M,M-1))*(ABS(Q)+ABS(R))
3770 V = ABS(P)*(ABS(B(M-1,M-1))+ABS(Z)+ABS(B(M+1,M+1)))
3780 IF U+V=V THEN 3800
3790 NEXT M
3800 FOR I=M+2 TO NN
3810 B(I,I-2) = 0
3820 IF I<>M+2 THEN B(I,I-3)=0
3830 NEXT I
3840 FOR KK=M TO NN-1
3850 IF KK<>M THEN
3860 P = B(KK,KK-1)
3870 Q = B(KK+1,KK-1)

```

```

3880 R = 0
3890 IF KK <> NN-1 THEN R=B(KK+2,KK-1)
3900 X = ABS(P)+ABS(Q)+ABS(R)
3910 IF X <> 0 THEN
3920 P = P/X
3930 Q = Q/X
3940 R = R/X
3950 END IF
3960 END IF
3970 IF P >= 0 THEN S=ABS((P^2+Q^2+R^2)^.5)
3980 IF P <= 0 THEN S=-ABS((P^2+Q^2+R^2)^.5)
3990 IF S <> 0 THEN
4000 IF KK=M THEN
4010 IF L <> M THEN B(KK,KK-1)=-B(KK,KK-1)
4020 ELSE
4030 B(KK,KK-1)=-S*X
4040 END IF
4050 P = P+S
4060 X = P/S
4070 Y = Q/S
4080 Z = R/S
4090 Q = Q/P
4100 R = R/P
4110 FOR J=KK TO NN
4120 P = B(KK,J)+Q*B(KK+1,J)
4130 IF KK <> NN-1 THEN
4140 P = P+R*B(KK+2,J)
4150 B(KK+2,J)=B(KK+2,J)-P*Z
4160 END IF
4170 B(KK+1,J)=B(KK+1,J)-P*Y
4180 B(KK,J)=B(KK,J)-P*X
4190 NEXT J
4200 IF NN <= KK+3 THEN MIN=NN
4210 IF NN >= KK+3 THEN MIN=KK+3
4220 FOR I=L TO MIN
4230 P = X*B(I,KK)+Y*B(I,KK+1)
4240 IF KK <> NN-1 THEN
4250 P = P+Z*B(I,KK+2)
4260 B(I,KK+2)=B(I,KK+2)-P*R
4270 END IF
4280 B(I,KK+1)=B(I,KK+1)-P*Q
4290 B(I,KK)=B(I,KK)-P
4300 NEXT I
4310 END IF
4320 NEXT KK
4330 GOTO 3170
4340 END IF

```

```
4350 END IF
4360 GOTO 3150
4370 END IF
4380 FOR I=1 TO 6
4390 PRINT "WR("; I; ") = "; WR(I), "WI("; I; ") = "; WI(I)
4400 NEXT I
4410 NEXT COUNT
4420 END
4430 PRINT "EXCEEDED MAXIMUM NUMBER OF STEPS"
4440 END
```

Once the eigenvalues were returned, the signs of the real parts were inspected to determine the extent of the stable operating range.

Appendix B: Experimental Verification of the Mutually-Reinforced Hole-Burning Minimum

This appendix will present the experiment used to verify the existence of the mutually-reinforced hole-burning minimum mentioned in chapter II. In the first section, a brief overview of hole-burning phenomena will be discussed along with the theoretical modelling of a two-mode He-Ne laser. The second part will describe the experimental setup and comment on the results.

A. Spectral Hole Burning Theory

Spectral hole burning in a Doppler-broadened gain profile is a well known phenomenon in gas lasers ³¹. The most famous consequence of hole burning is the "Lamb dip" which Lamb predicted in his treatise on laser theory in 1964 ²⁰. The Lamb dip, which is usually observed using a single (longitudinal) mode laser, represents a small dip at the peak of the relative intensity curve of the laser as it is tuned across a Doppler-broadened gain profile of the medium. Although single mode operation of lasers has been studied thoroughly ²⁰, the case of hole burning by multiple modes oscillating simultaneously does not seem to have received the close attention of previous investigators. When a laser with a Doppler-broadened gain medium oscillates on two longitudinal modes, the relative intensity tuning curve manifests not only the two Lamb dips associated with the two modes oscillating, but also another dip which is somewhat more pronounced than the more familiar Lamb dips.

If a single laser mode oscillates in a standing-wave cavity containing an

inhomogenously-broadened medium, the Doppler frequency shift of the photons travelling in each direction permits the photons to interact generally with two different velocity groups of the laser medium, saturating the gain and "burning holes" at two frequencies in the gain curve (See Figure B.1a). When the laser mode is tuned to the gain center, the two holes burned into the gain curve overlap and produce a measureable reduction in the laser output intensity known as the Lamb dip (Figure B.1b).

When the laser is operated in multimode (longitudinal), however, the laser exhibits, in addition to the Lamb dips due to individual modes, a secondary dip in its intensity curve, which is associated with a mutually reinforced hole burning by different modes. This point can be seen from Figure B.2 which shows the incoherent sum of the individual mode intensities representing the total laser output. This intensity tuning curve was generated by numerically solving the set of four coupled equations obtained for a two-mode He-Ne laser using Lamb's semi-classical laser theory ²⁰:

$$\frac{\partial E_1}{\partial t} = E_1 (\alpha_1 - \beta_1 I_1 - \theta_{12} I_2) \quad (\text{B.1})$$

$$\frac{\partial E_2}{\partial t} = E_2 (\alpha_2 - \beta_2 I_2 - \theta_{21} I_1) \quad (\text{B.2})$$

$$\frac{\partial \phi_1}{\partial t} = \gamma(\xi_1 - \delta - \Delta) + \sigma_1 - \rho_1 I_1 - \tau_{12} I_2 \quad (\text{B.3})$$

$$\frac{\partial \phi_2}{\partial t} = \gamma(\xi_2 + \delta - \Delta) + \sigma_2 - \rho_2 I_2 - \tau_{21} I_1 \quad (\text{B.4})$$

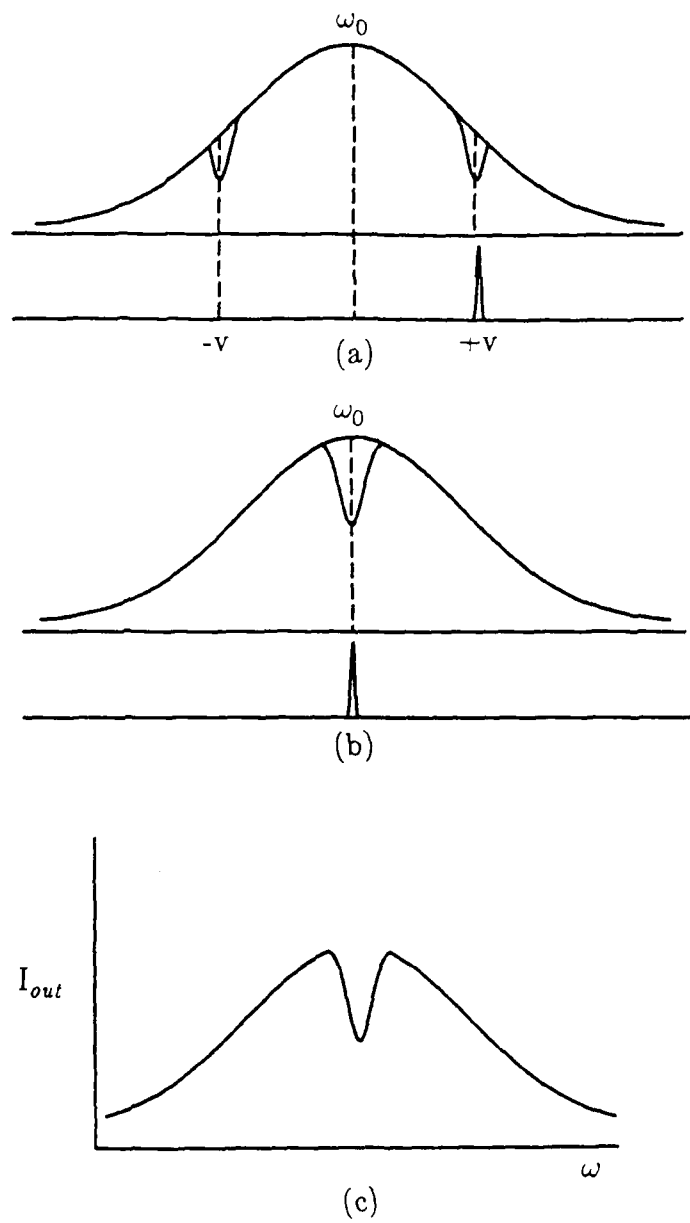


Figure B.1. Spectral hole burning of a Doppler-broadened gain curve: (a) A laser mode oscillating at a frequency away from the gain center burns two holes in the gain curve. (b) A mode oscillating at the gain center burns one hole. (c) The laser output intensity exhibits a Lamb dip as the laser is tuned across the gain curve.

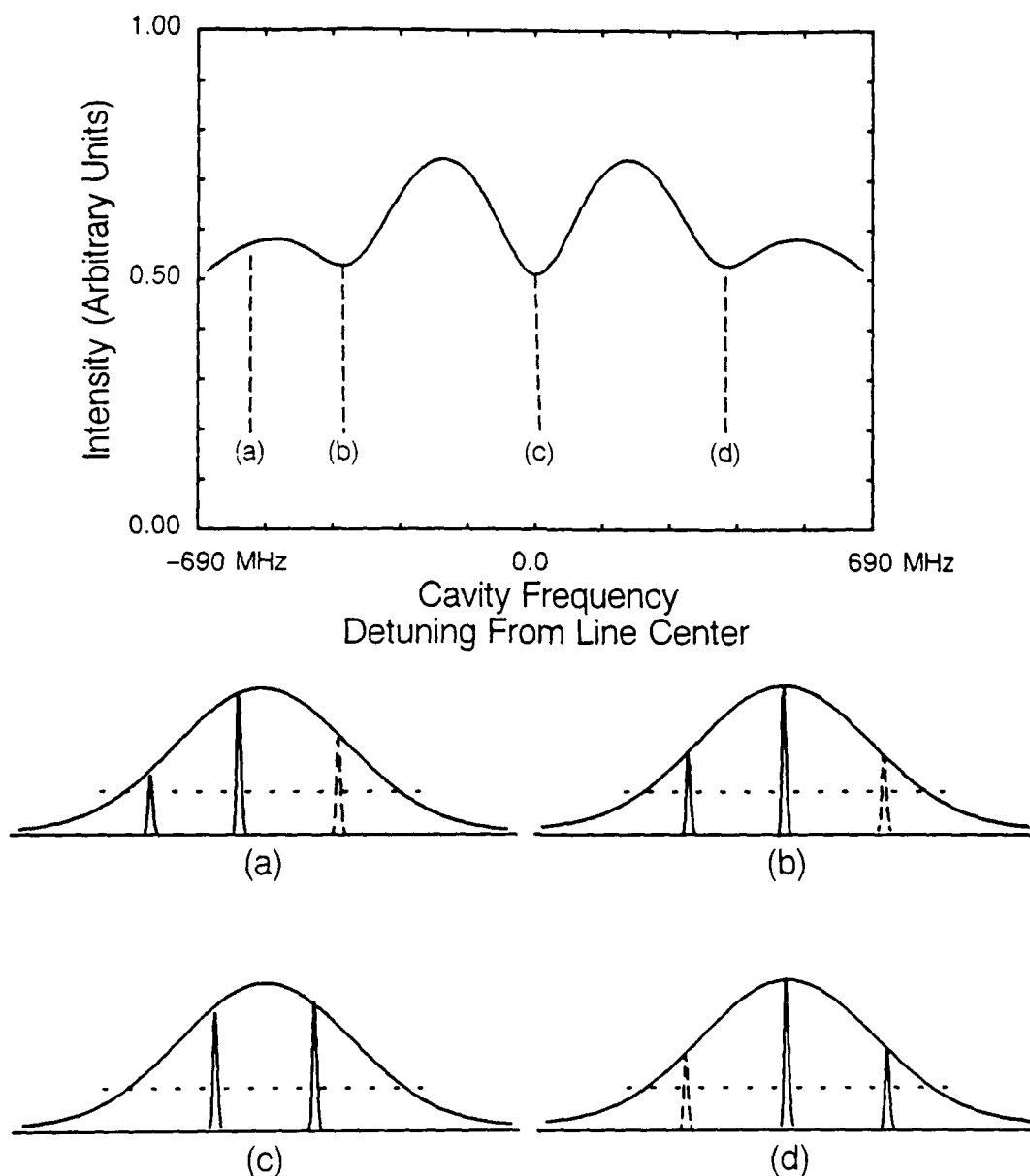


Figure B.2. Intensity tuning curve of a two-mode laser. The intensity shown represents the incoherent sum of the individual mode intensities. The spectral locations of the modes at various points along the tuning curve are shown as (a)-(d).

The coefficients are identical to those found in Table 2.1 and the laser parameters used can be found in Table B.1.

Table B.1: He-Ne Laser Parameters	
Cavity Length	Laser Wavelength
$L = 29 \text{ cm}$	$\lambda = 632.8 \text{ nm}$
Tube Diameter	Doppler Gain Width
$d = 2 \text{ mm}$	$\gamma_d = 1500 \text{ MHz}$
Gain Length	Mirror Reflectivities
$l \approx 14 \text{ cm}$	$R = 0.99 \text{ and } 0.995$
Single-Pass Gain ³²	
$g_0 = .0015 \text{ cm}^{-1}$	

Examination of the frequency detuning of each mode from the gain center frequency reveals the physical process involved. At the position marked (a) in Figure B.2, the two laser modes, split by a free spectral range, appear under the gain profile as shown in Figure B.2a. (The dashed mode in the figure is included for physical accuracy even though the theory does not explicitly treat the three modes. In reality, it is difficult to achieve true two-mode oscillation in a laser as the laser is tuned through several free spectral ranges.) As the cavity is tuned by translating one of the mirrors, the mode frequency at ω_2 reaches the gain center and burns out the Lamb dip at the position marked (b) of Figure B.2. When the

modes are tuned such that they are symmetrically spaced about the line center as shown in Figure B.2c, the holes burned by the mode at ω_1 on each side of the gain center align exactly with the holes burned by the other mode at ω_2 . This overlap of holes burned by the two modes produces an additional intensity minimum at the position marked (c) in a manner analogous to that creating the Lamb dip as shown in Figure B.2c. Continued tuning brings the mode at ω_1 to the line center which, in turn, burns out the second Lamb dip denoted by (d) in Figure B.2. The additional intensity minimum should be present whenever a laser oscillates in multimode and when those modes are symmetrically spaced about the gain center, not just for two modes.

B. Experimental Verification

The existence of the mutually-reinforced hole-burning minimum was demonstrated using an open-cavity He-Ne laser configured to support two longitudinal modes. Figure B.3 shows the schematic diagram of the experimental system used in this experiment with the laser parameters listed in Table B.1. One of the cavity mirrors was mounted on a piezoelectric transducer (PZT) and driven by a signal generator/amplifier generating a sawtooth ramping voltage. To isolate the laser from room air turbulence, the entire cavity was enclosed in a housing. The laser was slowly tuned through several free spectral ranges during which the intensity output through one mirror was detected with a photodetector and sent to a chart recorder. In order to monitor the mode structure, the output from the other mirror was directed into a scanning Fabry-Perot spectrum analyzer.

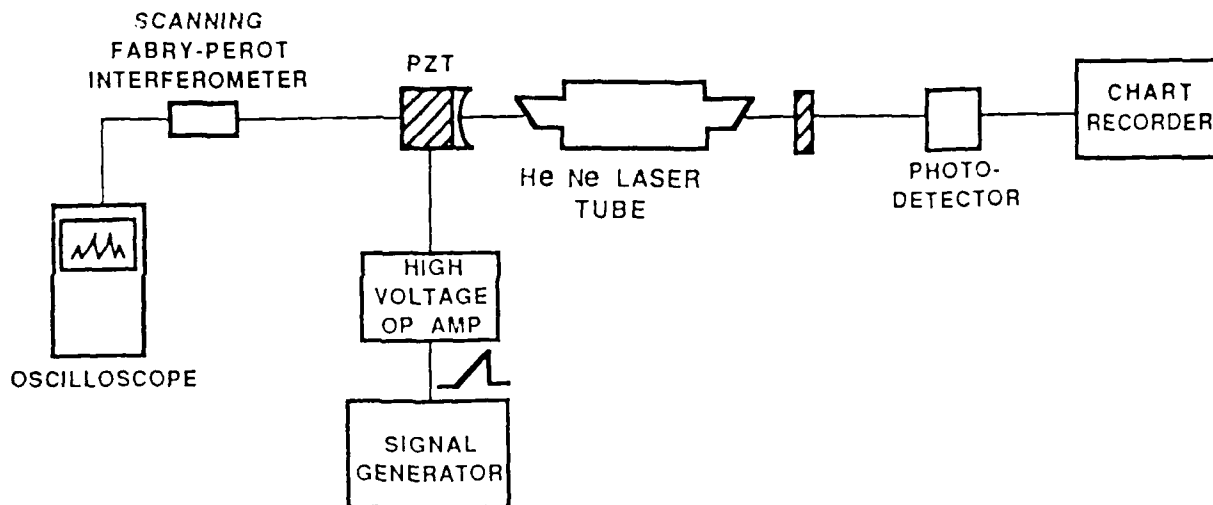


Figure B.3: Schematic diagram of the experimental setup. PZT is a piezoelectric transducer.

Figure B.4 shows the intensity trace from the chart recorder. The deeper valley is the mutually-reinforced hole-burning minimum corresponding to the symmetric placement of the laser modes about the gain center as verified by observing the mode spectrum while the dip occurred. The smaller valley is the Lamb dip whose width (FWHM) was measured to be approximately 130 MHz which is in rough agreement with the theoretical value of the power broadened linewidth. Note the absence of the second Lamb dip which should have appeared as the second mode crossed the gain center. In a real laser, an infinite string of longitudinal modes exists. As a mode on one side of the gain curve is tuned beyond the lasing region, the next mode on the other side of the gain curve enters the lasing region and begins to lase. Unlike the behavior of a real laser, the theory does not account for the replacement of the first mode as it passes out of the gain region. Pictured in Figure B.4 is the reinforced hole-burning minimum and a Lamb dip,

but as tuning progresses, a new mode begins to lase causing the intensity to increase and smear out the second Lamb dip which is predicted by the two-mode theory.

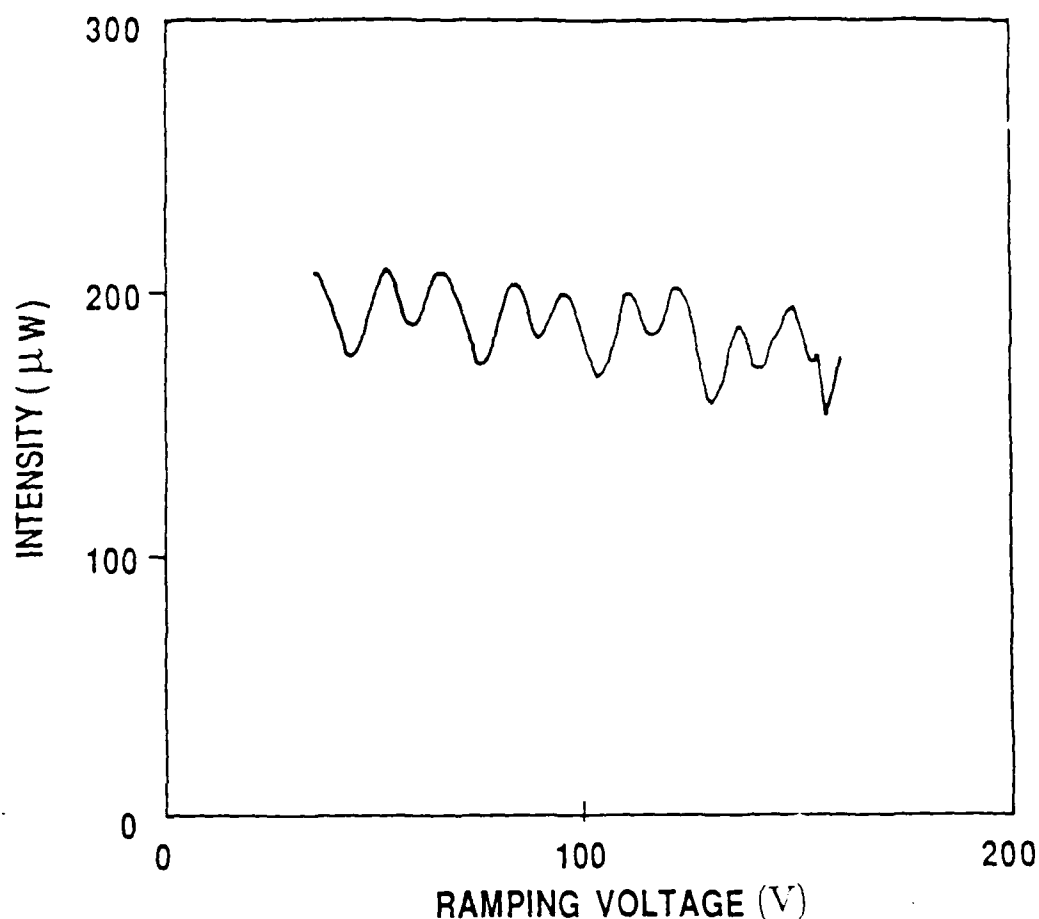


Figure B.4: Recorder trace of the photodetector output exhibiting the mutually-reinforced hole-burning minimum as the PZT-mounted cavity mirror is translated by a ramp signal. See the text for explanation.

Although the theoretical intensity curve shows the multimode dip to be slightly deeper than the Lamb dip, the disparity is much more pronounced in the experimental trace. This is likely due to the difficulty in accurately defining all the parameters used in the theoretical model, especially the single-pass gain and the mirror reflectivities, both of which significantly affect the output intensity.

The qualitative character of the theoretical curve, however, can be seen to be consistent with the experimental observations. As was pointed out, the multimode dip should be observable for any number of modes symmetrically placed about the line center, but the difficulties associated with stabilizing more modes in a longer cavity and the resultant higher amplitude noise precluded its observation.

A laser oscillating in multiple longitudinal modes in a standing-wave cavity containing a Doppler-broadened medium exhibits a dip in the intensity tuning curve in addition to the more familiar Lamb dip. The existence of the dip has been verified both analytically and experimentally. Although many newer theories describing lasers have been developed, this experimental verification shows that Lamb's theoretical model accurately predicts some aspects of the behavior of two-mode as well as single-mode lasers.

Appendix C: Passive Mode Analysis of Three-Mirror Fabry-Perot Resonators

This appendix will examine the mode structure of the three-mirror optical resonator used for the coupled lasers in this dissertation research. Section A presents the field equations describing general three-mirror interferometers. In section B, the conservation-of-energy condition is applied Fabry-Perot interferometers to derive the transmission characteristics and resonant modes for the interferometers acting as a passive filters. The equations are solved for two- and three-mirror resonators to benchmark the theory. In section C, the field equations are solved for the analysis of coupled laser resonators. First, solutions are obtained for the resonant modes and the field distributions for the case of the coupled resonators with a gain medium in only one subcavity. The case of the coupled resonators with a gain medium in each of the two subcavities is studied next. Due to the non-uniqueness that exists in the threshold conditions (*i.e.* , the threshold gains for the two gain media are not uniquely determined by the cavity resonance conditions alone when there are two gain media available in the system), the system is solved for the special case of imposing the condition of equal gains in both subcavities.

A. Field Equations for Three-Mirror Interferometers

In 1986, Van de Stadt and Muller ³³ applied conservation-of-energy boundary conditions which are usually used in the study of multilayer dielectric films to multimirror interferometers to analyze the resonant modes and transmission pro-

perties of such a device. In the treatment, they derived a compact matrix multiplication to model any number of partially reflecting mirrors. While concise and convenient, their analysis is limited in versatility and can only be applied to multi-mirror cavities used as a filter rather than as a laser cavity, since the field distributions within the cavity cannot be evaluated. Also, their theory cannot be used to analyze any two-dimensional resonators such as the Fox-Smith cavity ³⁴. The theory presented in this chapter removes these limitations by generalizing Van de Stadt and Muller's method. The generalization makes it possible to determine the relative intensity of the circulating complex fields at all the partially reflecting mirrors and solves for the resonant modes of the multimirror interferometer and the threshold gain for laser oscillation. The solutions identify the amount of gain needed to sustain steady-state oscillations (threshold gain), the relative strength of the cavity intensities, and the resonance frequencies corresponding to the longitudinal modes of the composite resonators. Knowledge of the the field amplitudes and resonant frequencies should allow experimentalists to tailor their laser cavity configurations to match as closely as possible the conditions necessary to initiate phase locking (*i.e.*, all lasers oscillating on the same frequency with identical phases).

Consider the three-mirror resonator depicted in Figure C.1. Each of the electric fields in the figure (A-G) must satisfy conservation-of-energy requirements. Therefore, the field leaving a mirror in a particular direction is composed of the sum of the waves transmitted through and reflected from the mirror (modified by the appropriate phase shifts and single-pass gains). For example, field E is equal to the transmission of C through mirror (2) after being multiplied by the single-

pass amplitude gain g and delayed by the phase associated with length L_1 , plus the reflected portion of F which encounters the single-pass amplitude gain h while shifted in phase by the optical distance of L_2 and the π phase change upon reflection at mirror (2).

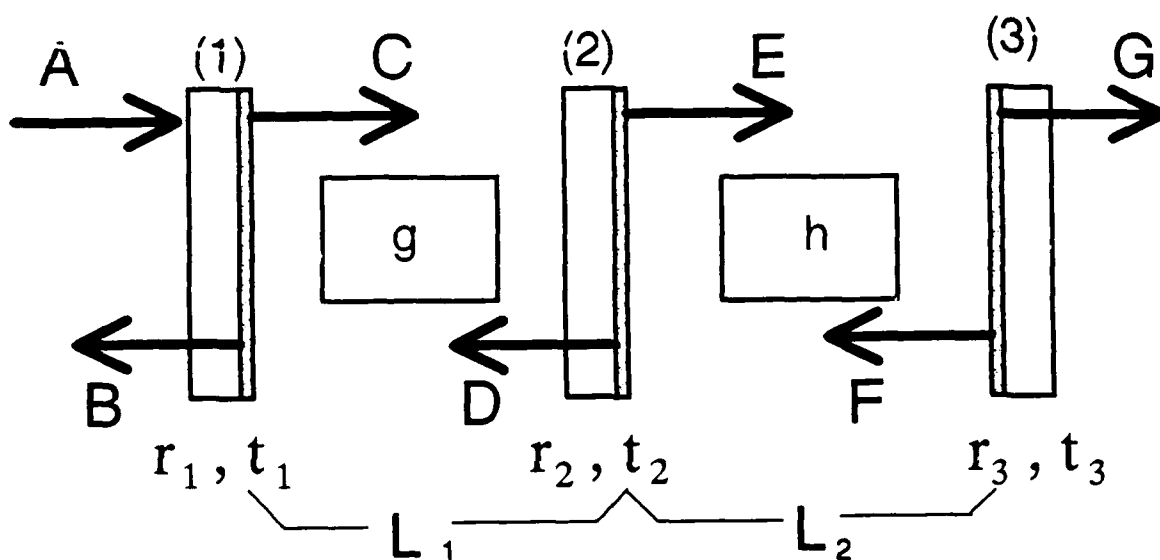


Figure C.1: Fields, phases, mirror reflectivities and transmissivities, and round trip gains for a three mirror cavity.

The optical thicknesses of the mirror substrates are ignored since they can be compensated by adjusting the cavity lengths, but the direction in which the reflective coating on the substrate faces is important because it determines which waves receive an additional π phase change upon reflection off that interface. Claiming to obviate the need for such a distinction, Van de Stadt and Muller embed their reflective surfaces in media with equal refractive indices on both sides thereby eliminating the necessity of tracking the phase changes. That construct is

artificial since there must be different indices on each side of an interface for reflection to occur, but the bookkeeping involved would spoil the symmetry of Van de Stadt and Muller's asthetically pleasing matrix multiplication.

A set of linear equations can be written for each electric field in terms of the others:

$$B = r_1 A + t_1 g D e^{i\delta_1} \quad (\text{C.1.a})$$

$$C = t_1 A + r_1 g D e^{i(\delta_1 + \pi)} \quad (\text{C.1.b})$$

$$D = r_2 g C e^{i\delta_1} + t_2 h F e^{i\delta_2} \quad (\text{C.1.c})$$

$$E = t_2 g C e^{i\delta_1} + r_2 h F e^{i(\delta_2 + \pi)} \quad (\text{C.1.d})$$

$$F = r_3 h E e^{i(\delta_2 + \pi)} \quad (\text{C.1.e})$$

$$G = t_3 h E e^{i\delta_2} \quad (\text{C.1.f})$$

where $\delta_1 = \frac{2\pi}{\lambda} L_1$ and $\delta_2 = \frac{2\pi}{\lambda} L_2$. From this set of six linear equations, a number of different properties of the three-mirror resonator can be determined by instituting the appropriate initial conditions.

B. Application to Filters

The system of equations (C.1.a-f) can be used to analyze the three-mirror interferometer as a passive filter. First, consider the familiar case of the two-mirror Fabry-Perot interferometer which is a limiting case of the three-mirror

Fabry-Perot resonator when $r_2 = 0$ and $g = h = 1.0$. To accomplish this, the system of equations is solved for B and G in terms of A for this situation and the results are:

$$\frac{B}{A} = r_1 - \frac{t_1^2 r_3 e^{i2(\delta_1 + \delta_2)}}{1 - r_1 r_3 e^{i2(\delta_1 + \delta_2)}} \quad (C.2)$$

$$\frac{G}{A} = \frac{t_1 t_3 e^{i2(\delta_1 + \delta_2)}}{1 - r_1 r_3 e^{i2(\delta_1 + \delta_2)}} \quad (C.3)$$

which are readily recognizable as the expressions for the reflection and transmission coefficients of the two mirror Fabry-Perot interferometer normally derived using amplitude splitting summations.

For the case of the passive three-mirror cavity (as a filter), let $g = h = 1.0$.

The solutions are

$$\frac{B}{A} = r_1 - \frac{t_1^2 r_2 e^{i2\delta_1} (1 - r_2 r_3 e^{i2\delta_2}) - t_1^2 t_2^2 r_3 e^{i(2\delta_1 + 2\delta_2)}}{(1 + r_1 r_2 e^{i2\delta_1})(1 - r_2 r_3 e^{i2\delta_2}) - r_1 r_3 t_2^2 e^{i(2\delta_1 + 2\delta_2)}} \quad (C.4)$$

$$\frac{G}{A} = \frac{t_1 t_2 t_3 e^{i(\delta_1 + \delta_2)}}{(1 + r_1 r_2 e^{i2\delta_1})(1 - r_2 r_3 e^{i2\delta_2}) - r_1 r_3 t_2^2 e^{i(2\delta_1 + 2\delta_2)}} \quad (C.5)$$

which collapse to the equations derived by Van de Stadt and Muller when their interfacial phase condition is substituted into the expressions. As required, the intensities of the transmitted and reflected beams are complimentary to each other indicating energy is conserved, but when both outside mirrors have the same reflectivity (mirrors (1) and (3) of Figure C.1), the intensity transmittance of the

resonator (acting as a filter) is governed exclusively by the intensity transmittance of the center mirror. The transmission peaks are spaced at the free spectral range of the super cavity

$$\Delta\nu_{FSR} = \frac{c}{2(L_1 + L_2)} \quad (C.6)$$

Figure C.2 shows the intensity curves for the transmitted and reflected beams with $r_1^2 = r_3^2 = 0.9$, $r_2^2 = 0.5$, and $L_1 = L_2 = 1.0m$. When $L_1 \neq L_2$, a sinusoidal envelope is superimposed on top of the mode structure which further discriminates against selected modes depending on the length mismatch between the two cavities. To achieve an intensity throughput of 1.0, the values of the mirror reflectivities can be manipulated to meet such a requirement. Mirrors of $r_1^2 = 0.6$, $r_2^2 = 0.5$, and $r_3^2 = 0.9$, for example, result in a peak throughput of 0.991. Other filtering characteristics were examined in detail by Van de Stadt and Muller ³³.

C. Application to Coupled Laser Resonators

Despite some fascinating peculiarities of multimirror cavities used as optical filters, of more interest to the laser resonators community are the resonant mode structure and the threshold gain required to sustain a steady-state oscillation for a gain medium placed in the cavity. To build a deeper understanding of the characteristics of three-mirror Fabry-Perot lasers, the system is first examined with a gain medium in only one side of the resonator. Second, the more pertinent case of gain medium in both cavities will be discussed.

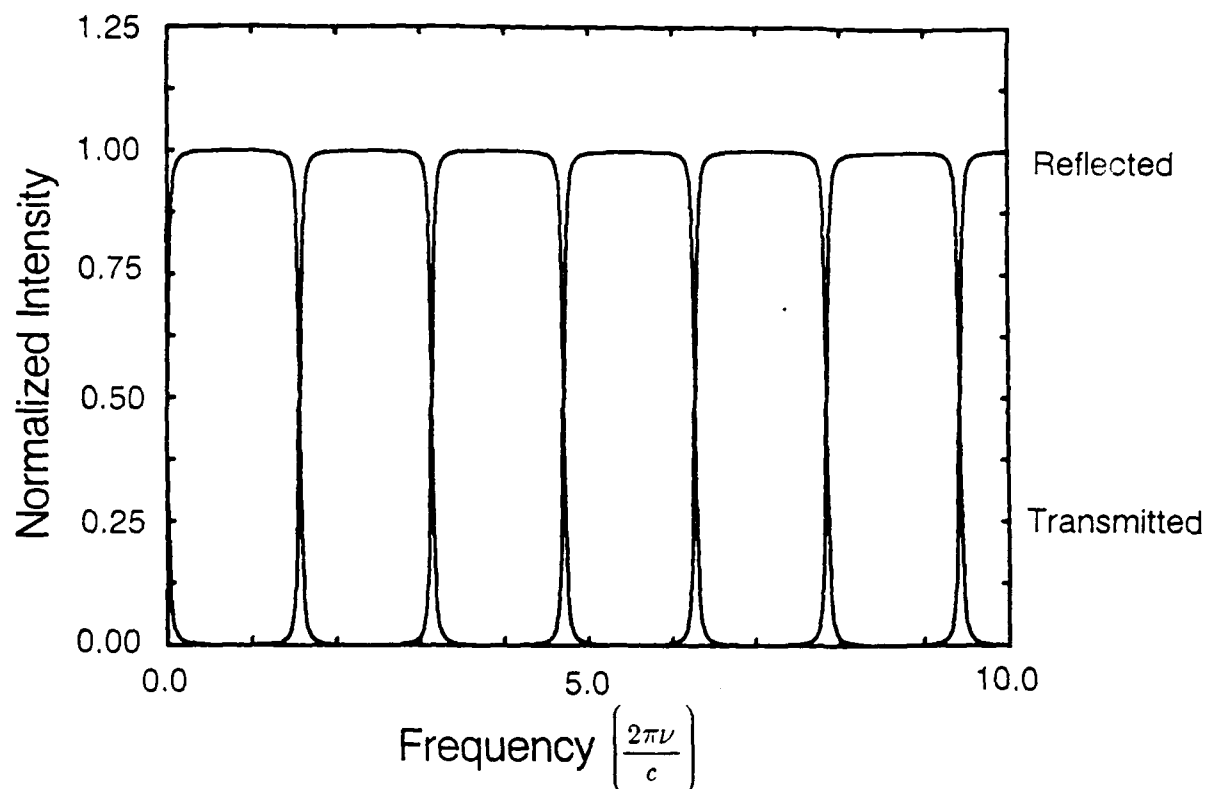


Figure C.2: Normalized reflected and transmitted intensities for a three mirror cavity plotted as a function of frequency with the two end mirrors of 90% reflectivity and the center mirror of 50% reflectivity.

To demonstrate the strength of the present treatment, it was applied to the Fox-Smith cavity whose solution was derived by Smith³⁴ using amplitude splitting arguments. With the assurance that both treatments yielded identical results for the round trip gain, conservation-of-energy boundary conditions were determined to be suitable for use with the three-mirror cavity. For the analysis of laser resonators, the field A is set identically to zero since the fields are internally generated from the gain medium. Considering the case in which a gain medium is placed only in the left cavity, h is set equal to one and the set of equations (C.1.a-f) is solved for g , yielding

$$|g|^2 = \frac{1 - 2r_2r_3\cos(2\delta_2) + (r_2r_3)^2}{(r_1r_3)^2 + 2r_1^2r_2r_3\cos(2\delta_2) + (r_1r_2)^2} \quad (C.7)$$

Similarly, by setting $g = 1.0$, the system can be solved for the case where a gain medium is placed in the right side of the cavity. The results are:

$$|h|^2 = \frac{1 + 2r_1r_2\cos(2\delta_1) + (r_1r_2)^2}{(r_1r_3)^2 + 2r_1r_2r_3^2\cos(2\delta_1) + (r_2r_3)^2} \quad (C.8)$$

These equations specify the minimum single-pass gain the medium must provide to sustain a steady-state field distribution, *i.e.*, the threshold gain. Also, the frequencies at which g and h become real constitute the resonant modes. Plotting $|g|^2$ and $|h|^2$ as functions of frequency (Figure C.3) shows that the threshold gains are equal for both cases, but the mode resonances are out of phase with each other by exactly 90 degrees because of the orientation of the central mirror. Reversing the physical direction of the middle mirror exchanges the mode structures of the two gain expressions. Perhaps more interesting is that the resonances are determined solely by the length of the cavity in which the gain resides although the threshold gain depends on all mirrors. This means that additional cavities coupled to the one containing the gain medium do not affect the free spectral range when the medium is in only one subcavity. In real laser systems, the steady-state field intensity will be at the point where the gain saturates to the threshold level with the relative intensities of the various beams being determined by the resonance conditions.

For coupled lasers with gain media in both cavities, each resonator should, in general, satisfy different gain requirements. Solving equations (C.1) with arbitrary

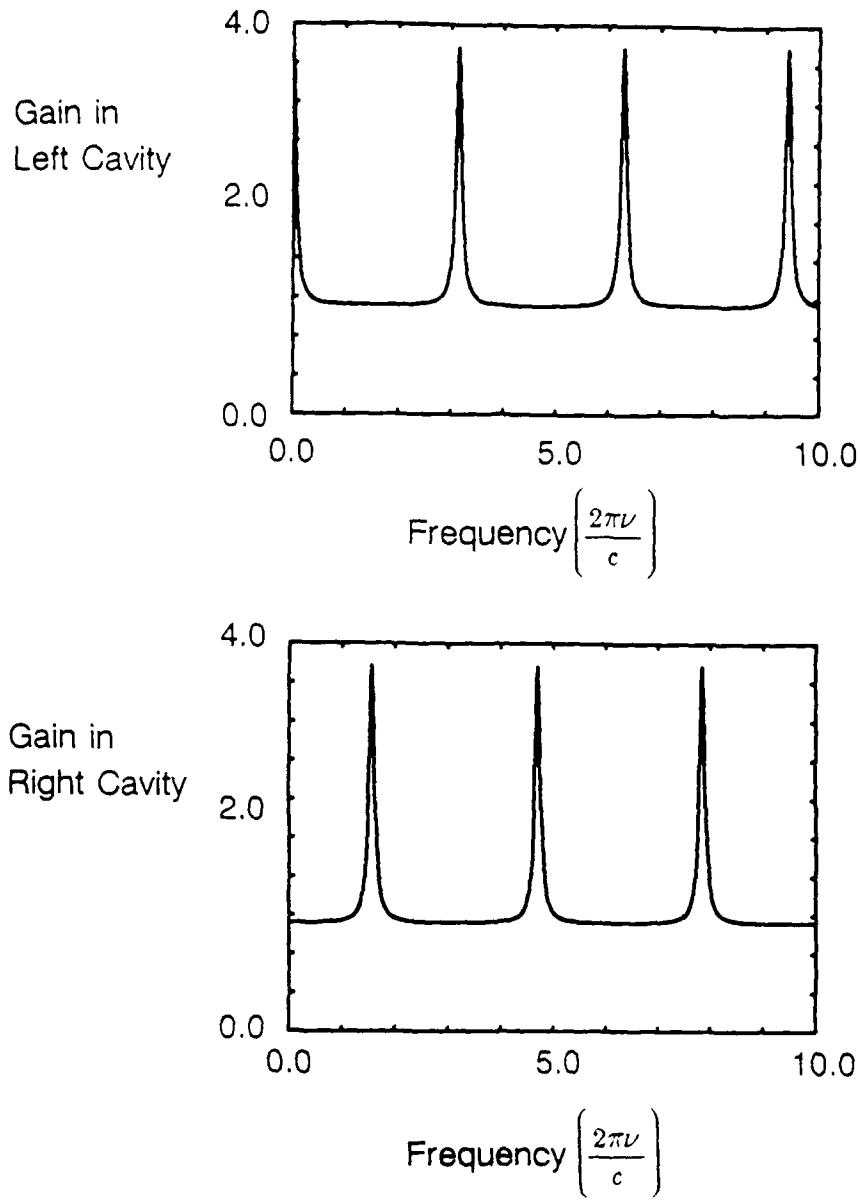


Figure C.3: Round trip gain plotted as a function of frequency showing the spacing of the resonant modes magnitudes with the gain medium in the left- or right- hand cavity only.

h results in a single equation with two unknowns:

$$1 + r_1 r_2 g e^{i2\delta_1} = r_1 r_3 g h e^{i(2\delta_1 + 2\delta_2)} + r_2 r_3 h e^{i2\delta_2} \quad (\text{C.9})$$

This illustrates one operational aspect of coupled lasers; the threshold gains are not uniquely determined, meaning that steady-state laser operation can be attained for many combinations of gain g and h . Physically, this implies that no matter what the threshold gain, g , is, a threshold gain, h , for the other medium can always be found which can sustain steady-state oscillation, and vice versa. Consequently, an additional condition must be imposed in order to solve the equations uniquely. A reasonable additional condition would be to calculate the gain when both subcavities are oscillating at the same frequency. By setting $g = h$, solutions are found only for those frequencies which oscillate simultaneously in both cavities.

Once again, the system of equations (C.1.a-f) is solved to eliminate all the fields producing a complex quadratic equation in the round trip gain, g :

$$g^4 + g^2 \left[\frac{r_2}{r_1} e^{-i2\delta_1} - \frac{r_2}{r_3} e^{-i2\delta_2} \right] - \frac{1}{r_1 r_3} e^{-i(2\delta_1 + 2\delta_2)} = 0 \quad (C.10)$$

with roots

$$g^2 = \beta e^{i\theta} \quad (C.11)$$

where

$$\beta = \left[\frac{1}{4} \left(\frac{r_2^2}{r_3^2} + \frac{r_2^2}{r_1^2} + \frac{b^{1/2}}{4r_1^2 r_3^2} \right) - \frac{1}{2} \frac{r_2^2}{r_1 r_3} \cos(2\delta_2 - 2\delta_1) \right. \\ \left. \pm \frac{r_2 b^{1/2}}{2r_1 r_3^2} \cos(2\delta_2 \mp (\delta_1 + \delta_2)) \mp \frac{b^{1/4}}{2r_1^2 r_3} \cos(2\delta_1 \mp (\delta_1 + \delta_2)) \right]^{1/2} \quad (C.12)$$

$$b = r_2^4(r_1^4 + r_3^4) + 4r_1^2r_3^2(2 - r_2^2)^2 + 2r_1^2r_2^4r_3^2\cos(4\delta_2 - 4\delta_1) \\ + 4r_1r_3r_2^2(2 - r_2^2)(r_1^2 + r_3^2)\cos(2\delta_2 - 2\delta_1) \quad (C.13)$$

$$\theta = \tan^{-1} \left\{ \frac{\frac{r_2}{r_1}\sin 2\delta_1 - \frac{r_2}{r_3}\sin 2\delta_2 \pm \frac{b^{1/2}}{r_1r_3}\sin(\delta_1 + \delta_2)}{\frac{r_2}{r_3}\cos 2\delta_2 - \frac{r_2}{r_1}\cos 2\delta_1 \pm \frac{b^{1/2}}{r_1r_3}\cos(\delta_1 + \delta_2)} \right\} \quad (C.14)$$

the field amplitude gain for a round trip through the entire cavity is

$$g^4 = \beta^2 e^{i2\theta} \quad (C.15)$$

Despite the daunting complexity of these expressions, the actual solutions for the gain become quite transparent. In one special case when $r_1 = r_3$ and $L_1 = L_2$ (*i.e.*, $\delta_1 = \delta_2$), the resultant field amplitude gain reduces to

$$g^4 = \frac{1}{r_1^2} e^{-i4\delta_1} \quad (C.16)$$

In order to constitute a mode of the multimirror cavity, after every round trip, the adjustment in phase the medium has to provide to the fields must be some integer multiple of 2π for the fields to exactly reproduce themselves. Therefore, only those frequencies at which 2θ is an integer multiple of 2π are modes. Figure C.4 graphs $2\theta/2\pi$ as a function of frequency for $r_1 = r_3$ and the two cavities mismatched in length by 10%. Any horizontal slice through the curve at some integer value determines which frequencies can oscillate. In some regions, there are three distinct frequencies all of which satisfy the conditions imposed upon g^4 . The first intersection of the slice ((a) of Figure C.4) corresponds to the

free spectral range determined by $L_1 + L_2$, the second intersection, (b), corresponds to the mode spacing determined by $2L_1$, and the third to that of $2L_2$. There are three different frequencies because a wave can encounter a round trip gain of g^4 in three ways: one total round trip through the resonator, two round trips through the left-hand cavity, or two round trips through the right-hand cavity. When the composite lasers oscillates at the proper frequency, (d), all three combinations of the round trip gain are at exactly the same frequency at the same time.

The most surprising but satisfying result is that the magnitude of the round trip field amplitude gain, g^4 , is equal to $1/r_1^2$ for all frequencies. For a two-mirror cavity, the round trip gain required of the medium to compensate for cavity losses is determined only by the transmission losses through the mirrors. The same condition is true for the three mirror cavity.

Once the magnitude of g^4 is found, the value is substituted into the field equations (C.1.a-f), and the associated intensities are then computed relative to one of the other intensities. Each field is solved in terms of C , C is chosen to be 1.00, and then the relative intensities are calculated by multiplying each field expression by its respective complex conjugate. The values of the intensities for two 90% reflective end mirrors with a range of coupling mirrors are recorded in Table 4.6 in chapter IV along with the interpretation of those results.

D. Conclusion

Conservation of energy boundary conditions were applied to the electric fields

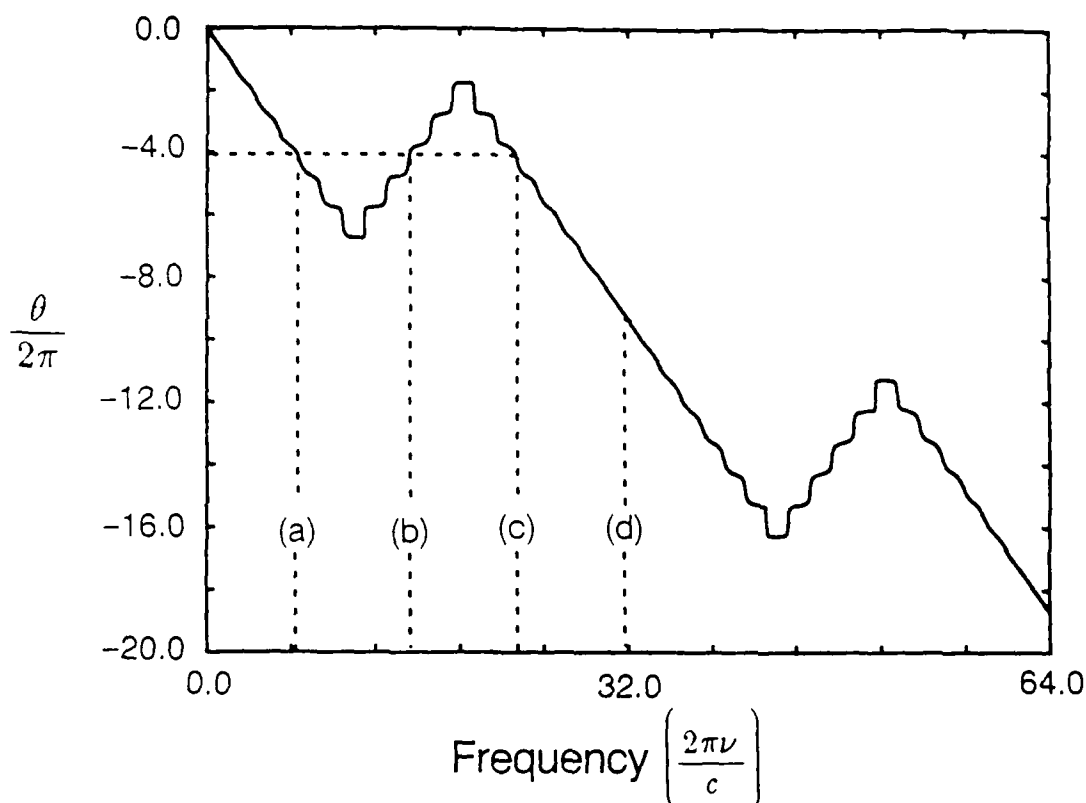


Figure C.4: Phase angle $\theta / 2\pi$ plotted as a function of frequency showing the three oscillating frequencies corresponding to (a) $L_1 + L_2$, (b) $2L_1$, (c) $2L_2$, and (d) when all three frequencies are equal.

incident upon each interface of a three-mirror Fabry-Perot resonator to calculate the resonant behavior and relative intensities of the circulating beams. The method was used to rederive the resonance and transmission properties of two- and three-mirror Fabry-Perot interferometers and also to determine the round trip gain the laser media must supply in order to sustain steady-state oscillation for gain in each subcavity separately, and identical gain in both cavities. The theory can analyze any configuration of partially reflecting mirrors. The results from

two-coupled lasers showed that the imbalance of the circulating intensities may inhibit complete phase locking. More rigorous treatments which include the active gain media must be conducted to conclusively determine if the imbalance is a true manifestation of coupled lasers.

Bibliography

1. T.C. Bradbury, *Theoretical Mechanics*, Krieger Publishing co., Malabar, Fla., 1981.
2. A.D. Pierce, *Acoustics: An Introduction to its Physical Principles and Applications*, McGraw-Hill, N.Y., 1981.
3. P.M. Morse, *Vibration and Sound*, McGraw-Hill, N.Y., 1948.
4. E. Hecht, *Optics*, Addison-Wesley Publishing Co., Reading, Mass., 1987.
5. J.W. Goodman, *Statistical Optics*, Wiley-Interscience, N.Y. 1985.
6. H.L. Stover and W.H. Steier, "Locking of Laser Oscillators by Light Injection", *Applied Physics Letters*, **Vol. 8**, No. 4, February 1966, pp. 91-93.
7. C.N. Man and A. Brillet, "Locking of Ar-ion Lasers", *Optics Letters*, **Vol. 9**, No. 8, August 1984, pp. 333-334.
8. J.L. Jacoby, R.W. Steffan, D. Dee, and V.R. Tiemann, "Multiline, Continuous Wave (CW) Coupled Devices", AFWL-TR-87-85, May 1988.
9. G.E. Palma, W.J. Fader, and K.E. Oughston, "Coupled Resonator Beam Combining Investigation", AFWL-TR-84-95, April 1985.
10. J.M. Bernard, R.A. Chodzko, and H. Mirels, "Mutual Coherence of Two Multiline Continuous-wave HF Lasers", *Optics Letters*, **Vol. 12**, No. 11, November 1987, pp. 897-899.
11. P.R. Cunningham, J.A. Benda, S.S. Townsend, J.W. Collins, and A. Parasco, "Multiline Continuous-wave Coupled Devices", AFWL-TR-88-73, Vol. 1, February 1989.
12. M.B. Spencer and W.E. Lamb, Jr., "Theory of Two Coupled Lasers", *Physical Review A*, **Vol. 5**, No. 2, February 1972, pp. 893-899.
13. W.W. Chow, "Frequency Locking in Weakly Coupled Lasers", *Optics Letters*, **Vol. 10**, No. 9, September 1985, p. 442-444.
14. H. Mirels, "Performance of Two Coupled Lasers", *Applied Optics*, **Vol. 25**, No. 13, July 1986, p. 2130-2137.

15. S.A. Shakir and W.W. Chow, "The Semiclassical Theory of Coupled Lasers", Optics Letters, **Vol. 9** , **No. 6**, **June 1984**, pp. **202-204**.
16. D.M. Walsh, "Longitudinal Supermode Analysis of Two Coupled CO₂ Lasers", Proceedings SPIE, Southeast Conference on Optics and Optoelectronics, April 1986.
17. S.A. Shakir and J.H. Erkkila, "A Supermode Theory of Coupled Unstable Resonators", Final Task Report, CDRL A008, Contract F29601-85-C-0025, May 1987.
18. J.A. Benda and G.E. Palma, Theory of Ring Lasers Coupled Using Reverse Waves", Proceedings SPIE O/E '89, **Vol. 1045** , January 1989.
19. S.M. Rinaldi and J.H. Erkkila, "Semiclassical Modelling and Analysis of Injected Lasers", Proceedings SPIE O/E '89, **Vol. 1045** , **January 1989**.
20. W.E. Lamb, Jr., "Theory of an Optical Maser", Physical Review, **Vol. 134** , **No. 6A**, June 1964, p. A1429-A1450.
21. M. Sargent III, M.O. Scully, and W.E. Lamb, Jr., *Laser Physics* , Addison-Wesley, Reading, Mass., 1977.
22. R.L. Burden, and J.D. Faires, *Numerical Analysis* , PWS Publishers, Boston, Mass., 1985, p. 496.
23. W.R. Bennett, Jr., and R.C. Size, "CW Gain Measurements in Small- Bore Argon-Ion Laser Discharges using a Novel Modulation Technique", IEEE Journal of Quantum Electronics, **Vol. QE-10** , December 1974, p. 908-910.
24. W.R. Bennett, Jr., P.J. Kindlmann, and J. Sunderland, "Relaxation Rates of the Ar⁺ Laser Levels", Applied Physics Letters, **Vol. 5** , **No. 8**, October 1964, p. 158-160.
25. A.E. Siegman, *Lasers* , University Science Books, Mill Valley, Cal., 1986.
26. W.W Chow, "A Composite-Resonator Mode Description of Coupled Lasers", IEEE Journal of Quantum Electronics, **Vol. QE-22** , **No. 8**, August 1986, p. 1174-1183.
27. W.H. Press, *et.al.* , *Numerical Recipes* , Cambridge University Press, Cambridge, Mass., 1988, p. 365.

28. M.P. Jelonek, and W.B. Roh, "Observation of the Mutually-Reinforced Hole Burning Effect in Multi-mode Lasers", To be Published, Optics Communications, 1989.
29. D.Z. Anderson, W.W. Chow, and M.O. Scully, "Optically Biased Laser Gyro", Optics Letters, **Vol. 5** , No. 10, October 1980, p. 413-415.
30. B. Dahmani, L. Hollberg, and R. Drullinger, "Frequency Stabilization of Semiconductor Lasers by Resonant Optical Feedback", Optics Letters, **Vol. 12** , No. 11, November 1987, p. 876-878.
31. J.T. Verdeyen, *Laser Electronics* , Prentice-Hall, New Jersey, 1981.
32. P.W. Smith, "On the Optimum Geometry of a 6328 A Laser Oscillator", IEEE Journal of Quantum Electronics, **Vol. QE-2** , No. 4, April 1966, pp. 77-79.
33. H. van de Stadt and J.M. Muller, "Multimirror Fabry-Perot Interferometers", Journal of the Optical Society of America A, **Vol. 2** , No. 8, August 1985, p. 1363-1370.
34. P.W. Smith, "Stabilized, Single-Frequency Output from a Long Laser Cavity", IEEE Journal of Quantum Electronics, **Vol. QE-1** , No. 8, November 1965, p. 343-348.

Vita

Captain Mark P. Jelonek [REDACTED]

[REDACTED] in

1981 and afterwards attended the Pennsylvania State University where he received a Bachelor of Science degree, with highest distinction, in physics in 1985. He also earned a regular commission in the United States Air Force through the AFROTC program and was immediately called to active duty to enter the physics program of the School of Engineering at the Air Force Institute of Technology at Wright-Patterson Air Force Base from which he was a distinguished military graduate with a Master's of Science in Engineering Physics in December of 1986.

[REDACTED]

19. (continued)

— substantiated by the fact that the maximum power output was also achieved at this point, and the appearance of the super cavity mode spacing verified that the behavior was due to phase locking. A passive cavity mode analysis of the three-mirror Fabry-Perot resonator showed that the system oscillated on the composite resonator frequency as well as the frequencies of both sub-resonators.

REPORT DOCUMENTATION PAGE				Form Approved OMB No. 0704-0188	
1a. REPORT SECURITY CLASSIFICATION UNCLASSIFIED			1b. RESTRICTIVE MARKINGS		
2a. SECURITY CLASSIFICATION AUTHORITY			3. DISTRIBUTION / AVAILABILITY OF REPORT		
2b. DECLASSIFICATION / DOWNGRADING SCHEDULE			Unlimited		
4. PERFORMING ORGANIZATION REPORT NUMBER(S) AFIT/DS/ENP/89-3			5. MONITORING ORGANIZATION REPORT NUMBER(S)		
6a. NAME OF PERFORMING ORGANIZATION Air Force Institute of Technology		6b. OFFICE SYMBOL (If applicable)	7a. NAME OF MONITORING ORGANIZATION		
6c. ADDRESS (City, State, and ZIP Code) Wright-Patterson AFB, Ohio 45433			7b. ADDRESS (City, State, and ZIP Code)		
8a. NAME OF FUNDING / SPONSORING ORGANIZATION		8b. OFFICE SYMBOL (If applicable)	9. PROCUREMENT INSTRUMENT IDENTIFICATION NUMBER		
8c. ADDRESS (City, State, and ZIP Code)			10. SOURCE OF FUNDING NUMBERS		
			PROGRAM ELEMENT NO.	PROJECT NO.	TASK NO.
					WORK UNIT ACCESSION NO.
11. TITLE (Include Security Classification) A Theoretical and Experimental Investigation of Coupled Ar-ion Lasers					
12. PERSONAL AUTHOR(S) Mark P. Jelonek, Capt., USAF					
13a. TYPE OF REPORT Ph.D. Dissertation		13b. TIME COVERED FROM 7/87 TO 10/89		14. DATE OF REPORT (Year, Month, Day) 1989 , 12 , 14	
				15. PAGE COUNT 163	
16. SUPPLEMENTARY NOTATION					
17. COSATI CODES			18. SUBJECT TERMS (Continue on reverse if necessary and identify by block number)		
FIELD	GROUP	SUB-GROUP			
20	06		Phase Locking Ar-ion Lasers		
07	04		Coupling Coherent Combination		
19. ABSTRACT (Continue on reverse if necessary and identify by block number)					
➤ A single-mode laser theory was applied to two coupled Ar-ion lasers in Fabry-Perot resonators and the equations were solved numerically to predict intensity tuning curves and locking ranges for various types of mirror translations. The same theory was extended to model two modes in each cavity, which predicted a decrease in locking range as well as a mutually-reinforced hole-burning minimum. With a single, uncoupled two-mode He-Ne laser, the existence of the minimum was verified experimentally. Two multiline/multimode Ar-ion lasers were coupled through a common end mirror and the effect of coupling strength on phase locking was investigated by varying the reflectivity of that mirror. In order to characterize the phase-locked performance of the multiline/multimode and single-line/multi-mode coupling, interference fringe visibilities, output power, and the frequency and RF mode beat spectra were measured. It was found that the optimal phase locking occurred at approximately 25% coupling as determined by the maximum fringe visibilities produced by laser phase locking. That 25% coupling was the optimum coupling strength was also					
20. DISTRIBUTION / AVAILABILITY OF ABSTRACT <input type="checkbox"/> UNCLASSIFIED/UNLIMITED <input checked="" type="checkbox"/> SAME AS RPT <input type="checkbox"/> DTIC USERS			21. ABSTRACT SECURITY CLASSIFICATION UNCLASSIFIED		
22a. NAME OF RESPONSIBLE INDIVIDUAL Dr. Won B. Roh			22b. TELEPHONE (Include Area Code) (513) 255-2012		22c. OFFICE SYMBOL AFIT/ENP